

Molecular Dynamics Simulation of Nanoscale Condensation on Hybrid Wetting Surface

By

Sudipta Paul

(0419102069)

A thesis has been submitted in partial fulfillment of the requirements for the degree of
MASTER OF SCIENCE IN MECHANICAL ENGINEERING




Department of Mechanical Engineering
Bangladesh University of Engineering and Technology

March 2022

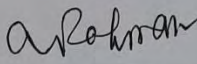
The thesis titled “Molecular dynamics simulation of nanoscale condensation on hybrid wetting surface” submitted by **Sudipta Paul**, Roll No.: **0419102069**, Session: **April, 2019** has been accepted as satisfactory in partial fulfillment of the requirement for the degree of **Master of Science in Mechanical Engineering** on March 13, 2022.

BOARD OF EXAMINERS



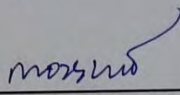
Dr. Muhammad Nasim Hasan
Professor
Department of Mechanical Engineering
BUET, Dhaka

Chairman
(Supervisor)



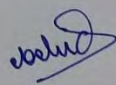
Dr. Muhammad Ashiqur Rahman
Professor and Head
Department of Mechanical Engineering
BUET, Dhaka

Member
(Ex-officio)



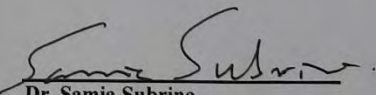
Dr. A. K. M. Monjur Morshed
Professor
Department of Mechanical Engineering
BUET, Dhaka

Member



Dr. Md. Ashiqur Rahman
Professor
Department of Mechanical Engineering
BUET, Dhaka

Member



Dr. Samia Subrina
Professor
Department of Electrical and Electronic Engineering
BUET, Dhaka

Member
(External)

CANDIDATE'S DECLARATION

It is hereby declared that this thesis or any part of this thesis has not been submitted elsewhere for any award or any degree or any diploma.

13 March 2022

Sudipta Paul

ACKNOWLEDGEMENTS

First of all, I would like to express my sincere gratitude to my honorable supervisor, **Dr. Mohammad Nasim Hasan**, for his continuous support, motivation, and guidance throughout my M.Sc. Engg. Program. Without his persistent guidance and support, this dissertation would not be possible.

I am also grateful to the respectable members of the board of examiners **Dr. Muhammad Ashiqur Rahman, Dr. A. K. M. Monjur Morshed, Dr. Md. Ashiqur Rahman** and **Dr. Samia Subrina** for their valuable suggestions and recommendations on my thesis.

Finally, I would like to express my special thanks to my parents, younger brother and my teachers for their constant encouragement throughout the work. I am very fortunate that my parents have always motivated me to achieve success in my life.

"Research is creating new knowledge."
- Neil Armstrong

ABSTRACT

In this study, molecular dynamics simulations have been conducted in order to investigate the condensation process over hybrid wetting surfaces at nanoscale. With a view of pursuing this objective, an enclosed three-phase atomistic system has been modeled, consisting of two solid surfaces and two different phases of fluid atoms. The temperature of the upper and lower solid substrates is kept at 130 K and 90 K, respectively, to make them serve as evaporating and condensing surfaces. In the simulation process, during the non-equilibrium period, the vaporized fluid atoms move from the lower surface to the upper surface and start to get condensed at the upper surface. The wetting characteristics of the lower surface are kept unchanged in all of the cases to corroborate uniform evaporating conditions. The upper condensing surface's wetting configuration was altered to assess how different wetting profiles can affect nanoscale condensation phenomena at different philic-phobic proportions and wettability contrasts. On the upper surface, two types of wetting profiles have been modeled, namely, gradient and patterned wetting profiles. Functional wettability gradient (FWG) surfaces have been modeled using the power-law function from the concept of functionally graded material (FGM), whereas patterned wetting surfaces have been developed by juxtaposing different wettability zones. For determining the performance of hybrid wetting surfaces at different wettability contrasts, four different cases have been modeled by modifying the wettability of the philic-phobic atoms. Nucleation, coalescence, and growth of the condensate, solid-liquid interfacial thermal resistance, condensed atoms, condensation mass flux, condensing wall heat flux, and surface tension profile are the important parameters evaluated for assessing the performance of the condensing surfaces. The simulation results have revealed that an increased proportion of hydrophilic atoms along with lower strip size of philic-phobic pattern enhances the condensation heat transfer. In addition, FWG surfaces have been found to be preferred to patterned ones in terms of condensation heat transfer enhancement, specifically on surfaces with larger hydrophobic fraction. The effect of wettability contrast is prominent on the surfaces with larger hydrophobic fraction and better performance has been observed in case of higher wettability of solid-fluid atoms in terms of condensation heat transfer rate.

NOMENCLATURE

Ar	argon
E	total energy (eV)
F_j	force of an atom j (N)
h_{fg}	latent heat of vaporization of argon (kJ/kg)
G^*	Gibbs free energy
J	Rate of nucleation ($m^{-2}s^{-1}$)
k_B	Boltzmann constant
m_j	mass of an atom j (kg)
m_c	condensation mass flux (kg/m^2s)
$m_{c,avg}$	averaged condensation mass flux (kg/m^2s)
n^*	critical size of nucleus
P	pressure (bar)
Pt	platinum
q_w	heat flux at the condensing wall (MW/m^2)
$q_{w,avg}$	averaged heat flux at the condensing wall (MW/m^2)
q_{therm}	thermodynamic heat flux (MW/m^2)
r_{ij}	distance between molecules i and j (\AA)
t	time (ns)
T	temperature (K)
v_j	velocity of an atom j ($\text{\AA}/ns$)
x	coordinate in x-direction
y	coordinate in y-direction
z	coordinate in z-direction

Greek Symbols

α	fraction of hydrophilic atoms
β	fraction of hydrophobic atoms
γ	surface tension (N/m)
ε	energy parameter of LJ potential (eV)
ε_r	ratio of solid-fluid to fluid-fluid energy parameter
ϕ	short range potential energy (eV)
σ	length parameter of LJ potential (\AA)
ρ_N	Spatial number density ($1/\text{\AA}^3$)

Dedicated to my Parents.....

TABLE OF CONTENTS

CANDIDATE’S DECLARATION	iii
ACKNOWLEDGEMENTS.....	iv
ABSTRACT	vi
NOMENCLATURE.....	vii
LIST OF FIGURES	xii
LIST OF TABLES	xvi
CHAPTER 1: INTRODUCTION.....	1
1.1 Background	1
1.1.1 Wettability	1
1.1.2 Modes of condensation.....	2
1.1.3 Hybrid wetting surface	5
1.1.4 Functionally graded materials (FGM).....	7
1.1.5 Molecular Dynamics (MD) Simulation.....	8
1.2 Motivation of the Present Study	9
1.3 Objectives of the Present Study.....	10
1.4 Thesis Outline.....	10
CHAPTER 2: LITERATURE REVIEW	12
2.1 Experimental study on condensation over patterned hybrid wetting surface	12
2.2 Experimental study on condensation over nanostructured hybrid wetting surface.....	15
2.3 Molecular dynamics study on condensation phenomena.....	17
CHAPTER 3: FUNDAMENTALS OF MOLECULAR DYNAMICS	22
3.1 Molecular Dynamics Simulation.....	22
3.1.1 Advantages of Molecular Dynamics	25
3.1.2 Limitations of Molecular Dynamics.....	25
3.1.3 Steps of Molecular Dynamics Simulation	26
3.1.4 Potential function	27
3.1.5 Time integration algorithm	32
3.1.6 Boundary Conditions.....	35
3.1.7 Temperature and pressure control.....	37

3.1.8 Statistical ensembles.....	38
3.2 LAMMPS – Large-scale Atomic/Molecular Massively Parallel Simulator	41
3.2.1 LAMMPS operation	42
3.2.2 LAMMPS pre- and post-processing	43
3.3 OVITO – Open Visualization Tool	44
CHAPTER 4: SIMULATION MODEL AND PERFORMANCE PARAMETERS	45
4.1 Simulation methodology of the present study.....	45
4.2 Evaluation of transport characteristics.....	50
4.2.1 Temperature	50
4.2.2 Total energy	50
4.2.3 Spatial density	50
4.2.4 Heat flux	51
4.2.5 Surface tension.....	51
4.2.6 Time-averaged condensation mass flux	52
4.2.7 Time-averaged condensing wall heat flux.....	52
4.2.8 Thermodynamic heat flux.....	53
CHAPTER 5: RESULTS AND DISCUSSIONS	54
5.1 Equilibrium characteristics and model validation	54
5.1.1 Spatial number density	54
5.1.2 Temperature of system components.....	56
5.1.3 Total energy of argon atoms	56
5.1.4 Wall heat flux during equilibrium period.....	58
5.2 Effect of philic-phobic content and patterning.....	58
5.2.1 System characteristics for different cases.....	60
5.2.2 Solid-liquid interfacial thermal resistance for different hybrid wetting surface.....	62
5.2.3 Nucleation and growth mode of condensate for different condensing surface.....	65
5.2.4 Transient condensation over different hybrid wetting surfaces at nanoscale	69
5.2.5 Heat flux characteristics at the condensing wall	73
5.2.6 Local surface tension profile near the condensing wall	77
5.3 Effect of gradient and patterned wetting configuration	Error! Bookmark not defined.
5.3.1 Transient variation of system behavior	Error! Bookmark not defined.

5.3.2 Thermal resistance at the solid-liquid interface	Error! Bookmark not defined.
5.3.3 Nucleation, coalescence and growth characteristics	Error! Bookmark not defined.
5.3.4 Transient condensation over different hybrid wetting surfaces ...	Error! Bookmark not defined.
5.3.5 Heat flux characteristics at the condensing wall	Error! Bookmark not defined.
5.3.6 Surface tension profile at the vicinity of condensing surface	Error! Bookmark not defined.
5.4 Effect of wettability contrast	Error! Bookmark not defined.
5.4.1: System characteristics for different cases	Error! Bookmark not defined.
5.4.2 Thermal resistance at the solid-liquid interface	Error! Bookmark not defined.
5.4.3 Nucleation, coalescence and growth characteristics for different cases	Error! Bookmark not defined.
5.4.4 Transient condensation over different hybrid wetting surfaces ...	Error! Bookmark not defined.
5.4.5 Heat flux characteristics at the condensing wall	Error! Bookmark not defined.
5.4.6 Time-averaged condensation characteristics	124
CHAPTER 6: CONCLUSIONS	125
REFERENCES	127

LIST OF FIGURES

Figure 1.1	Classification of the wettability of a surface from contact angle perspective	2
Figure 1.2	Schematic illustration of (a) filmwise condensation (b) dropwise condensation	3
Figure 1.3	Schematic showing wetting regimes over rough surface (a) Wenzel state (b) Partially wetting state (c) Cassie state	5
Figure 1.4	Surface morphology of patterned hybrid wetting surface	6
Figure 1.5	Fabrication process of microstructured hydrophobic–hydrophilic hybrid wetting surfaces	6
Figure 1.6	FGM in nature (a) human tooth (b) human bone	7
Figure 2.1	Inter-digitated design of periodically-patterned hybrid wetting surface fabricated by Mahapatra et al. [52].....	13
Figure 2.2	Pictures of prepared hydrophobic–hydrophilic hybrid surface by Peng et al. [86] (light: hydrophobic region; gray: hydrophilic region).....	14
Figure 2.3	Schematic of microstructured hybrid wetting surface prepared by Varanasi et al. [89].....	15
Figure 2.4	Schematic drawing (left) and scanning electron microscopy (SEM) image of nanograssed micropyramid arrays (right) prepared by Chen et al. [44].....	16
Figure 2.5	Simulation domain for the MD study performed by Liang et al. [91].....	18
Figure 2.6	Simulation setup of Pt-water system modelled by Niu and Tang [34].....	19
Figure 2.7	Simulation domain for the MD study performed by Ghahremanian et al. [95].....	21
Figure 3.1	Range in various time and length scales used in modelling	23
Figure 3.2	Molecular dynamics simulation system as a collection of N particles in a particular volume	24
Figure 3.3	Fundamental algorithm followed for solving classical molecular dynamics simulation	26
Figure 3.4	LJ potential between two atoms i and j	30
Figure 3.5	Periodic boundary condition (Basic cell is replicated in all the directions)	36
Figure 3.6	Coordinates of primary and image atoms in periodic boundary condition	36
Figure 3.7	Fixed boundary condition (Atomistic rigid wall)	37
Figure 4.1	Simulation domain at the beginning of the simulation	45
Figure 4.2	Liquid-solid wetting scenario at the equilibrium state for different solid-liquid interaction strengths	47
Figure 4.3	Atomistic configuration of the (a) patterned (b) FWG hybrid wetting surface with $\alpha = 0.6$	47
Figure 4.4	Wettability gradient profile, namely, the spatial variation of the Ar-Pt energy parameter, ϵ_{Ar-Pt} for different hydrophobic weight fraction, β of (a) FWG and (b) patterned surfaces	49
Figure 5.1	(a) Spatial number density, ρ_N profile of Argon along y-direction and (b) Reduced density profile of argon on a flat Pt-surface as depicted in Morshed et al.	55
Figure 5.2	Temperature of the atomistic elements during equilibration period ($\alpha = 0.2$)	56
Figure 5.3	(a) Temporal variation of total energy of argon atom ($\alpha = 0.2$), and (b) system energy curve during equilibration period in ref. [125]	57
Figure 5.4	Heat flux at the condensing wall ($\alpha = 0.2$)	58

Figure 5.5	(a) Wetting configuration of the top surface for different cases (b) Change in interaction energy parameter ratio, $\epsilon_{Ar-Pt}/\epsilon_{Ar-Ar}$ for various cases	59
Figure 5.6	Temporal variation of total energy content of Argon atoms (a) at different portion of hydrophilic and hydrophobic region (b) at different strip size having equal portion of hydrophilic and hydrophobic region	61
Figure 5.7	Simulation domain with dimensions 10 nm x 8.9 nm x 7 nm along x, y and z-axis at the beginning for calculating solid-liquid interfacial thermal resistance	62
Figure 5.8	(a) Spatial variation of temperature along the direction of heat flow for different cases, (b) Similar variation of temperature along the direction of heat flow in ref. [127], (c) Temporal variation of heat flow through heat source and heat sink for different cases, and (d) Similar variation of heat flow across heat source and heat sink in ref. [127].....	63
Figure 5.9	Thermal resistance profile at the solid-liquid interface, R_{int} with the variation in (a) hydrophobic fraction, (b) hydrophilic-hydrophobic patterned strip size of hybrid wetting surface	64
Figure 5.10	Snapshots of atomic trajectory at top surface for showing difference in nucleation and growth of liquid clusters of Argon atoms with change in hydrophilic portion percentage. Colors indicating- blue for hydrophilic region, orange for hydrophobic region, purple for vapor Ar atoms, green for liquid Ar atoms	66
Figure 5.11	Snapshots of atomic trajectory at top surface for showing difference in nucleation and growth of liquid clusters of Argon atoms with change in strip size of patterned hybrid wetting surface. Colors indicating- blue for hydrophilic region, orange for hydrophobic region, purple for vapor Ar atoms, green for liquid Ar atoms	67
Figure 5.12	Temporal variation of number of condensed atoms in cases with (a) different portion of hydrophilic and hydrophobic region (b) different strip size having equal portion of hydrophilic and hydrophobic region	70
Figure 5.13	Temporal variation of condensation mass flux at (a) different portion of hydrophilic and hydrophobic region (b) different strip size having equal portion of hydrophilic and hydrophobic region	71
Figure 5.14	Temporal variation of heat flux at condensing wall for (a) different portion of hydrophilic and hydrophobic region (b) different strip size having identical portion of hydrophilic and hydrophobic region	74
Figure 5.15	Variation of number density profile of Argon atoms near the condensing wall at 2.3 ns for various cases with change in (a) fraction of hydrophilic and hydrophobic portion (b) strip size having equal portion of hydrophilic and hydrophobic region	75
Figure 5.16	Variation of average condensation mass flux, average heat flux at condensing wall and thermodynamic heat flux for different cases with change in fraction of hydrophobic and hydrophilic portion	76
Figure 5.17	Contour plot of local liquid-vapor interfacial surface tension at 4.5 ns	78
Figure 5.18	Wetting profile of the condensing surface in different cases	80
Figure 5.19	Wettability gradient profile, namely, the spatial variation of the Ar-Pt energy parameter, ϵ_{Ar-Pt} for different (a) FWG (group A) and (b) patterned surfaces (group B)	81
Figure 5.20	Temporal evolution of total energy of fluid atoms for different cases	82
Figure 5.21	(a) Temporal evolution of heat flow across source and sink (b) Spatial distribution of temperature of the fluid atoms along the direction of heat flow	83
Figure 5.22	Solid-liquid interfacial thermal resistance, R_{int} for various cases of FWG and patterned hybrid wetting surface	84

Figure 5.23	Total energy contour of the fluid atoms at the vicinity of the condensing surface for different cases of FWG configuration	85
Figure 5.24	Total energy contour of the fluid atoms at the vicinity of the condensing surface for different cases of patterned wetting configuration	86
Figure 5.25	Snapshots of surface cluster on condensing surface (z-x plane) at different timesteps for different cases of FWG surfaces (Green color indicates the condensed argon atoms in the surface clusters and pink color indicates condensed argon atoms not in any surface cluster)	87
Figure 5.26	Snapshots of surface cluster on condensing surface (z-x plane) at different timesteps for different cases of patterned surfaces (Green color indicates the condensed argon atoms in the surface clusters and pink color indicates condensed argon atoms not in any surface cluster)	90
Figure 5.27	Temporal variation of surface clusters for (a) FWG condensing surfaces, (b) patterned condensing surfaces	91
Figure 5.28	Temporal variation of surface clusters above threshold sizes for (a) FWG condensing surfaces, (b) patterned condensing surfaces	92
Figure 5.29	Temporal variation of condensation characteristics in terms of (a) amount of condensed fluid atoms and (b) condensation mass flux	95
Figure 5.30	Temporal variation of heat flux at the condensing wall for different cases	96
Figure 5.31	Average mass flux of the condensate and average condensing wall heat flux for different cases	96
Figure 5.32	Liquid-vapor interfacial surface tension profile for different cases near the condensing surface at 4 ns	98
Figure 5.33	Wetting configuration of the different types of condensing surface	100
Figure 5.34	Temporal evolution of total energy of fluid atoms for different cases of (a) surface 1A and (b) surface 1B	101
Figure 5.35	Temporal evolution of total energy of fluid atoms for different cases of (a) surface 2A and (b) surface 2B	102
Figure 5.36	Temporal evolution of heat flow across source and sink for (a) surface 1A and (b) surface 1B	104
Figure 5.37	Temporal evolution of heat flow across source and sink for (a) surface 2A and (b) surface 2B	105
Figure 5.38	Spatial temperature distribution along y-axis for (a) surface 1A and (b) surface 1B	106
Figure 5.39	Spatial temperature distribution along y-axis for (a) surface 2A and (b) surface 2B	107
Figure 5.40	Solid-liquid interfacial thermal resistance, R_{int} for different cases of hybrid wetting surface	108
Figure 5.41	Temporal variation of surface clusters for different cases of (a) surface 1A and (b) surface 1B	109
Figure 5.42	Temporal variation of surface clusters for different cases of (a) surface 2A and (b) surface 2B	110
Figure 5.43	Snapshots of atomic trajectory at condensing surface for showing difference in nucleation and growth of liquid clusters of Argon atoms for different cases in surface 1A. Colors indicating- blue for hydrophilic region, orange for hydrophobic region, purple for vapor Ar atoms, green for liquid Ar atoms	112
Figure 5.44	Snapshots of atomic trajectory at condensing surface for showing difference in nucleation and growth of liquid clusters of Argon atoms for different cases in surface 1B. Colors indicating- blue for hydrophilic region, orange for hydrophobic region, purple for vapor Ar atoms, green for liquid Ar atoms	113

Figure 5.45	Snapshots of atomic trajectory at condensing surface for showing difference in nucleation and growth of liquid clusters of Argon atoms for different cases in surface 2A. Colors indicating- blue for hydrophilic region, orange for hydrophobic region, purple for vapor Ar atoms, green for liquid Ar atoms	114
Figure 5.46	Snapshots of atomic trajectory at condensing surface for showing difference in nucleation and growth of liquid clusters of Argon atoms for different cases in surface 2B. Colors indicating- blue for hydrophilic region, orange for hydrophobic region, purple for vapor Ar atoms, green for liquid Ar atoms	115
Figure 5.47	Temporal variation of number of condensed atoms for different cases of (a) surface 1A and (b) surface 1B	117
Figure 5.48	Temporal variation of number of condensed atoms for different cases of (a) surface 2A and (b) surface 2B	118
Figure 5.49	Temporal variation of condensation mass flux, m_c for different cases of (a) surface 1A and (b) surface 1B	119
Figure 5.50	Temporal variation of condensation mass flux, m_c for different cases of (a) surface 2A and (b) surface 2B	120
Figure 5.51	Temporal variation of condensing wall heat flux, q_w for different cases of (a) surface 1A and (b) surface 1B	122
Figure 5.52	Temporal variation of condensing wall heat flux, q_w for different cases of (a) surface 2A and (b) surface 2B	123
Figure 5.53	Variation of (a) average condensation mass flux, $m_{c,avg}$ and (b) average condensing wall heat flux, $q_{w,avg}$ for different cases of hybrid wetting surface...	124

LIST OF TABLES

Table 5.1	Overview of all the cases of condensing surface.....	79
Table 5.2	Rate of nucleation, J for different cases.....	93
Table 5.3	Solid-fluid energy parameter for different cases of wettability contrast.....	99

1.1 Background

Condensation is a process through which the phase of the fluid is transformed from vapor to liquid. Because of being an omnipresent and complex heat transfer process, it has drawn attention of the scientists and researchers over the years. The application of the condensation process covers a wide range of engineering fields such as water harvesting [1,2], desalination [3,4], refrigeration [5,6], HVAC [7], power plants [8,9], environmental control [10] and cooling of electronic devices [11]. For this reason, it has become important to obtain a deep insight of condensation process. In condensation process, the phase of fluid is shifted from vapor to liquid across a tiny region. This tiny region of nanoscale is termed as the liquid-vapor interface. During the transition from vapor to liquid across the liquid-vapor interface huge change of thermophysical and transport characteristics is observed that is quite important for the condensation process [12]. For microscale and nanoscale condensation phenomenon, the effect of thermophysical processes at the liquid-vapor interfaces are highly important compared to that at the macroscale [12]. With the rapid advancement of micro and nano-electromechanical systems (MEMS/NEMS) the scale of the electronic devices has been shrunk to a scale of micrometer to nanometer. But with the inclusion of micro and nano-electronic cooling devices, heat dissipation has become an important issue owing to limitations of space [13,14]. Overheating can lead to potential damage to the components of nano-electronic devices and degrade the performance of the same [14]. To alleviate such problems, phase change heat transfer at nanoscale can be considered as potential solution to this because of its high heat removal capability by utilizing the high latent heat of vaporization [14]. For this reason, in recent years it has become a prime focus of researchers to achieve a detailed insight on the condensation process at nanoscale to enhance the condensation phenomenon at nanoscale.

1.1.1 Wettability

Wettability is the preference of a liquid to be in contact with a solid surrounded by another fluid (liquid or gas). Adhesive and cohesive forces between the solid and the liquid determine the

wettability. Cohesive forces affect in between the same type of molecules. In a liquid or solid, the molecules are pulled towards each other because of the cohesion between the molecules. Adhesion is the interaction between unlike molecules. The balance between these forces is what defines the degree of wettability.

Solids can be divided into high and low-energy solids. High energy solids such as glass, ceramics, and metals are held together by chemical bonds (covalent, ionic and metal) which are very strong. This causes high excess energy on the surface of the solid i.e. the name high energy solid. Most of the liquids will wet the high energy solid completely as that will lead to a decrease in interfacial energy. Low-energy solids, such as many of the polymers, especially Teflon are harder to wet.

Contact angle is a measure of wettability. A drop of liquid is placed on the solid and contact angle can be optically measured. Typically, 90° contact angle is considered as a threshold value. When the contact angle is above 90° the wettability is low i.e., hydrophobic/superhydrophobic, when it is below 90° the wettability is high i.e., hydrophilic/superhydrophilic as shown in figure 1.1.

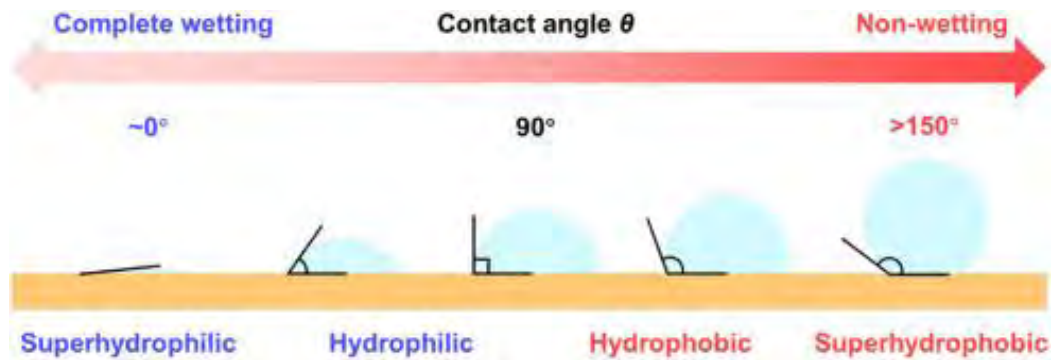


Figure 1.1: Classification of the wettability of a surface from contact angle perspective [15].

1.1.2 Modes of condensation

Based on the nucleation and droplet growth and departure mode of condensation is classified into two types i.e., filmwise condensation (FWC) and dropwise condensation (DWC). The development of different condensation mode depends mainly on the thermophysical properties of the condensate, the operating conditions, and the characteristics of the condensing surface. Among them wettability of the surface is the preponderant factor affecting the development of condensation mode [16,17]. It is known that FWC takes place on hydrophilic surface [18] while, DWC takes place on hydrophobic surface [19].

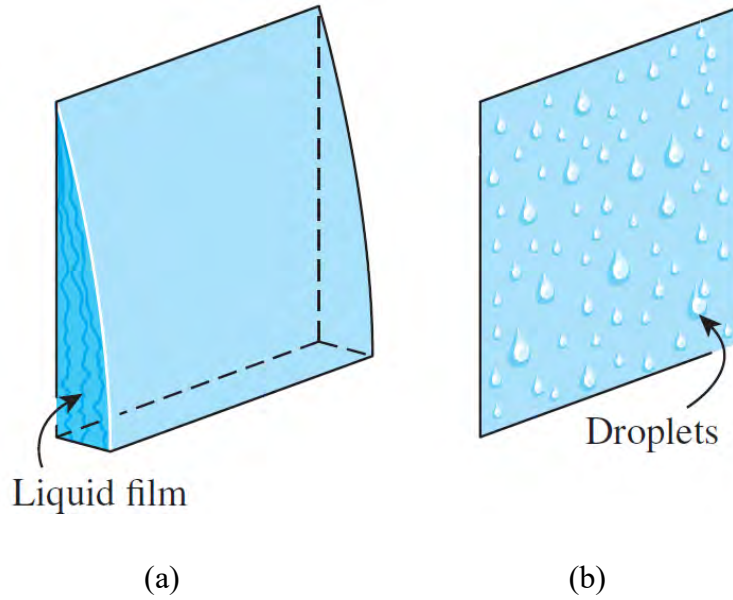


Figure 1.2: Schematic illustration of (a) filmwise condensation (b) dropwise condensation [20].

(a) Filmwise condensation (FWC): In this condensation mode, the condensing surface is blanketed by the layer of condensate film as shown in figure 1.2 (a). This layer of condensate develops an extra layer of thermal resistance which causes reduction of heat transfer as observed in the previous studies of condensation at macroscale [16–19]. It is reported that the heat transfer rate is reduced to 5-6 times in FWC compared the DWC [21]. Several techniques have been implemented by the researchers to enhance the performance of filmwise condensation at macroscale. These techniques include inclusion of microfin or grooved surfaces [22–24], coating of low surface energy materials [25–27], SLIPS (slippery liquid infused porous surface) or LIS (liquid infused surfaces) [28–30], reducing the thermal resistance of the liquid film using porous medium [31,32], introducing capillary forces through wicking [33]. These methods have provided positive results in terms of condensation heat transfer enhancement in macroscale. But the performance of different modes of condensation (FWC and DWC) in terms of rate of heat transfer is different in nanoscale from macroscale [34,35].

(b) Dropwise condensation (DWC): This condensation mode is observed on the low energy surfaces i.e., hydrophobic surfaces where droplets are formed on specific nucleation sites [19] as shown in figure 1.2 (b). The droplets thus formed slide down when they reach a certain critical size, clearing the surface and exposing it to vapor [36]. There is no liquid

film in this case to resist heat transfer. The process is completed after following few steps such as at first DWC are formed at specific nucleation sites [37], and grow by either coalescence or direct condensation until a critical droplet radius is reached. Beyond this point, body forces (typically gravitational) will exceed the surface tension holding the droplet on the surface; thus, causing the droplets to depart from the vertical surface. The departing droplets also sweep the surface clear due to vapor shearing, thus permitting new nucleation sites on the surface so that the process repeats itself [38,39]. There are various techniques implemented by the researchers to promote dropwise condensation such as treating or coating the surface with polymers, e.g., Teflon [40,41], organic promoters such as fatty acids [42] or by implanting ions of low energy [43]. Different surfaces have been modelled with nanostructures to induce superhydrophobic characteristics on the condensing surface and developed dropwise condensation [44,45]. From microscopic or molecular viewpoint, it is noticed that the condensing surface is not perfectly smooth. Depending on the roughness of the surface 3 different types of wetting state are observed in figure 1.3 [46]:

(a) Wenzel state:

It is the highly pinned state where the droplets adhere to the surface firmly.

(b) Partial wetting state:

Here, the droplet does not spread but instead forms a spherical cap resting on the substrate.

(c) Cassie state:

Here, the droplet does not spread onto the surface rather is suspended on the rough surface.

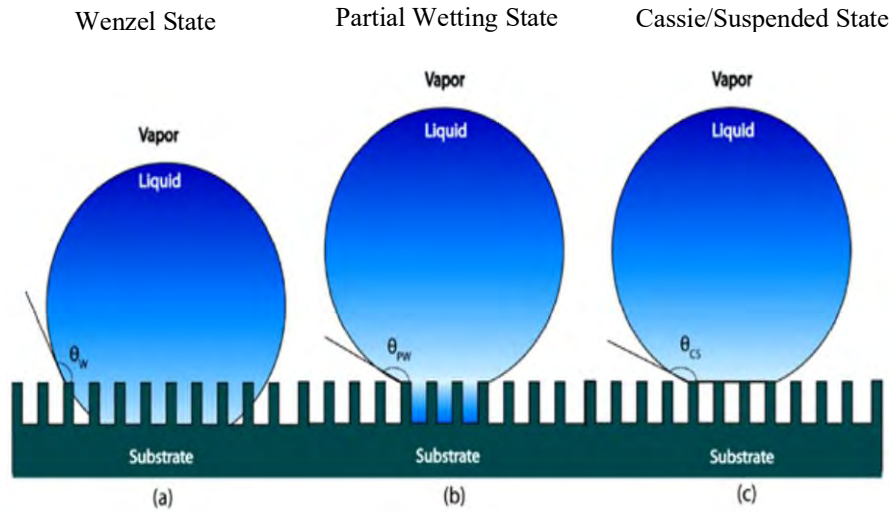


Figure 1.3: Schematic showing wetting regimes over rough surface (a) Wenzel state (b) Partially wetting state (c) Cassie state [36].

1.1.3 Hybrid wetting surface

Hybrid wetting surface can be defined as the surface which contains interlaced hydrophilic hydrophobic regions and thus results in having different wettability over the surface. Thus, the liquid spread on it will have varying contact angle along the surface. It is known that hydrophilic or superhydrophilic surface promotes higher nucleation density [47,48] and hydrophobic or superhydrophobic ones have better droplet departure characteristics [49,50]. Therefore, a combination of these effects is required for achieving the best condensation performance. Hence, the surface has higher nucleation sites and rapid droplet removal rate so after droplet removal, nucleation sites are rejuvenated again for nucleation, is considered the optimum surface for condensation. So, with a view to harnessing the synergistic effect of higher nucleation density and quicker droplet removal researchers have performed theoretical and experimental studies on condensation heat transfer over hybrid wetting surfaces and obtained remarkable result in terms of condensation heat transfer enhancement.

Researchers have fabricated hybrid wetting by incorporating patterned topology [51–54] or microstructured/nanostructured configurations [44,45,55–57].

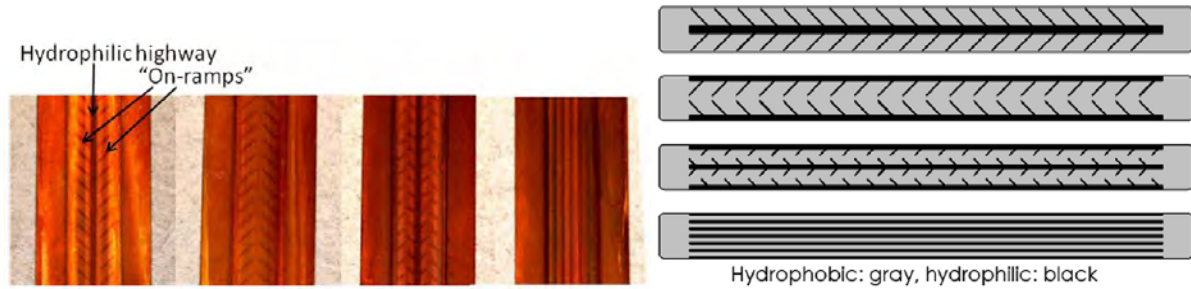


Figure 1.4: Surface morphology of patterned hybrid wetting surface [54].

Derby et al. [54] prepared hybrid wetting surface through coating and chemical etching. At first, the copper channel was cleaned with isopropyl alcohol and plasma etched. Then, the surface was dipped in a solution of Teflon AF 1601S. Then, The substrate is transferred into a patterned hard mask to the channel via a plasma etch and hydrophobic/hydrophilic surfaces were created as shown in figure 1.4.

Tokunaga et al. [57] prepared hybrid wetting surface by incorporating micro structured morphology. The fabrication process of microstructured hybrid wetting surface is illustrated in figure 1.5.

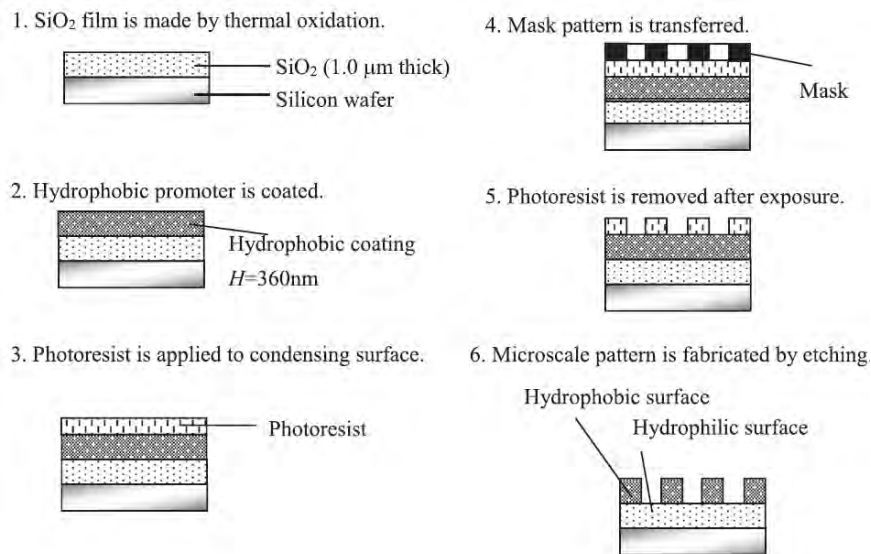


Figure 1.5: Fabrication process of microstructured hydrophobic–hydrophilic hybrid wetting surfaces [57].

1.1.4 Functionally graded materials (FGM)

Functionally graded materials (FGM) are considered one of the most promising materials among the class of advanced fabricated materials. They consist of two or more different materials, where the composition continuously varies along a dimension following a particular function [58]. FGMs are conceived as a solution to solve high-stress concentration, high-temperature creep, and material delamination [59] challenges that are common in other fabricated materials such as composites. These enhanced thermal and mechanical properties render FGM a suitable candidate for manufacturing structures of airplanes, automobile engine components, and protective coatings for turbine blades [60,61]. Furthermore, recent researches showed that human teeth and bone can be considered as functionally graded living tissues from nature [62] as shown in figure 1.6.

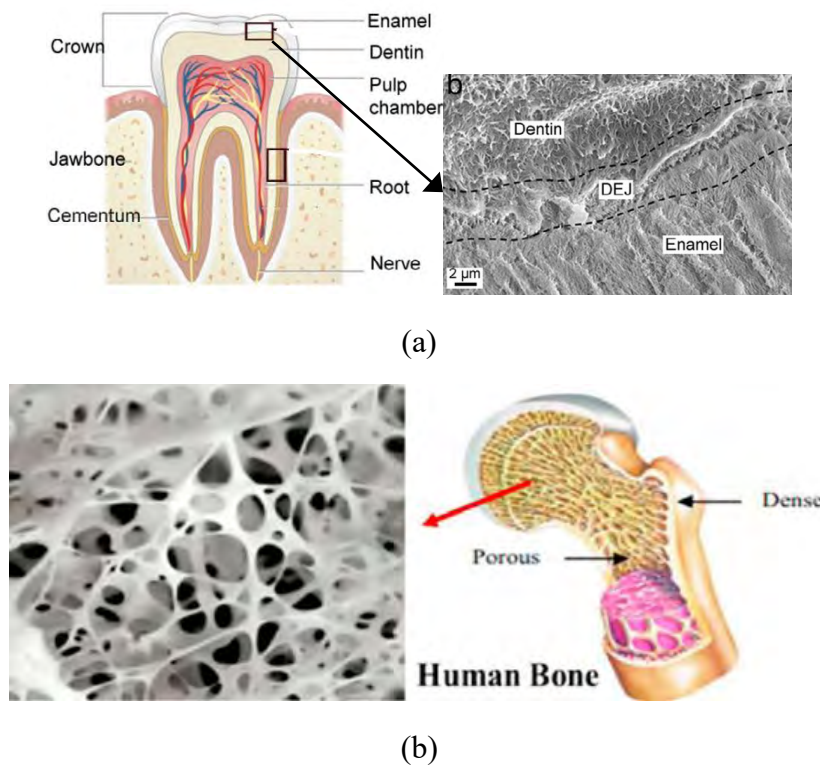


Figure 1.6: FGM in nature (a) human tooth [63] (b) human bone [64].

Thus, the application of FGMs has found its way into teeth and bone replacement industry. Due to the applications in the fields of aerospace, automobile, medicine, and energy, the research efforts to characterize the mechanical and thermal properties of FGMs have increased rapidly in recent years. In recent years, applications of FGMs have shifted towards sophisticated micro and

nanoscale electronics and energy conversion devices such as broadband ultrasonic transducer, solid oxide fuel cells [65], high current connectors [66] and thermoelectric energy converter [60].

In this study, hybrid wetting surfaces with functional wettability gradient (FWG) have been modelled by utilizing the concept of FGM where the wettability of the surface is changed from hydrophilic to hydrophobic along the length following a gradient function as delineated in chapter 4.

1.1.5 Molecular Dynamics (MD) Simulation

Among all phase change phenomena, one of the most common is condensation heat transfer phenomena, especially in practical engineering applications. In the last few decades, a lot of comprehensive studies have been conducted regarding this to achieve optimum energy efficiency in industrial sectors. Researchers developed some theoretical models to predict the exact nature of condensation as well as performed some macroscopic/experimental studies in lab scale to visualize these phenomena in practical cases. But condensation is a two-phase complex process and the precise understanding of the occurrence of different phase transitions of condensation is very difficult through the experimental studies only. Because, due to the very small scale of liquid-vapor interface, most often it is not possible to materialize accurate experimentation of condensation at this scale and thus empirical correlations obtained from many experimental studies cannot sufficiently predict the characteristics of condensation phenomena at nanoscale. Moreover, in classical thermodynamics, phase transitions are considered as the quasi-equilibrium process but in most cases, real phase change phenomena deviate from this process. So, the classical thermodynamics approach cannot successfully anticipate the phase change process in molecular level in most cases. In the last two decades a lot of technological advancement occurred and with the advent of computational facilities, scientists are now investigating these complicated and highly non-equilibrium processes in nanoscale. Nonequilibrium molecular dynamics (NEMD) [67] is a powerful simulation tool which can render a very accurate insight about the phase change phenomena from the atomistic viewpoint. The broad spectra of previous MD studies include analysis of nucleation [68–71] and growth mode of condensate [72], cluster formation and coalescence [68,73–75], impact of nanostructure on wetting state affecting condensation heat transfer [76–81], variation of condensation heat transfer with surface wettability [34,35,68,73], vapor temperature [82,83], variation of interfacial thermal resistance with surface energy [71–73],

condensate drainage [75] and droplet motion with wettability gradient [84,85]. Summary of these studies are delineated in chapter 2.

1.2 Motivation of the Present Study

With the progress of nanotechnology, the scale of electronic components has been reduced to micrometer to nanometer range. Study of nanoscale condensation has become a prime focus of the contemporary researchers to alleviate the problem of overheating of these devices with a view to enhance their capacity of rapid heat removal from a very small space. As a result, it has become very much important for the scientists to obtain a deep insight on the liquid-vapor interfacial characteristics of the fluid atoms with a view to improvise the condensation heat transfer rate. Previously, molecular dynamics (MD) studies have been conducted on the homogeneous wetting surfaces to gain an atomistic perspective of nanoscale condensation process. To harness the combined advantages of higher nucleation rate and better droplet departure characteristics hybrid wetting surfaces have been prepared for experimental studies at large scale. Their experimental results revealed a remarkable rise in condensation heat transfer. But in those studies, gravitational forces and vapor shear forces played a significant role droplet motion. But in NEMS/ MEMS devices these forces can not play considerable role due to limitations in space. Furthermore, with the existing experimental setup, it is difficult to properly visualize some important stages of nanoscale condensation phenomena such as nucleation, coalescence, and growth of condensate layer [79]. To overcome these difficulties, with the rapid advancement in computational technology, molecular dynamics (MD) simulation has become very popular among researchers of various fields for having a deeper insight and better visualization of the condensation process. But no molecular dynamics study has been performed on condensation phenomenon over hybrid wetting surfaces.

Hence, in this present work, molecular dynamics study has been performed to obtain an atomistic insight on the condensation process over hybrid wetting surfaces.

1.3 Objectives of the Present Study

In this study, MD simulations were performed on a confined domain where the bottom surface at 130 K acted as a source of vapor atoms and top surface at 90 K acted as the condensing surface. Under the same wetting characteristics of the bottom surface, different condensing surfaces were modelled in order to investigate the effect of (a) hydrophilic-hydrophobic content (c) gradient profile (c) wettability contrast of the hybrid wetting surface on the condensation performance.

The specific objectives of this research work are as follows:

- i) To model a closed three-phase solid-fluid (liquid and vapor) molecular system to represent condensation process over hybrid wetting surface.
- ii) To examine the liquid droplet nucleation and growth on condensing surface and correlate them with classical macroscale theoretical growth models.
- iii) To evaluate the performance of condensing surface with patterned and functional wettability gradient (FWG) configuration in terms of important system parameters such as condensation mass flux, wall heat flux, system energy and local interfacial surface tension distribution.
- iv) To perform a comparative analysis on condensation performance between patterned and functional wettability gradient surface for various relative hydrophilic-hydrophobic content as well as wettability contrast of hydrophilic-hydrophobic segment.

1.4 Thesis Outline

The present thesis focuses on the molecular dynamics study of nanoscale condensation phenomenon over flat hybrid wetting surface that covers the effect of hydrophilic-hydrophobic combination and patterning as well as wetting profile i.e., gradient and patterned with different wettability contrast from atomistic perspective by observing the changes in some important parameters of nanoscale condensation process such as system energy, solid-liquid energy parameter, nucleation, coalescence and growth of condensate, number of condensed atoms, condensation mass flux, condensing wall heat flux and surface tension at the liquid-vapor interface. An outline of this thesis is presented below,

Chapter 1: Introduction – a discussion about the key elements of this research, the motivation behind this research work, and research objectives.

Chapter 2: Literature Review – an overview of previous researches on the experimental and molecular dynamics study on condensation phenomena.

Chapter 3: Fundamentals of Molecular Dynamics – a description of basic elements of molecular dynamics simulation, essentials of the simulator (LAMMPS) that is used in this study.

Chapter 4: Simulation Model and Performance Parameters – describes the modelling of simulation domain and evaluation process of different transport characteristics of the study.

Chapter 5: Results and Discussions – describes the simulation model of the present study, validation of the model and discussion about the results of the study.

Chapter 6: Conclusion – summarizes the outcomes of the current research.

CHAPTER 2

LITERATURE REVIEW

Throughout the last few decades, many studies have been conducted by the researchers to characterize the different aspects of condensation phenomena. Many experimental studies have been carried out control the mode of condensation, droplet nucleation and dynamics of droplet departure for enhancing the condensation heat transfer. Along with these experimental studies, molecular dynamics simulations have also been performed for examining the nanoscale condensation characteristics from an atomistic point of view. Over the last two decades, functionally gradient materials have become so much popular among the scientists and engineers owing to its excellent thermal and mechanical properties. Experimental and atomistic studies have been carried to study various aspects of these novel materials to model and develop them according to their requirements in practical applications. In this section, relevant research works and their outcomes are discussed to provide an illustration of the contemporary experimental and molecular dynamics study on this subject matter.

Although many experimental studies have been performed to explore the phase change characteristics regarding this, atomistic simulation of these studies has become a matter of great interest nowadays with the great advancement in computational facilities. Molecular dynamics simulation has been a very effective method to investigate such phase change phenomena in the nanoscale range or atomistic viewpoint. In this section, relevant research works and their outcomes are discussed to provide an illustration of the contemporary experimental and molecular dynamics study on boiling phenomena.

2.1 Experimental study on condensation over patterned hybrid wetting surface

In recent years, researchers have developed hybrid wetting surface and performed experimental studies on condensation heat transfer in order to harness the combined effect of higher droplet nucleation and smaller droplet size.

Inspired by wettability variation of banana leaf Ghosh et al. [51] developed hybrid wetting surfaces with interdigitated patterned surfaces with hydrophilic and superhydrophilic wetting configuration. The preparation method included laser-patterned masking and chemical etching

which rendered desired wetting property in the developed material. The interdigitated hybrid surfaces resulted in 19% higher condensate collection rate than the dropwise condensation. Their results also revealed that interdigitated patterned hybrid surfaces provides better performance than the dropwise condensation hydrophobic surface in terms of droplet size and condensate collection rate.

Mahapatra et al. [52] demonstrated a facile and scalable wettability-patterning approach to promote condensate removal on a vertical metal plate during condensation in a controlled vapor environment also containing non-condensable gases (air). The approach does not apply any coatings on the metal condenser plate, thus circumventing the adverse effects of added thermal resistance. A staggered arrangement of tapered superhydrophilic wedges shown in figure 2.1, offering long wettability transition lines and capillary-driven condensate drainage helps in rapid removal of the condensate from the metal substrate. They tried to find out the optimum ratio of FWC to DWC for the enhancement of condensation heat transfer and revealed that the optimum area ratio shifted towards higher FWC fractions with rising vapor mass content in the atmosphere.

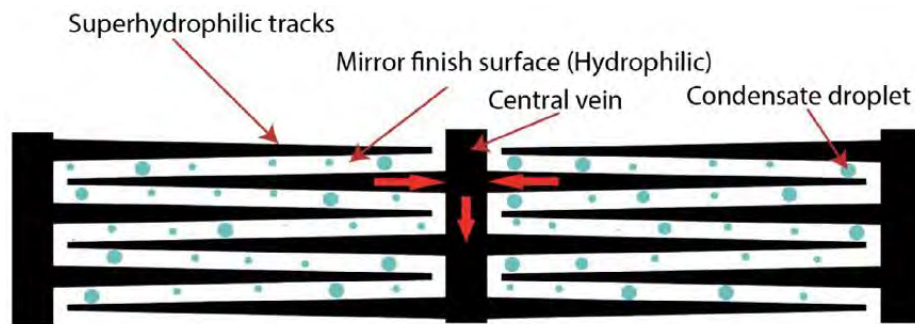


Figure 2.1: Inter-digitated design of periodically-patterned hybrid wetting surface fabricated by Mahapatra et al. [52]

Peng et al. [86] carried out experimental research on steam condensation at atmospheric pressure on various hydrophobic–hydrophilic hybrid surfaces (shown in figure 2.2) and studied the effect of maximum droplet radius and droplet population density on condensation heat transfer. They explained that reduced maximum droplet radius and increased population density are beneficial to heat transfer performance of hydrophobic region. From their research it is reported that maximum droplet radius and droplet population density is reduced with the increment of width of hydrophobic region. Considering this fact, they determined a surface with optimum hydrophilic-

hydrophobic combination and obtained 23% higher condensation heat transfer rate than the dropwise condensation on plain hydrophobic surface.

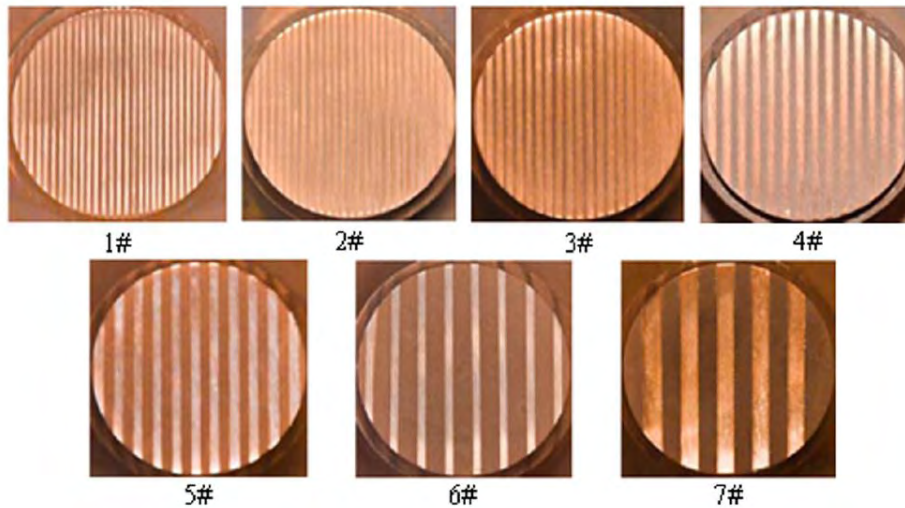


Figure 2.2: Pictures of prepared hydrophobic–hydrophilic hybrid surface by Peng et al. [86](light: hydrophobic region; gray: hydrophilic region).

Preparing hybrid wetting surface with a combination of hydrophobic-less hydrophobic surface by applying different coatings and following necessary chemical procedures Alwazzan et al. [53] determined surfaces with optimum combination of hydrophobic-less hydrophobic surface and reported that this developed hydrophobic surface offered 4.8- and 1.8-times condensation heat transfer rate than the filmwise condensation and dropwise condensation respectively due to better condensate removal and higher droplet nucleation.

For studying flow condensation heat transfer on a mini channel Derby et al. [54] they prepared hybrid wetting surface by designing the surface with hydrophilic region of copper and hydrophobic coating of Teflon. They reported that the hybrid wetting surfaces promoted the dropwise condensation mode and significantly enhanced the condensation heat transfer.

From an experimental study on hybrid wetting surface having circular hydrophilic island with hydrophobic background Chatterjee et al. [87] reported that all of the hybrid wetting surface outperformed the dropwise condensation heat transfer on hydrophobic surface in terms of condensation heat transfer coefficient. They changed the diameter of hydrophilic island from 0.25 to 1.50 mm and observed that maximum condensation heat transfer coefficient took place on

hybrid wetting surface with hydrophilic island of 0.25 mm diameter. They illustrated that at lower island diameter the coalescence of droplets took place easily, that eventually resulted in smaller maximum droplet size.

Egab et al. [88] performed a parametric study to examine the heat transfer performance on different hybrid surfaces. They conducted their experiments on both hydrophilic islands on a hydrophobic background surface and hydrophobic islands on a hydrophilic background surface. They used different island and pitch sizes to find the optimal conditions, which showed an enhancement of 79% in heat transfer rate compared to that of complete dropwise condensation.

2.2 Experimental study on condensation over nanostructured hybrid wetting surface

Previously, researchers have developed hybrid wetting surfaces with nanostructured configurations to perform experimental study on condensation over hybrid wetting surface. From the results of these studies, it is reported that hybrid wetting surfaces with various nanostructured configurations performed better than the homogeneous surfaces i.e., hydrophilic and hydrophobic/superhydrophobic in terms of condensation heat transfer enhancement due to higher nucleation and better droplet removal rate. The summary of these experimental studies is discussed in this section.

Varanasi et al. [55] prepared hybrid wetting surface (shown in figure 2.3) for analyzing the heterogeneous nucleation of water droplet. They showed that textured hydrophobic surfaces with hydrophilic tops promote nucleation and growth of Cassie-type droplets and can therefore exhibit superior droplet shedding properties under condensation. As a result, these hybrid surfaces have a great potential to enhance condensation heat transfer and could broadly lead to efficient condensers in power generation and cooling of electronic devices.

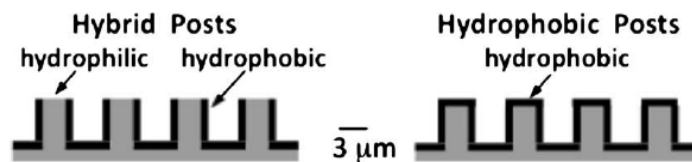


Figure 2.3: Schematic of microstructured hybrid wetting surface prepared by Varanasi et al. [89]

In an experimental study on micro grooved silicon nanowire surface of hybrid wettability Lo et al. [45] observed that the cycle time (i.e., the time required to complete a cycle from droplet nucleation to droplet departure) on the micro grooved silicon nanowire surface is ten times smaller than that on a plain silicon surface and resulted in higher heat transfer coefficient on the micro grooved silicon nanowire surface. They also tried to figure out the effect of groove width on the nucleation density and observed that it increases with decrement of groove width.

Chen et al. [44] developed a hierarchical nanograsSED micropyramidal architecture that promotes drop nucleation as well as drop departure without compromising each other. Specifically, the presence of wettable patches facilitates drop growth and preferential coalescence whereas the global superhydrophobicity promotes spontaneous drop departure without pinning to the substrate. With this surface morphology, they obtained 65% increase in droplet nucleation and 450% increase in droplet removal after nucleation in comparison with superhydrophobic nanostructured surface for water vapor condensation.

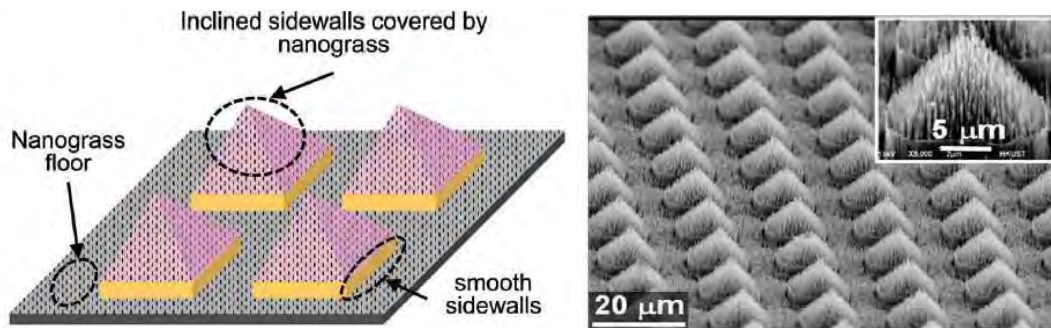


Figure 2.4: Schematic drawing (left) and scanning electron microscopy (SEM) image of nanograsSED micropyramid arrays (right) prepared by Chen et al. [44]

Hou et al. [56] reported the development of a bioinspired hybrid surface with high wetting contrast that allows for seamless integration of filmwise and dropwise condensation modes. They showed that the synergistic cooperation in the observed recurrent condensation modes leads to improvements in all aspects of heat transfer properties including droplet nucleation density, growth rate, and self-removal, as well as overall heat transfer coefficient. By designing a surface with hydrophilic micropillars on hydrophobic nanograsSED surface and obtained 63% enhancement in condensation heat transfer coefficient in water vapor condensation compared to flat hydrophobic surface.

In an experimental study on grooved wettability gradient surface, Tokunaga and Tsuruta [57] found that the size of the droplets could be controlled by modifying the pattern width and the wettability gradient could be used to remove large droplets and their study revealed that heat transfer coefficient was enhanced by three times compared with the results of the microstructured condensing surface with a straight pattern.

Shang et al. [90] developed a mathematical model for condensation heat transfer over biphilic nanostructured surface including necessary thermal resistances that affects condensation heat transfer through a single droplet and thus the overall heat transfer. They also modelled the droplet size during its dynamic growth over a biphilic surface having hydrophilic micropillar and hydrophobic nanopillars and found that droplet size decrease with the decrement of micropillar size. They also found that overall heat transfer depends both on the pillar diameter and the spacing between them.

2.3 Molecular dynamics study on condensation phenomena

With the existing experimental setup, it is difficult to properly visualize some important aspects of nanoscale condensation phenomena such as nucleation, coalescence, and growth of condensate layer. To overcome these difficulties, with the rapid advancement in computational technology, molecular dynamics (MD) simulation has become very popular among researchers of various fields for having a deeper insight and better visualization of the condensation process. The summary of the earlier MD studies on this subject matter are discussed in this section.

Liang et al. [91] performed non-equilibrium molecular dynamics (NEMD) study on transient evaporation and condensation phenomena and reported that results from MD simulation matches with the results of classical kinetic theory of gas like Schrage relationship. The simulation of their study is depicted in figure 2.5.

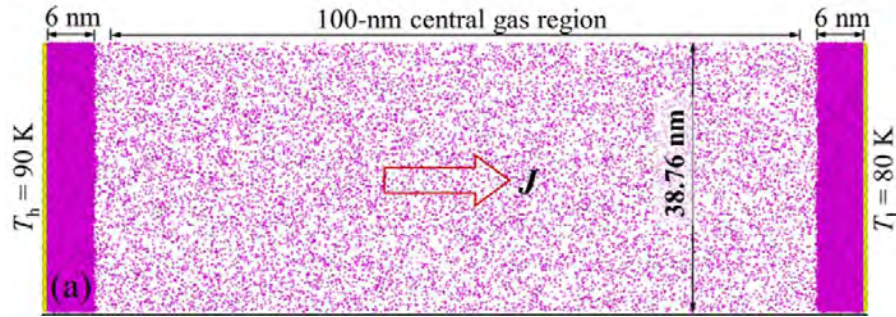


Figure 2.5: Simulation domain for the MD study performed by Liang et al. [91].

Sheng et al. [68] conducted MD study of condensation of water molecules on surfaces having different wettability. The different wettability surfaces were modelled by changing the solid-liquid energy parameter. They found that the condensation mode is highly dependent on the solid-liquid energy parameter. The reported critical values of solid-liquid energy parameter which controls the different condensation modes i.e., no condensation, dropwise condensation and filmwise condensation.

In a similar atomistic study Pu et al. [73] illustrated that at the condensate film has a tendency to rupture and develop dropwise condensation on surfaces with smaller solid-liquid energy parameter. They also showed that higher temperature difference between vapor and solid surface leads to filmwise condensation mode compared to the lower ones.

Through MD simulation Niu and Tang [34] studied the effect of surface wettability in condensation at nanoscale. They reported that in nanoscale the solid-liquid interfacial thermal resistance plays the most dominant role in condensation heat transfer which is quite different from the conventional behaviour at macroscale. They observed that hydrophilic surfaces cause lower solid-liquid interfacial thermal resistance than the hydrophobic ones. For this reason, hydrophilic surface offers higher condensation heat transfer than the hydrophobic one.

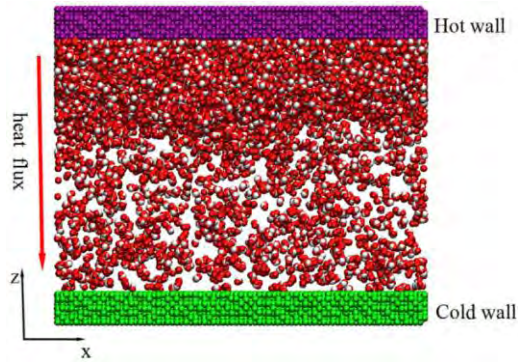


Figure 2.6: Simulation setup of Pt-water system modelled by Niu and Tang [34].

In their MD study, Yang et al. [35] observed a similar effect of wettability on condensation heat transfer efficiency. They also determined the effect of vapor temperature on condensation heat transfer efficiency and reported that condensation heat transfer efficiency increases with the increment of vapor temperature. They also showed that the results of their study follow the classical nucleation theory.

Wang and Keblinski [82] demonstrated the effect of solid-liquid interaction energy parameter on interfacial thermal resistance at the solid-liquid interface in case of both rough and smooth surface. They illustrated that solid-liquid interaction parameter changes the wettability of the surface thus changes the solid-liquid contact area of the surface. From the results they reported that among all the parameters the solid-liquid interaction energy parameter is the most important one to affect the solid-liquid interfacial thermal resistance.

From their MD study on the relative effect of solid-liquid interfacial thermal resistance and bulk thermal resistance on condensation heat transfer, Sun and Wang [92] reported that at the earlier stage the solid-liquid interfacial thermal resistance plays the most dominant role on condensation heat transfer. But with time, the thickness of condensate layer is increased which results in the increment of bulk thermal resistance. At one point, the effect of bulk thermal resistance surpasses the solid-liquid interfacial thermal resistance and plays the dominant role at the later stage of condensation. They also showed that time required for this incident to take place is increased with the decrement of solid-liquid interfacial interaction energy parameter.

From their MD study on condensation of water over mica surface Ou et al. [72] found that the development and growth of the condensate film depend on the surface properties. They showed

that the formation of first adlayer is heterogeneous due to different adsorption affinities to various surface sites. The second water adlayer begins to emerge even when some surface sites are still empty: the water molecules adsorbed in the preferential binding sites can effectively recruit other water molecules. The condensation process of water film on the mica surface resembles the process described by the Stranski-Krastanov (S-K) growth model, i.e., the formation of the first adlayer followed by island growth.

Deng et al. [84] illustrated the effect of wettability gradient on the motion of droplet by numerically analysing through Lattice-Boltzmann method. They delineated that during condensation phenomena the droplet has a tendency to spontaneously migrate from low surface energy regions (hydrophobic) to high surface energy region (hydrophilic). They also showed that at higher wettability gradient the motion is enhanced which is conducive to condensation heat transfer.

While studying the thermodynamic properties at the solid-liquid interface by using different fluid substances such as non-polar argon, polar water, straight chain alkanes like butane, octane and dodecane Nagayama et al. [93] found no dependence of the structure of the molecules on the thermodynamic properties at the solid-liquid interface during the condensation process.

Rashidi et al. [80] performed MD simulation with a view to study the effect of roughness on condensation flow in a nanochannel. They employed two different roughness geometry i.e., rectangular and conical and varied the height of the roughness. They showed that both the shape and height of the roughness affect the velocity of flow and thus alter the condensation heat transfer. From the results they reported that with the increase of roughness height the velocity of flow is reduced which increases the condensation heat transfer. They also revealed that condensation heat transfer is higher with the roughness of rectangular cross-section than the conical ones.

The effects of pillar height, pitch distance of nanopillars, wall subcooling and wettability on condensation are discussed in the MD study of Huang et al. [94] on condensation of Argon vapor on nanopillar array surfaces made of copper. It is found that higher pillars, denser pillars and stronger wall surface wettability can suppress vapor condensation at the bottom of a nanopillar array, making vapor more likely to condense in the upper section of the array. It is also shown that the condensation peak in the nanopillar array can be shift from bottom to top with the increasing wall subcooling and wettability.

Xu and Chen [75] performed MD simulations to study condensate drainage on wedge shaped wettability gradient surface having higher wettability on wedge shaped portion than the flat portion. They observed that hydrophobic-hydrophilic combination offered highest condensate drainage compared to the superhydrophilic-hydrophilic and hydrophobic-superhydrophobic combination.

From the MD study on the effect of different wall temperatures on the annular condensation of vapor Argon through a nanochannel Ghahremanian et al. [95] found that the wall temperature does not have a significant effect on the vapor and liquid density, while the heat flux value increases with the increase of wall temperature.

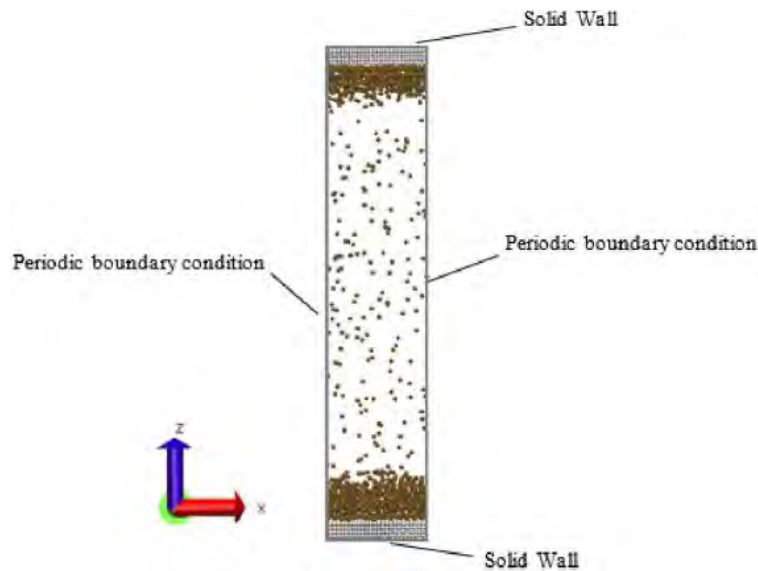


Figure 2.7: Simulation domain for the MD study performed by Ghahremanian et al. [95].

Li et al. [81] performed MD simulations on surfaces with nanostructures and found that higher surface area of nanostructured configurations results in higher condensation heat transfer rate. From their findings they showed that surface area is not the only parameter that affects the condensation heat transfer. They showed that the height and spacing of the nanostructures also play an important role in condensation heat transfer process over nanostructured surface.

FUNDAMENTALS OF MOLECULAR DYNAMICS

3.1 Molecular Dynamics Simulation

A computer simulation method called molecular dynamics (MD) is used to explore the physical motions of atoms and molecules. It is used to determine the qualities of molecular assemblies in terms of structure and microscopic interaction. The atoms and molecules are allowed to interact for a fixed amount of time, resulting in a picture of the system's dynamic evolution, and then the trajectories of the atoms and molecules are determined using appropriate techniques. It combines the old mechanistic tradition from the time of Pierre Simon de Laplace and the new concept of atoms and molecules introduced at the beginning of the 20th century. Microscopic simulations are used to analyze macroscopic properties of a system, while statistical mechanics is used to study a macroscopic system from a molecular perspective to make the connection between microscopic simulations and macroscopic properties. The equilibrium qualities of a liquid made up of hard spheres were the first thing to be studied using this method [96,97]. However, with the advancement of current computers, researchers can now employ them in subjects such as physics [96], biology [98], structure refinement [99], and so on.

Because of the corresponding length scales, several instrumentation issues occur frequently in nanoscale experimental research, and the system is therefore discretely modelled from an atomistic viewpoint. Generally, three basic steps are considered for a molecular-scale simulation: (a) model construction, (b) evaluation of molecular trajectories, and (c) analyzing those trajectories to get property values [100]. A pure continuum explanation of fluid motion in these situations is obviously inaccurate. Hence, first of all the length scale of a problem has to be judged to go further for a system modelling. Numerous important physical models with their corresponding length and time scales are shown in figure 3.1.

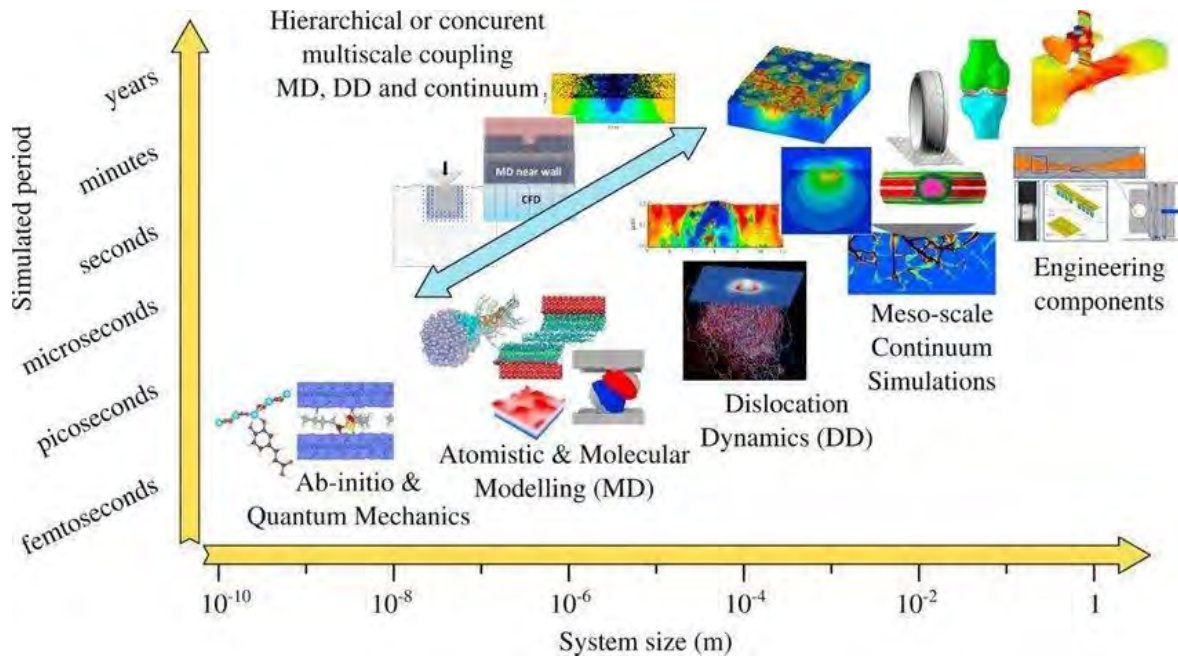


Figure 3.1: Range in various time and length scales used in modelling [101].

The nature of atoms and subatomic particles at the tiniest scales of energy levels is described by quantum mechanics, which is a fundamental theory in physics. A complex wave function, also known as a state vector in a complex vector space, defines the state at a given time in quantum mechanics. This abstract mathematical object allows to analyze the probabilities of different experiment outcomes. Quantum modeling is extremely accurate, but the high computing cost prevents it from being used in interphase phenomena. Mesoscopic physics is utilized with materials of intermediate length, and the scale of these materials can be characterized as the difference between the nanoscale size of atom quantity and the micrometer-scale size of materials. Macroscopic scale is used when dealt objects are enough large that can be visualized with naked eye without the help of optical instruments for magnifying. That is why, molecular dynamics simulation has gained a lot of attraction from the researchers in order to modelling the characteristics of atom such as position, velocity, movement etc. in case of non- equilibrium system of condensation phenomena. Accurate experimentation in this very small scale of length and time is very complex and sometimes impossible. Even, if possible, it also costs very high for the delicate experiment. So, the MD simulation is now an obvious for rapid research and development.

The system is modeled as an ensemble of interacting particles, which includes molecules, atoms, and fractions of molecules in molecular dynamics simulations. The molecule's nuclei motion, which is

determined classically and is known as mass points [102], is a good fit for the system dynamic. The mathematical method used to evaluate the interactions of the particles in the simulation is determined by the type of particles in the simulation. A potential, or more technically, a functional, clarifies the positions of the nuclei.

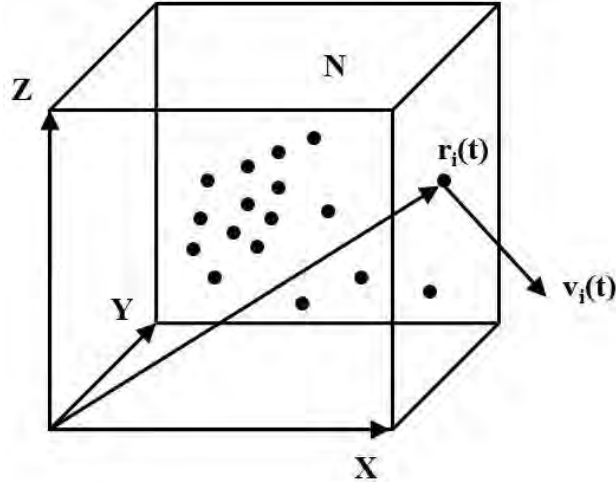


Figure 3.2: Molecular dynamics simulation system as a collection of N particles in a particular volume.

A system considering as in the figure 3.2 composed of N particles gives the equations of motion are as follows:

$$m_i \dot{v}_i = -\frac{\partial \phi}{\partial r_i}, \quad i = 1, 2, 3, \dots, N \quad (3.1)$$

$$\dot{r}_i = v_i, \quad i = 1, 2, 3, \dots, N \quad (3.2)$$

Here, m_i denotes the mass of the i -th particle, r_i is its position, v_i is the velocity, and ϕ is the interaction potential of the entire system. The $6N$ first-order Newtonian ordinary differential equations can be used to model the system's behavior. The equations of motion can be solved using a variety of techniques or algorithms, which will be explained in detail in the following sections of this chapter. To carry out a good molecular dynamics simulation, one must utilize a reliable and efficient algorithm that can solve the $6N$ Newtonian ordinary differential equations and use ideal potentials to accurately depict particle interactions.

3.1.1 Advantages of Molecular Dynamics

In comparison to other simulation methodologies, molecular dynamics simulation offers a number of computational advantages. Some of them are mentioned below:

- Molecular dynamics (MD) takes only the positions and interactions between the atoms as input and solves the equation of motion using Newton's law to predict the atoms' future trajectories.
- Molecular dynamics serves as an important computational experiment or trial because it solves the problem without making any prior assumptions. As a result, the post-processing of MD simulation can yield novel discoveries or suggestions.
- MD simulation can provide crucial guidance for multi-scale modeling.
- In the field of thermal engineering, MD simulation may predict macroscopic transport parameters using atomistic data. The time-averaged technique is utilized in MD simulation to produce the thermodynamic properties, and so the phase diagram of a certain material may be evaluated using this technique.
- MD simulation can be a useful tool for non-equilibrium process optimization.

3.1.2 Limitations of Molecular Dynamics

Although molecular dynamics simulation is a powerful computational tool, it is not without its limitations. The following are some of the major limitations of molecular dynamics simulation:

- The length- and time-scale associated with traditional molecular dynamics simulations is the most significant restriction. In traditional MD, the time-step resolution for determining the average properties of a macroscopic system must be roughly 10^{-15} s. However, in practice, completing a basic microsecond scale simulation would take at least several months, which is a major limitation of MD simulation. As a result, determining the bulk characteristics from a molecular dynamics simulation is nearly impossible in most circumstances. The length-scale in traditional MD simulation is in the nanoscale range (10^{-9} m). In addition, the time it takes to finish a simulation is exactly proportional to the number of atoms involved. Typical MD simulations can handle millions of atoms, which in many circumstances may not be feasible.

- Atoms directly interact with one other in molecular dynamics, and these interactions generate forces that operate on atoms, causing atoms to move under the influence of these instantaneous forces. These interatomic forces are the most essential factor in the physics of classical molecular dynamics modeling. If the interatomic forces in the simulation match the forces of the real atoms, the simulation will be realistic or completely imitate the behavior of the real system. The choice of the perfect interatomic potential to recreate the behavior of real atoms in the simulation is now a significant topic. In many circumstances, we must rely on simplified interatomic potentials, which severely limits our ability to derive real system features from simulations.

3.1.3 Steps of Molecular Dynamics Simulation

Figure 3.3 denotes the main algorithm behind the MD simulation.

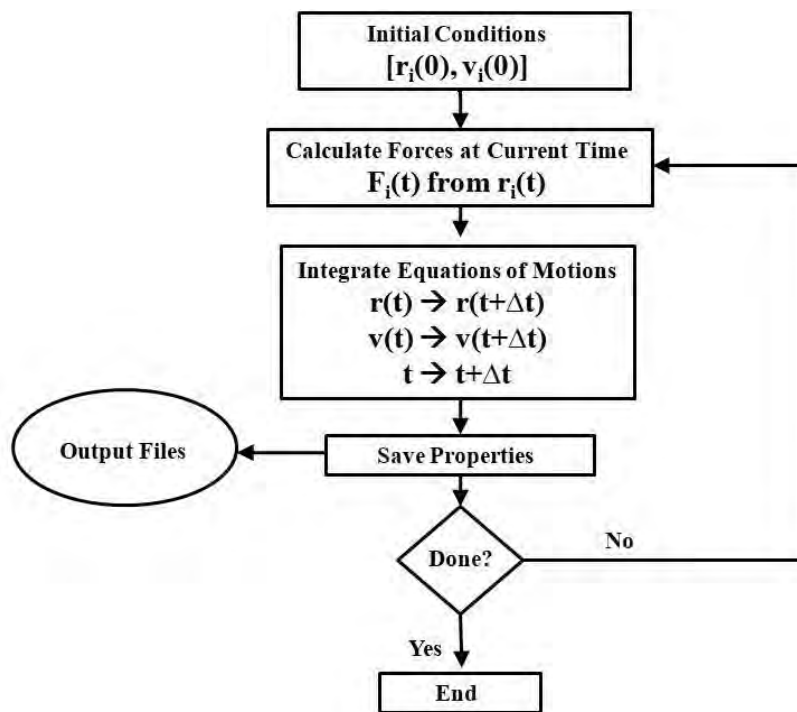


Figure 3.3: Fundamental algorithm followed for solving classical molecular dynamics simulation.

The basic steps of classical molecular dynamics [100] are briefly presented below:

- At the beginning of the MD simulation, the system of particles has to be perfectly defined. This definition includes the initial position and velocity of the particles.
- Then, the expression of forces has to be obtained by selecting appropriate interatomic potential function.
- Next, the energy of the structure has to be minimized.
- After that, Newton's equation of motion has to be solved by a suitable technique.
- Then, the positions and velocities of the atoms in the system have to be updated for an incremental time-step.
- Finally, the obtained data from the simulation has to be analysed with the help of the statistical approach.

3.1.4 Potential function

Interatomic interactions in molecular dynamics simulations are defined by a force field or potential. This is referred to as a force field in chemistry and biology, and as an interatomic potential in materials physics. The potential energy of N atoms varies with the atoms' co-ordinate in a system, as explained by the potential function, $\phi(r_1, r_2, \dots, r_N)$. To evaluate these potential functions, a variety of methods are utilized, some of which are detailed below:

- For empirical potential functions, the parameters are chosen assuming a functional form for the intended potential function to reproduce a set of experimental data (e.g. Lennard-Jones [103], Morse [104], etc.).
- For fixed placements of atoms, calculating the electronic wave for a system made of numerous atoms is challenging. To analyze the semi-empirical potentials derived from quantum-mechanical considerations, many assumptions are made. Embedded Atom Method (EAM) by Daw et al. [105], Tersoff potential [106], Brenner potential [107], and others are some instances.
- Several approximations are utilized in Ab-initio MD simulation [108](e.g. Car and Parrinello approach employing plane wave pseudo potentials) based on theoretical considerations rather than empirical fitting. In the case of empirical approaches, ab initio computations generate a large amount of data, which is inconvenient. Calculation of the

density of electronic states or other electronic parameters of the system are examples of this.

The following things are considered when choosing an appropriate potential function for molecular dynamics model:

1. Accuracy (reproduction of interested properties as closely as possible)
2. Transferability (can be utilized to analyse different of properties for which it was inaccurate)
3. Computational speed (Fast calculation with simple potentials)

Determining appropriate potential is critical, because it varies greatly depending on the materials used, the nature of the task, and the computing resources available. For material science, thermal flaws, and other applications, great precision is necessary, while computational speed is concentrated as a collective character run for long periods of time.

The Born-Oppenheimer adiabatic approximation [109] is used to create atomistic simulations. This is one of the most essential principles for defining quantum states of molecules and allowing nuclei and electron movements to be distinguished. It separates the wave function into electronic and nuclear parts mathematically, with electrons in their ground state and nuclei moving.

An expansion of ϕ in terms of one-body, two-body and N-body interactions for the considered nuclear motions are given as follows:

$$\phi(r^{3N}) = \sum_{j=1}^N \phi_1(r_j) + \sum_{i<j}^N \phi_1(r_i, r_j) + \sum_{i<j<k}^N \phi_1(r_i, r_j, r_k) \quad (3.3)$$

Here, in equation 3.3,

- The first term stands for the sum of one-body interactions
- The second term indicates the contribution of pure two-body interactions (pairwise additive).
- The third sum denotes pure three-body interactions.

The list of different types of potential are discussed as follows:

(i) Pair Potentials

It is the simplest way to define an interaction, in which total potential energy is calculated from the sum of energy contributions between pairs of atoms. By summing the effective potentials of pairings, the potential can be found $\phi(r_{ij})$,

$$\phi = \sum_i \sum_{i < j} \phi(r_{ij}) \quad (3.4)$$

Pair potential functions used in computational cases are described below:

- **Hard/Soft spheres:** Hard spheres are impenetrable spheres that cannot overlap in space, but soft sphere potential is finite at interatomic separations less than the diameter of the sphere. There is no consideration of any coherent interplay in these potentials.

$$\phi(r_{ij}) = \begin{cases} \infty, & \text{for } r_{ij} \leq r_0 \\ 0, & \text{for } r_{ij} \geq r_0 \end{cases} \text{ for hard spheres} \quad (3.5)$$

$$\phi(r_{ij}) = \left(\frac{r_{ij}}{r_0}\right)^{-n} \text{ for soft spheres} \quad (3.6)$$

- **Ionic:** The ionic potential is the ratio of an ion's electric charge to its radius. To account for charge-charge interaction or polarization, this is frequently appended to other functional forms.

$$\phi(r_{ij}) = \frac{q_i q_j}{r_{ij}} \quad (3.7)$$

- **Lennard-Jones potential:** The Lennard-Jones (LJ) potential [69] is the most common and widely utilized paired potential function. This is a straightforward mathematical model that approximates the interaction of two neutral atoms or molecules. Despite the fact that this potential does not take into account any complex factors (such as bond angle or electron density), it is commonly employed to describe the properties of gases and to predict dispersion and overlap interactions in molecular models due to its computational simplicity. This potential function was first proposed for liquid argon or Lennard-Jones fluid. The distance between two atoms i and j located at r_i and r_j is r_{ij} , and the potential energy as given by the LJ potential is:

$$\phi(r_{ij}) = 4\varepsilon \left\{ \left(\frac{\sigma}{r_{ij}} \right)^{12} - \left(\frac{\sigma}{r_{ij}} \right)^6 \right\}, r_{ij} < r_{cut} \quad (3.8)$$

$$\phi(r_{ij}) = 0, r_{ij} > r_{cut} \quad (3.9)$$

Here, ε governs the strength of the interaction, and σ is the finite distance at which the interparticle potential is zero. The r_{ij}^{-12} term, which is the repulsive term, describes Pauli repulsion at short ranges due to overlapping electron orbitals, and the r_{ij}^{-6} term, which is the attractive long-range term, describes attraction at long ranges (van der Waals force, or dispersion force). Significant computation time can be saved by neglecting pair interactions beyond a cut-off radius (r_{cut}). In this study, Lennard-Jones (LJ) potential is used for all the computational cases.

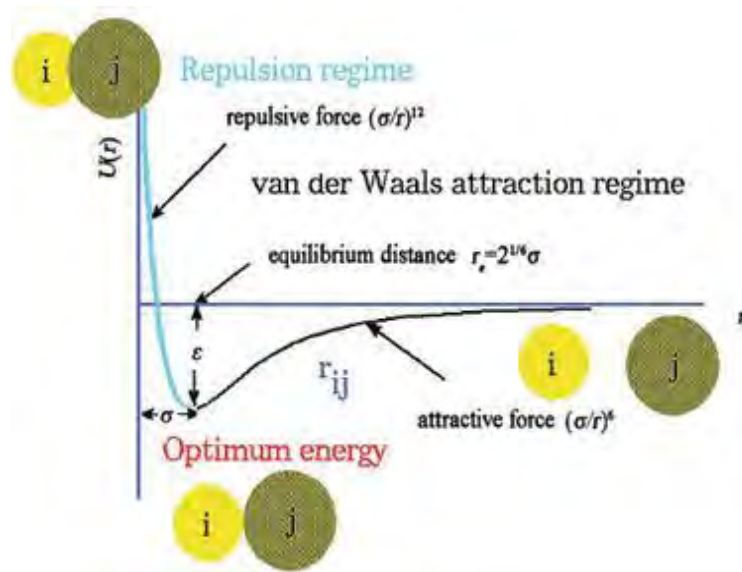


Figure 3.4: LJ potential between two atoms i and j [110].

- **Morse potential:** The Morse potential [104] is a convenient interatomic interaction model for a diatomic molecule's potential energy, and it explicitly includes bond breaking effects such as the presence of unbounded states. It's a common option for modeling metals with face-centered cubic (fcc) and hexagonal closed packed (hcp) structures.

$$\phi(r_{ij}) = \varepsilon [e^{-2\alpha(r_{ij}-r_0)} - 2e^{-\alpha(r_{ij}-r_0)}] \quad (3.10)$$

Here, r_{ij} denotes the distance between the atoms, r_0 is the equilibrium bond distance, and α controls the width of the potential.

(ii) Many body potentials

In many computational cases, oversimplification in the representation of interaction in the pair potential can lead to major errors. For example, the interaction between atoms is very different from the interactions within a bulk material. Pair potentials can also underestimate the stable stacking fault energy [111] and are unable to describe the elastic anisotropy in cubic crystals in the case of nanoindentation. Many body potentials can circumvent these constraints because they consider the bond energy between atoms as a function of not only distance but also the locations of all other atoms in the vicinity of that atom [112].

The following are some of the most popular many body potentials models:

- **Embedded Atom Model (EAM):** Ionized atom cores with a "sea" of delocalized valence electrons are seen in metals. Embedded atom model [105,113] may completely describe metals and alloys, and the EAM potential consists of a term similar to simple LJ potential and correction for the local environment. This potential is special in that it takes into account the local electronic density on an atom that is influenced by adjacent atoms. The total potential energy in EAM potential is represented as in equation 3.11,

$$V_{TOT} = \sum_i^N F_i \left(\sum_j \rho(r_{ij}) \right) + \frac{1}{2} \sum_{i,j}^N V_2(r_{ij}) \quad (3.11)$$

$$\rho_i = \sum_j f(r_{ij}) \quad (3.12)$$

Here, F_i denotes the embedding function which is a function of the sum of the electron density $\rho(r_{ij})$. V_2 is a pair potential that usually is purely repulsive and $f(r_{ij})$ represents the electron density function at atom i due to atom j . The main advantage of this method over pair potential is the ability to describe the variation of the bond strength with coordination. The increase of coordination decreases the strength of each of the individual bonds and increases the bond length.

Bond order potentials: These potentials have an advantage over traditional molecular mechanics force fields in that they can describe numerous distinct bonding states of an atom with the same parameters, and hence may be able to correctly analyze chemical interactions to some extent. Bond order potentials, such as Tersoff-like [106] or Brenner potentials [107], are frequently used to describe covalently bound materials. Also, the ReaxFF potential [114] can be considered as a bond order potential, allowing for continuous bond formation and breaking. The generalized form of the bond order potentials has been given below:

$$V_{ij}(r_{ij}) = V_{repulsive}(r_{ij}) + b_{ijk}V_{attractive}(r_{ij}) \quad (3.13)$$

Here, the repulsive and attractive parts are simple exponential functions similar to those in the Morse potential. However, the strength of the bond is modified by the environment of the atom i via the b_{ijk} term.

3.1.5 Time integration algorithm

Newton's 2nd law of motion is used in the molecular dynamics simulation. It is possible to determine the acceleration of each atom if we know the force acting on it. When the equation is integrated, a trajectory is produced that describes the locations, velocities, and accelerations of each atom as they change over time. The state of the system may be predicted at any time once the locations and velocities of each atom are known. potential energy (force) is a function of $3N$ atomic positions. The equations of motion have no analytical solution and must be solved numerically. The time step for integration should be carefully chosen.

Some common integration algorithm schemes which are frequently used in MD simulation are discussed below:

3.1.5.1 Verlet algorithm

The Verlet algorithm [115] for MD integration is a straightforward application of the two equations given below which are derived from Taylor's series expansion,

$$r(t + \Delta t) = 2r(t) - r(t - \Delta t) + a(t)(\Delta t)^2 \quad (3.14)$$

$$v(t) = \frac{r(t + \Delta t) - r(t - \Delta t)}{2\Delta t} \quad (3.15)$$

In this simple integration scheme, the position of atoms at $t + \Delta t$ is calculated based on the current positions, $r(t)$ and forces, $F(t)$ and the previous positions, $r(t - \Delta t)$. Here, acceleration $a(t) = F(t)/m$ and the integration does not require the velocities, only position of the atoms is taken into account. This is the simplest integration scheme and has good stability but velocities of the atoms are not explicitly solved and that's why this algorithm lacks in accuracy.

3.1.5.2 Leap-Frog Algorithm

Leap-frog integration is equivalent to updating positions and velocities at interspersed time points. The updating equations are given below:

$$v\left(t + \frac{\Delta t}{2}\right) = v\left(t - \frac{\Delta t}{2}\right) + a(t)\Delta t \quad (3.16)$$

$$r(t + \Delta t) = r(t) + v\left(t + \frac{\Delta t}{2}\right)\Delta t \quad (3.17)$$

The velocities are updated at half time steps and 'leap' ahead the positions. The current velocities can be obtained from the following equation,

$$v(t) = \frac{v\left(t + \frac{\Delta t}{2}\right) + v\left(t - \frac{\Delta t}{2}\right)}{2} \quad (3.18)$$

The velocities are determined explicitly in this numerical method, which reduces the numerical error problem of the Verlet algorithm. But, because velocities are not measured at the same time as positions, kinetic energy contribution to total energy cannot be estimated at the same time as positions are established.

3.1.5.3 Velocity-Verlet Algorithm

Velocity-Verlet algorithm [116] is the widely used numerical scheme where the velocity and position are calculated at the same value of the time variable. This algorithm consists of the following steps:

- Starting with the position and velocity expansions similar to the basic Verlet algorithm,

$$r(t + \Delta t) = r(t) + v(t)\Delta t + \frac{1}{2}a(t)(\Delta t)^2 \quad (3.19)$$

$$v(t + \Delta t) = v(t) + a(t)\Delta t \quad (3.20)$$

- Calculation of the velocities at mid interval as $v(t + \frac{\Delta t}{2})$,

$$v\left(t + \frac{\Delta t}{2}\right) = v(t) + a(t)\frac{\Delta t}{2} \quad (3.21)$$

- Calculation of the positions at the next step,

$$r(t + \Delta t) = r(t) + v\left(t + \frac{\Delta t}{2}\right)\Delta t \quad (3.22)$$

- Calculation of the accelerations at the next step from the potential,

$$a(t + \Delta t) = F(r(t + \Delta t))/m \quad (3.23)$$

- Updating the velocities,

$$v(t + \Delta t) = v\left(t + \frac{\Delta t}{2}\right) + a(t + \Delta t)\frac{\Delta t}{2} \quad (3.24)$$

This method is more accurate than the others in terms of calculating velocities and is more stable than the predictor-corrector systems. The only disadvantage is that this method is more computationally expensive than the leap-frog algorithm. This algorithm is utilized to run all of the simulations in this study.

3.1.5.4 Predictor-Corrector Algorithm

This algorithm involves the following steps:

- Prediction of the system configuration at the end of the next time step using Taylor expansion
- Evaluations of the forces at the next time step using the predicted system state; the difference between the predicted and newly calculated acceleration is the error.
- Correction of all the next step values by using the error calculated in the previous step

Predictor-corrector approaches provide higher accuracy than the Verlet method but require extra computations and memory.

3.1.6 Boundary Conditions

In a molecular dynamics simulation, the necessary boundary conditions are used to solve Newton's equation of motion. These boundary conditions should match the physical restrictions of the simulation's computational experiments. Different types of boundary conditions exist, such as fixed or rigid boundaries, semi-rigid boundaries, and periodic boundaries. The computational domains in this study are in the form of a cuboid simulation cell with six boundaries, two in each of the x, y, and z dimensions. Periodic boundary [117] and fixed boundary conditions were used in this investigation. These two forms of boundary conditions are discussed in depth in the following sections.

3.1.6.1 Periodic Boundary Condition

Periodic boundary conditions (PBCs) are a collection of boundary conditions used to approximate a large (infinite) system using a small component known as a unit cell. Periodic boundary conditions allow a simulation to be run with a small number of particles while the particles are subjected to the same forces as if they were in a bulk solution. If an atom goes out of the simulation box in one direction, it re-enters with the same velocity from the opposite direction under these boundary conditions. As image cells, the primary cell is copied in all simulated directions. Both the primary and image cells have the same quantity, position, momentum, size, and shape of atoms.

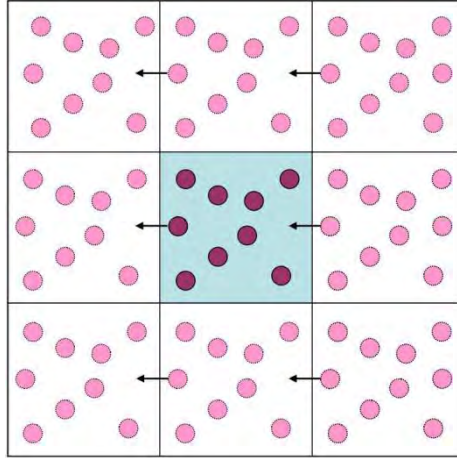


Figure 3.5: Periodic boundary condition (Basic cell is replicated in all the directions).

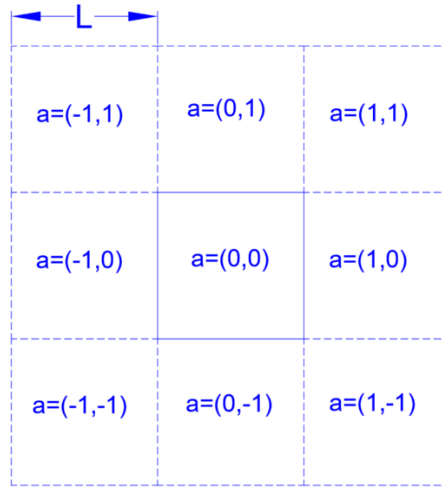


Figure 3.6: Coordinates of primary and image atoms in periodic boundary condition.

In figure 3.6, the coordinate of the basic cell is $a = (0,0)$. Under periodic boundary conditions, it has been replicated in all the directions. The forces between the primary and image atoms are shown in the following equations,

If i and j are in the primary cell,

$$\vec{F}_i = - \frac{\partial U(\vec{r}_{ij})}{\partial \vec{r}_i} \quad (3.25)$$

If j is in an image cell,

$$\vec{F}_i = - \sum_{\vec{\alpha}} \frac{\partial U(\vec{r}_{ij} - \vec{\alpha}L)}{\partial \vec{r}_i} \quad (3.26)$$

3.1.6.2 Fixed boundary condition

Non-periodic or fixed boundaries are utilized in some circumstances to prevent particles from interacting over the border and moving from one side of the simulation box to the other. Fixed boundary conditions should be utilized with caution because an atom may be lost if it moves outside the face. A rigid or fixed atomistic wall is depicted in figure 3.7.

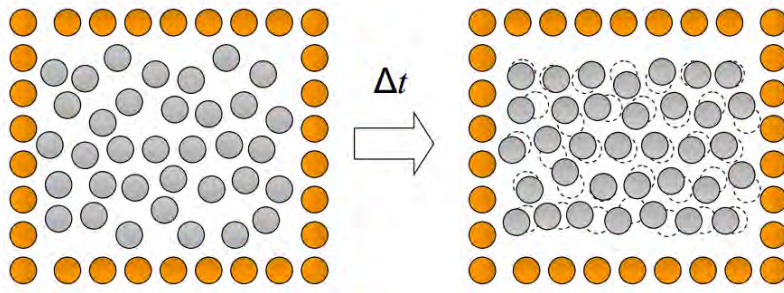


Figure 3.7: Fixed boundary condition (Atomistic rigid wall).

3.1.7 Temperature and pressure control

Thermostatting refers to managing the temperature of the particles in a molecular dynamics simulation, whereas barostatting refers to manipulating the pressure. A target temperature (T) and/or pressure (P) for a system is often set, and the Thermostat or Barostat attempts to equilibrate the system to the desired T and/or P. The Boltzmann constant is used to calculate temperature as kinetic energy divided by a number of degrees of freedom. LAMMPS is employed as the molecular dynamics simulator in this investigation. In LAMMPS, there are numerous ways for thermostatting the system, including Nose-Hoover (NVT), Berendsen, Langevin, and direct rescaling, among others. The Langevin thermostat was utilized in this study to control the temperature of a group of atoms in all circumstances. In Langevin thermostat, fewer computations per time step is needed since many atoms can be eliminated and be included implicitly by stochastic term. Besides, it is possible to choose a larger timestep while using Langevin thermostat. In addition, two barostatting methods are currently available in LAMMPS which are Nose-Hoover (NPT and NPH) and Berendsen methods.

3.1.7.1 Langevin dynamics

Langevin dynamics is a method for describing the dynamics of molecular systems using mathematics. The technique is characterized by the employment of reduced models with stochastic differential equations to account for neglected degrees of freedom. In the real world, a molecular system is unlikely to exist in a vacuum. Friction is caused by the jostling of solvent or air molecules, and the system is occasionally perturbed by a high-velocity collision. Langevin dynamics tries to account for these phenomena by extending molecular dynamics. Furthermore, Langevin dynamics enables temperature control similar to that of a thermostat, thus approaching the canonical ensemble.

For a system of N particles with masses M , the resulting Langevin equation is given below,

$$m_i \frac{d^2 r}{dt^2} = F_i(r) - M\gamma \frac{dr}{dt} + R_i(t) \quad (3.27)$$

Here, γ represents the collision frequency which can control the magnitude of the frictional force and the variance of the random forces. It ensures that the system converges to Boltzmann distribution. The larger its value, the greater the influence of the surrounding fluctuating force. $R_i(t)$ is a random force vector, which is a stationary Gaussian process with zero mean. To perfectly control the temperature, one needs to use the small value of γ .

3.1.8 Statistical ensembles

A collection of all feasible systems with distinct microscopic states but the same macroscopic or thermodynamic state is referred to as an ensemble. A statistical ensemble is an idealization that consists of a large number of virtual copies of a system that are all studied at the same time and each of which represents a possible state for the real system. A statistical ensemble, in other terms, is a probability distribution for the system's state. Different statistical ensembles can be used in molecular dynamics simulations to manage temperature and pressure. Gibbs [118] defined the most important thermodynamic ensembles, which are shown here,

- **NVE ensemble** – By solving Newton's equation without any temperature or pressure control, the constant-energy, constant-volume ensemble (NVE), also known as the micro canonical ensemble, is generated. When this ensemble is created, energy is conserved.

Particle number (N), volume (V), and total energy (E) are external parameters, and the observables to be determined are temperature (T), pressure (P). In this work, this ensemble has been used along with a thermostat to reach a target temperature.

- **NVT ensemble** – Controlling the temperature through direct temperature scaling during the initialization step yields the constant-temperature, constant-volume ensemble (NVT), also known as the canonical ensemble. During the data gathering phase, temperature-bath coupling was also used. It necessitates the use of a thermostat, which is an algorithm that adds and subtracts energy to maintain a steady temperature. Throughout the run, the loudness is maintained at a steady level. Particle number (N), volume (V), and temperature (T) are external factors, and the observables to be determined are total energy (E), pressure (P). The equipartition theorem is used to rescale the velocity. In this study, this ensemble has been used to equilibrate the confined system with constant volume to a certain temperature for a fixed period of time.
- **NPT ensemble** – Controlling both temperature and pressure is possible with the constant-temperature, constant-pressure ensemble. The pressure is controlled by modifying the volume, and the unit cell vectors are permitted to change. When accurate pressure, volume, and densities are required in the simulation, this is the ensemble to use. This ensemble can also be used to attain the desired temperature and pressure during equilibration before switching to the constant-volume or constant-energy ensemble when data collection begins. In addition to the thermostat, a Barostat is required, which is an algorithm that alters volume to maintain a constant pressure. Particle number (N), pressure (P), and temperature (T) are external factors, and the observables to be determined are Total energy (E), Volume (V).
- **μ VT ensemble** – In statistical mechanics, a grand canonical ensemble is the statistical ensemble that is used to represent the possible states of a mechanical system of particles that are in thermodynamic equilibrium (thermal and chemical) with a reservoir. The system is said to be open in the sense that the system can exchange energy and particles with a reservoir, so that various possible states of the system can differ in both their total energy and total number of particles. The system's volume, shape, and other external coordinates are kept the same in all possible states of the system. The thermodynamic variables of the grand canonical ensemble are chemical potential (μ) and absolute temperature (T). The

ensemble is also dependent on mechanical variables such as volume (V) which influence the nature of the system's internal states. This ensemble is therefore sometimes called the μVT ensemble, as each of these three quantities are constants of the ensemble.

- **NPH ensemble** – NPH is a constant atom, pressure, and enthalpy ensemble.
- **μPT ensemble** - a statistical ensemble where neither the energy nor particle number is fixed. This is a grand canonical ensemble which has constant chemical potential, pressure, and temperature.

3.1.8.1 Ensemble average

Ensemble (Thermodynamic) average is an average over all the points in the phase space at a single or definite time. For a given N and V , an element of an ensemble corresponds to a point in classical phase space, Γ . Phase space refers to the (highly dimensional) space of all positions and momenta of (all atoms of) all molecules:

$$\Gamma = (r^N, p^N) \quad (3.28)$$

Let us consider an observable A (Γ) defined for each point in phase space, for example, the total intermolecular energy. For a discrete set of microstates, the ensemble average of A is,

$$\langle A \rangle = \sum A_i \pi_i \quad (3.29)$$

Here, π is the probability distribution for a certain statistical ensemble. And, ensemble (thermodynamic) average of observable A (r^N, p^N) is given below:

$$\langle A \rangle_{ens} = \iint dp^N dr^N A(r^N p^N) \pi(r^N p^N) \quad (3.30)$$

3.1.8.2 Time Average

If the average of a quantity is taken at a single point of phase space over all the times then it is known as the time or dynamic average. Let $\langle A \rangle$ denotes a time average over the trajectory

generated by MD, where A is a dynamical variable, $A(t)$, and τ represents the simulation time, then it can be written as,

$$\langle A \rangle_{time} = \lim_{\tau \rightarrow \infty} \frac{1}{\tau} \int_{t=0}^{\tau} A(r^N(t), p^N(t)) dt \quad (3.31)$$

3.1.8.3 Ergodic Hypothesis

The duration spent by a system in some part of the phase space of microstates with the same energy is proportional to the volume of this region, according to the ergodic hypothesis, over long periods of time. The ergodic hypothesis states that the thermodynamic or ensemble average is equal to the temporal or dynamic average,

$$\langle A \rangle_{time} = \langle A \rangle_{ens} \quad (3.32)$$

In MD simulation, thermodynamic averaging can be calculated via time averaging which is expressed in the following equation,

$$\langle A \rangle \approx \frac{1}{N} \sum_{i=1}^N A(t_i) \quad (3.33)$$

3.2 LAMMPS – Large-scale Atomic/Molecular Massively Parallel Simulator

LAMMPS is an open source, classical molecular dynamics code developed by Sandia National Laboratories, USA. It is a code that models an ensemble of particles in a liquid, solid, or gaseous state. It can model atomic, polymeric, biological, metallic, granular, and coarse-grained systems using a variety of force fields and boundary conditions. LAMMPS can model systems with only a few particles up to millions or billions. The current version of LAMMPS is written in C++.

Although LAMMPS runs efficiently on single processor workstations, it is designed for parallel applications. The maximum number of atoms that can be modelled in a simulation is dependent on computational power. In most atomic systems, the time required for computing scales linearly with the number of atoms in the system. The same linear scaling does not hold for the number of

processors and limitations occur when any code runs in parallel on a multiprocessor machine. The overhead associated with communicating between processors becomes important and, given enough processors, will eventually dominate the computational time. A maximum of only four processors was used at any time in this work, meaning that most of the runtime is spent on molecular dynamics rather than processor communication.

In the most general sense, LAMMPS integrates Newton's equations of motion for collections of atoms, molecules, or macroscopic particles that interact via short- or long-range forces with a variety of initial and/or boundary conditions. For computational efficiency LAMMPS uses neighbour lists to keep track of nearby particles. The lists are optimized for systems with particles that are repulsive at short distances, so that the local density of particles never becomes too large. On parallel machines, LAMMPS uses spatial-decomposition techniques to partition the simulation domain into small 3D sub-domains, one of which is assigned to each processor. Processors communicate and store "ghost" atom information for atoms that border their sub-domain. LAMMPS is most efficient (in a parallel sense) for systems whose particles fill a 3D rectangular box with roughly uniform density. Plimpton provides an explanation of the specific time integration method used by LAMMPS [119].

3.2.1 LAMMPS operation

As an input, LAMMPS requires a list of initial atomic coordinates and molecular topology information such as mass and force field coefficients for each atom. This information can be either entered at the LAMMPS input script or generated by a custom code which is called when LAMMPS reads the input script. In either method, a simulation box is defined and filled with atoms whose positions and properties are determined by the user. Thermodynamic properties are controlled by defining an ensemble and/or holding some properties constant. Microscopic mechanical characteristics such as velocity and momentum can be explicitly assigned to individual or groups of atoms.

Since the number or position of atoms within the LAMMPS simulation box is not restricted in any way, an ensemble of atoms may be produced in any phase. Care must be taken to assure that the fluid's properties yield the desired location on the phase diagram.

Once the system constraints are set, LAMMPS updates the system by the time integration scheme over a predetermined number of time steps. Integration is prematurely stopped if values stored in the program, such as a thermodynamic property, become unphysical large.

3.2.2 LAMMPS pre- and post-processing

Several features are available within LAMMPS that automatically generate lattices and simple geometric shapes. A built-in preprocessor can produce sets of atom coordinates that correspond to different three-dimensional shapes. The LAMMPS preprocessor takes user input for the specific shape and assigns the required atomic coordinates to a text file. More complex geometries can be created by bypassing the default preprocessor and inputting atomic coordinates via a text file. However, any geometric figure must always be built from a collection of individual atoms which are positioned by the user.

The atoms must be positioned very carefully to create the desired simulation domain as any two atoms placed unnaturally close together can produce a near infinite repulsive force, which leads to a large temperature on the following time step. The unexpectedly large force originates from the steep slope of the LJ potential near $r=0$ and is completely avoidable by a proper choice of atomic spacing. Despite its simplicity, this is a common problem. Each atomic position is defined by an algorithm that writes Cartesian coordinates to a text file, thereby assuming atoms to exist only as points. The algorithm is chosen to space these points properly but exceptions can occur near boundaries of two geometric regions or on the border of the simulation box when periodic boundary conditions are applied. Most commonly, an atom located on one plane of the simulation box is accidentally imposed over another atom on the opposite side by periodic boundary conditions. The proximity of the two atoms produces a large temperature that crashes the program. Locating the offending atom(s) is not always trivial and the details of the input script can become important in resolving these conflicts.

No post-processing operations are available with LAMMPS. Post-processing duties are handled by a multi-functional code created by the author. This code allows the user to find the instantaneous properties like temperature, pressure, density etc. over a range of time steps. These quantities and related data are printed to a text file so that further analysis can be performed with a spreadsheet program.

3.3 OVITO – Open Visualization Tool

A visual output is vitally important in molecular dynamics. Although several good visualization codes exist, Open Visualization Tool (OVITO) is used throughout this work. OVITO is a scientific visualization and analysis software for atomistic and particle simulation data. It helps scientists gain better insights into materials phenomena and physical processes. OVITO is a platform-independent software written in C++ that runs on all major operating systems, including Microsoft Windows, MacOS and Linux. Molecular dynamics (MD), molecular statics and Monte-Carlo based simulations are nowadays standard methods for modelling materials with atomic-scale resolution. Such atomistic simulation models generate three-dimensional atomic configurations or trajectories, which usually need to be further analysed in order to generate new scientific insights. Powerful analysis and visualization techniques play a key role in this process as simulated systems become larger and more complex. Without the right software tools, key information would remain undiscovered, inaccessible and unused. The task of visualization packages such as OVITO is to translate the raw atomic coordinates into a meaningful graphical representation and enable an interpretation by the scientist [120].

OVITO provides a way of animating the collection of data which LAMMPS provides as the coordinates for all the atoms of the simulation over a series of time steps in the form of a properly-formatted text file. Because the atoms are represented by only a set of coordinates, a common approach to visualizing an atom is to assign a radius from the coordinate and fill the volume inside this radius with a solid colour. OVITO has a large variety of colour schemes and visualization styles that helps the user to render and analyse the atomistic characteristics in the excellent graphical interface.

SIMULATION MODEL AND PERFORMANCE PARAMETERS

4.1 Simulation methodology of the present study

A three-phase simulation domain is considered in the present study. The simulation domain consists of a cuboid simulation box of $16 \text{ nm} \times 100.34 \text{ nm} \times 8 \text{ nm}$, as shown in figure 4.1. Two Platinum (Pt) surfaces of dimension $16 \text{ nm} \times 1.37 \text{ nm} \times 8 \text{ nm}$ are modelled at the top and bottom parts of the simulation box. The liquid argon (Ar) layer of 4 nm thickness was placed above the bottom Platinum surface. The rest of the simulation box is filled with saturated vapor argon atoms.

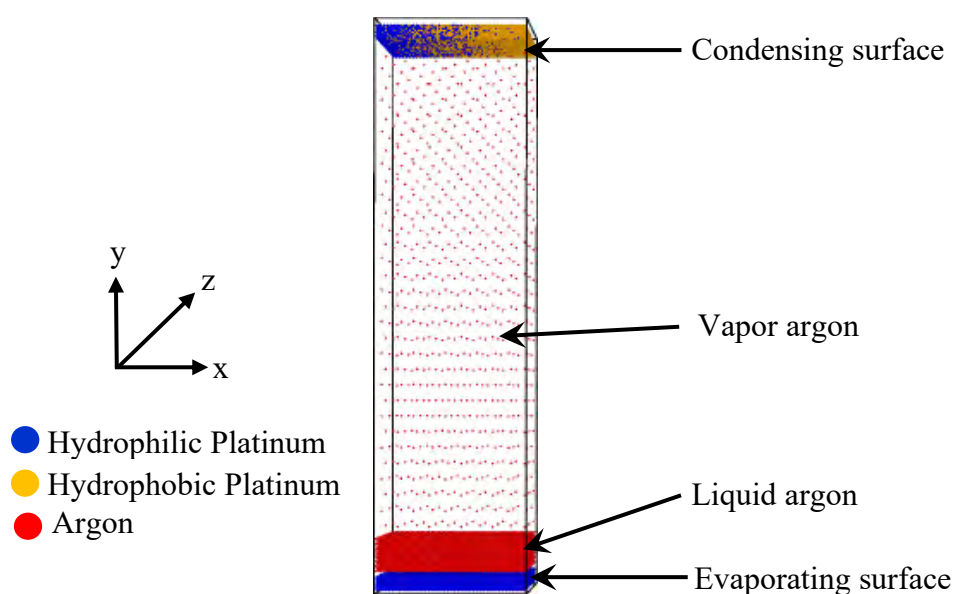


Figure 4.1: Simulation domain at the beginning of the simulation.

The bottom platinum surface consists of eight monolayers of solid Pt atoms. Among them, the bottommost layer is frozen by setting all composite forces and velocity to zero for ensuring the structural stability and zero loss of solid atoms from the simulation box. The atoms of the next two layers are considered as phantom atoms that acted as a heat source where the Langevin thermostat is applied, and through the rest of the five layers, heat transfer occurs between Pt and Ar atoms in the conduction mode. Similar conditions were also adopted for the top Pt surface also. At the beginning of the simulation, the simulation box consisted of 13284 Pt atoms at each solid substrate,

10395 liquid Ar atoms and 1336 vapor Ar atoms. All the atoms modelled had an FCC (1 0 0) crystal structure according to their respective densities (21450 kg/m³ for platinum (Pt), 1378 kg/m³ for liquid argon (Ar) and 6.751 kg/m³ for argon (Ar) vapor) corresponding to the initial equilibration temperature of 90 K. The well-known L-J potential is used for calculating the inter-molecular forces, which are widely used for non-polar molecular systems [121]:

$$\phi(r_{ij}) = 4\varepsilon \left\{ \left(\frac{\sigma}{r_{ij}} \right)^{12} - \left(\frac{\sigma}{r_{ij}} \right)^6 \right\} \quad \text{for, } r_{ij} < r_{cut} \quad (4.1)$$

$$\phi(r_{ij}) = 0 \quad \text{for, } r_{ij} > r_{cut}$$

Here, σ and ε denote the length parameter and energy parameter, respectively. In the present study, for the Pt-Ar system, the values of length and energy parameter used are $\sigma_{Ar-Ar} = 0.3405$ nm, $\sigma_{Pt-Pt} = 0.2475$ nm, $\sigma_{Ar-Pt} = 0.294$ nm, $\varepsilon_{Ar-Ar} = 0.0104$ eV and $\varepsilon_{Pt-Pt} = 0.5211$ eV. The Lorentz-Berthelot mixing rule [122] is used to determine the Ar-Pt length parameter as follows:

$$\sigma_{Ar-Pt} = \frac{\sigma_{Ar-Ar} + \sigma_{Pt-Pt}}{2} \quad (4.2)$$

Using equation 3.35 the Ar-Pt length parameter, σ_{Ar-Pt} has resulted in a value of 0.294 nm. Based on the wettability of the surface the Ar-Pt energy parameter is changed accordingly. Hens et al. [121] showed in their study that when solid-liquid interaction potential is changed, the contact angle of argon placed over flat solid platinum surface also changes accordingly. The change of the contact angle denotes that when $\varepsilon_{liquid-liquid} < \varepsilon_{liquid-solid}$, the surface can be considered as hydrophilic and when $\varepsilon_{liquid-liquid} > \varepsilon_{liquid-solid}$, the surface can be considered as hydrophobic. In their study, they have used $\frac{\varepsilon_{liquid-solid}}{\varepsilon_{liquid-liquid}} = 2$ for hydrophilic surface and $\frac{\varepsilon_{liquid-solid}}{\varepsilon_{liquid-liquid}} = 0.5$ for hydrophobic surface.

In this study, the wetting condition of the bottom surface is kept hydrophilic so that the system ensures an equal number of evaporated atoms for all cases under consideration while, the wettability of the top condensing surface is changed to investigate the effect of wettability on condensation heat transfer. To meet this objective, four different values $\varepsilon_r = \frac{\varepsilon_{Ar-Pt}}{\varepsilon_{Ar-Ar}}$ is used to change the wettability of the condensing surface as follows:

For superhydrophilic surface, $\varepsilon_r = \frac{\varepsilon_{Ar-Pt}}{\varepsilon_{Ar-Ar}} = 4$,

For hydrophilic surface, $\varepsilon_r = \frac{\varepsilon_{Ar-Pt}}{\varepsilon_{Ar-Ar}} = 2$,

For hydrophobic surface, $\varepsilon_r = \frac{\varepsilon_{Ar-Pt}}{\varepsilon_{Ar-Ar}} = 0.5$ and,

For superhydrophobic surface, $\varepsilon_r = \frac{\varepsilon_{Ar-Pt}}{\varepsilon_{Ar-Ar}} = 0.25$

The change of contact angle with the change of ε_r is shown in figure 4.2.

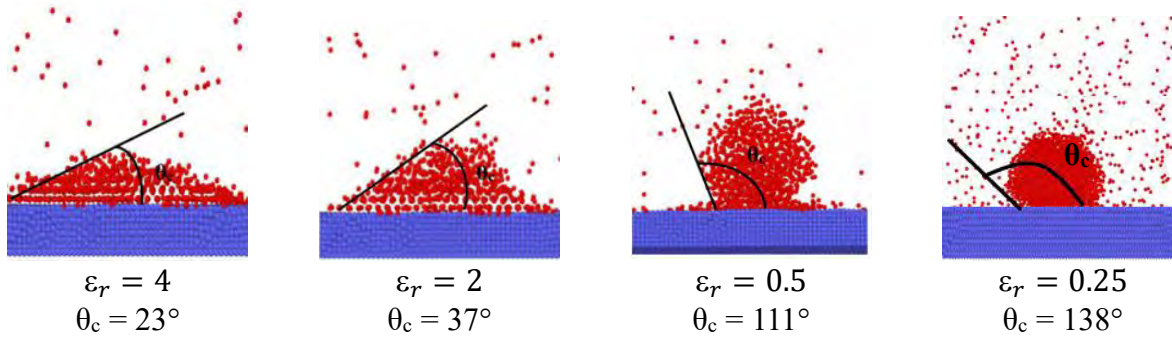


Figure 4.2: Liquid-solid wetting scenario at the equilibrium state for different solid-liquid interaction strengths.

In this work, two different types of hybrid wetting surface are modelled, namely, patterned hybrid wetting surface and functional wettability gradient (FWG) surface.



Figure 4.3: Atomistic configuration of the (a) patterned (b) FWG hybrid wetting surface with fraction of hydrophilic atoms, $\alpha = 0.6$.

The patterned hybrid wetting surfaces have been modelled by juxtaposing different wetting region together on the solid substrate as shown in figure 4.3 (a). The variation of the solid-liquid energy parameter for different hydrophobic fraction, β is depicted in figure 4.4 (a). On the other hand, FWG surfaces are modelled by using the novel concept of functionally graded materials (FGM). To properly model an FWG surface for MD simulation, the value of ε_{Ar-Pt} (energy parameter between Ar and Pt) is required to be varied according to a particular function along any direction. The modelling of the FWG substrate consists of the following three steps:

- (i) At first a solid substrate of the prescribed dimension has been created with hydrophilic Pt atoms.
- (ii) Then, the hydrophilic substrate is subdivided into a number of cuboid chunks of 0.196 nm × 0.196 nm × 8 nm.
- (iii) And, finally, in each chunk, the hydrophilic atoms are randomly replaced by hydrophobic atoms, according to the following power-law function:

$$f(x) = (x/L)^p \quad (4.3)$$

Where, $f(x)$ is the weight fraction of hydrophobic atoms in the hydrophilic chunk, x is the position of chunk's centroid along the x -direction, L is the length of the substrate along the x -direction, and p is a function parameter. Thus, a FWG surface can be modelled as shown in figure 4.3 (b).

The numerical value of ϵ_{Ar-Pt} will change along x -axis (as shown in figure 4.4 (b)) following the equation:

$$\epsilon_{Ar-Pt}(x) = (x/L)^p \times \epsilon_{Ar-Pt,hydrophilic} + [1 - (x/L)^p] \times \epsilon_{Ar-Pt,hydrophobic} \quad (4.4)$$

The fraction of hydrophobic atoms, β for different FWG surfaces is calculated using the following expression:

$$\beta = \int_0^L (x/L)^p dx/L \quad (4.5)$$

Thus, by changing the value of function parameter p , FWG surfaces with different weight fractions of hydrophilic-hydrophobic atoms can be obtained as shown in figure 4.3 (b).

The Velocity-Verlet algorithm (discussed in section 3.1.5) with a timestep of 5 fs is used to solve Newton's equation of motion for determining the position and velocity of atoms. The simulation process of the present MD framework can be divided into 2 different phases:

- i) **Equilibrium molecular dynamics (EMD):** In the beginning period, NVT ensemble is applied for 0.5 ns on the whole system by turning on the Langevin thermostat to fix the temperature of the entire system at 90 K. Then the Langevin thermostat is turned off

and the system is allowed to equilibrate under NVE ensemble for the next 2 ns. Thus, a total simulation period of 2.5 ns, is considered as equilibration period to ensure the thermal equilibrium of the present study in all cases.

- ii) **Non-equilibrium molecular dynamics (NEMD):** After the end of the equilibration period, the temperature of the bottom Pt surface is raised to 130 K, and the temperature of the top surface is kept at 90 K. Thus, the non-equilibrium MD simulation was carried out for the next 6.6 ns.

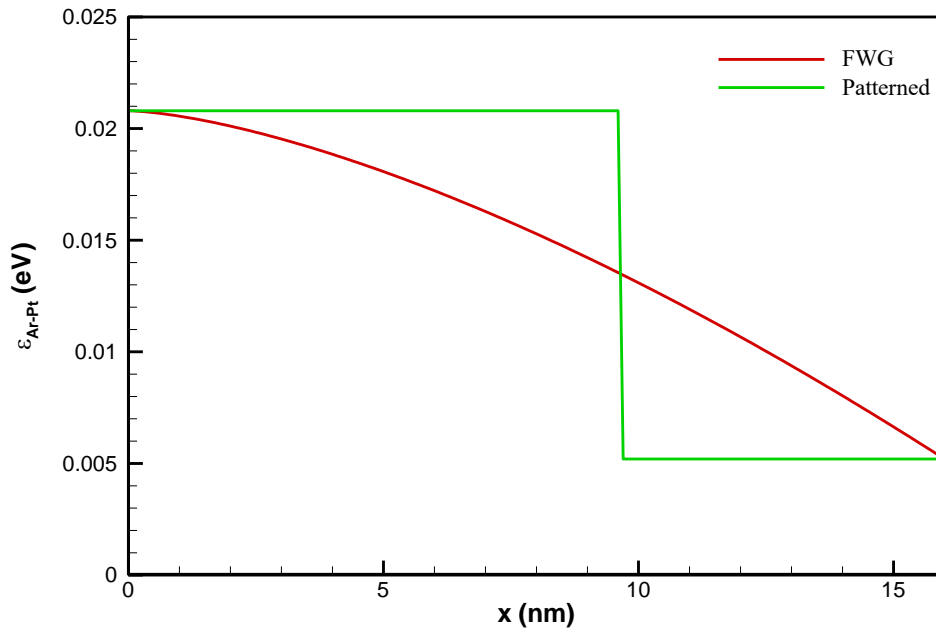


Figure 4.4: Wettability gradient profile, namely, the spatial variation of the Ar-Pt energy parameter, $\epsilon_{\text{Ar-Pt}}$ for FWG and patterned surface with hydrophobic weight fraction, $\beta = 0.4$

After ensuring the necessary equilibration condition till 2.5 ns, in the non-equilibrium period, the liquid atoms started getting evaporated. Then, the vapor atoms reached the top surface and started to get condensed. In this way, the bottom surface acted as a source of vapor atoms to support the condensation phenomenon at the top surface. A similar configuration was modelled in previous MD studies for studying condensation phenomenon [81,95]. Based on the wetting condition of the top condensing surface, different surface configurations are considered in this study.

4.2 Evaluation of transport characteristics

In this study, several transport characteristics such as temperature, total energy, spatial number density, heat flux, surface tension are evaluated to investigate the condensation phenomena over different types of hybrid wetting surfaces. The calculation and formula used to determine these transport characteristics are briefly discussed in this section.

4.2.1 Temperature

The relationship between the atomic velocity and temperature, T has been demonstrated in equation 3.39, where, m_j and v_j are the mass and velocity of the atom j respectively and K_b is the Boltzmann constant.

$$\frac{1}{N} \sum_{j=1}^N \frac{1}{2} m_j v_j^2 = \frac{3}{2} K_b T \quad (4.6)$$

By implementing equation 4.6, the temperature of a group of atoms is calculated in this study.

4.2.2 Total energy

The total energy E of the simulation domain can be obtained by adding up the kinetic, E_{kin} and potential, E_{pot} energies. The kinetic energy can be computed from the individual momentum of the atoms, while the potential energy is the sum of interatomic interactions. The equations used to determine the kinetic energy and potential energy are shown in equation (4.7) and (4.8),

$$E_{kin} = \frac{1}{2} \sum_i^N m v_i^2 \quad (4.7)$$

$$E_{pot} = \sum_i \sum_{i \neq j} \phi(r_{ij}) \quad (4.8)$$

4.2.3 Spatial density

In the present study, the spatial density profile of argon for different conditions has been observed and this is an important parameter particularly in phase change phenomena. To compute the spatial density, the simulation domain has been divided into equal 347 slices or bins in the y-direction with a thickness of 0.2895 nm and the number of atoms in each slice has been counted. Hence, if

the slice thickness is Δy and N_i is the number of atoms in slice i , then the instantaneous spatial number density of that slice can be evaluated with the help of following formula,

$$\rho_N(y_i) = \frac{N_i}{l_x l_z \Delta y} \quad (4.9)$$

The spatial density can be determined from equation (4.10),

$$\rho(y_i) = \frac{m N_i}{l_x l_z \Delta y} \quad (4.10)$$

Here, l_x and l_z represent the x and z dimensions of the simulation domain respectively, and m is the mass of a single atom.

4.2.4 Heat flux

In the present study, heat flux vector, J along the normal direction to the solid surface through the liquid film has been calculated by estimating the per-atom potential energy, the per-atom kinetic energy, and per-atom stress tensor.

$$J = \frac{1}{V} \left(\sum_i e_i v_i - \sum_i S_i v_i \right) \quad (4.11)$$

Where, V is the volume, e_i is the per-atom energy (potential and kinetic), S_i is the per-atom stress tensor and v is a 3×3 matrix vector.

4.2.5 Surface tension

To evaluate the spatial distribution of surface tension, the entire simulation system is split into 5933 planar segments of dimension $1 \text{ nm} \times 0.29 \text{ nm}$ along the direction normal to the surface. Then Kirkwood's mechanical approach [123] is adopted for determining the surface tension, γ at each planar segment using the following expression [100]:

$$\gamma = \int_{-\infty}^{+\infty} [P_N(y) - P_T(y)] dy \quad (4.12)$$

Here, $P_N(y)$ and $P_T(y)$ represents normal and tangential pressure components, respectively which are calculated using the following expressions [100]:

$$P_N(y) = n(y)k_B T - \frac{1}{2A} \left\langle \sum_{i \neq j} \frac{y_{ij} \varphi(r_{ij})}{r_{ij}} \theta \left(\frac{y - y_i}{y_{ij}} \right) \theta \left(\frac{y_j - y}{y_{ij}} \right) \right\rangle \quad (4.13)$$

$$P_T(y) = n(y)k_B T - \frac{1}{2A} \left\langle \sum_{i \neq j} \frac{[z_{ij} + x_{ij}] \varphi(r_{ij})}{r_{ij} y_{ij}} \theta \left(\frac{y - y_i}{y_{ij}} \right) \theta \left(\frac{y_j - y}{y_{ij}} \right) \right\rangle \quad (4.14)$$

Here, $n(y)$ represents number density of fluid atoms along y-axis and k_B denotes Boltzman's constant.

4.2.6 Time-averaged condensation mass flux

To estimate the overall condensation mass flux during the entire simulation period, time-averaged condensation mass flux, $m_{c,avg}$ is calculated using the following expression,

$$m_{c,avg} = \frac{\int_0^t m_c dt}{\int_0^t dt} \quad (4.15)$$

Here, t and m_c denote the time and instantaneous condensation mass flux respectively.

4.2.7 Time-averaged condensing wall heat flux

To estimate the overall condensing wall heat flux during the entire simulation period, time-averaged condensing wall heat flux, $q_{w,avg}$ is calculated using the following expression,

$$q_{w,avg} = \frac{\int_0^t q_w dt}{\int_0^t dt} \quad (4.16)$$

Here, t and q_w denote the time and instantaneous condensing wall flux respectively.

4.2.8 Thermodynamic heat flux

In this study, thermodynamic heat flux, q_{therm} is calculated using the following expression,

$$q_{therm} = m_{c,avg} \times h_{fg} \quad (4.17)$$

Here, h_{fg} denotes the latent heat of vaporization of argon atoms calculated at average temperature.

RESULTS AND DISCUSSIONS

In this work, MD simulations have been conducted to investigate the following aspects of condensation over hybrid wetting surfaces:

- i) Effect of hydrophilic-hydrophobic proportion and patterning on condensation over patterned hybrid wetting surface
- ii) Effect of gradient and patterned wetting configuration on condensation over hybrid wetting surface at different hydrophilic-hydrophobic combination and the comparative analysis
- iii) Effect of wettability contrast on condensation over hybrid wetting surfaces with gradient and patterned wetting configuration

This chapter is subdivided into four sections. Section 5.1 will cover the equilibrium characteristics and validation of the present atomistic model and section 5.2, section 5.3 and section 5.4 will cover the aforementioned three aspects of the present study.

5.1 Equilibrium characteristics and model validation

In this work, at the beginning of the simulation 2.5 ns is considered as the period of the thermal equilibrium. Various transport characteristics such as spatial number density, temperature, total energy and wall heat flux have been checked to ensure thermal equilibrium as well as validate the present atomistic model.

5.1.1 Spatial number density

The spatial number density of fluid atoms represents number of argon atoms at different position along a particular direction. In this work, to evaluate the spatial number density the simulation domain is subdivided into 347 one-dimensional bins each having a thickness of 0.2895 nm along y-direction. Then, using equation (4.9), the spatial number density, ρ_N profile for fraction of hydrophilic atoms, $\alpha = 0.2$ surface condition has been evaluated at 1.5 ns and 9 ns as shown in figure 5.1 (a). The spatial number density, ρ_N profile of figure has been compared with the earlier work working with argon as working fluid and similar number density profile was reported by

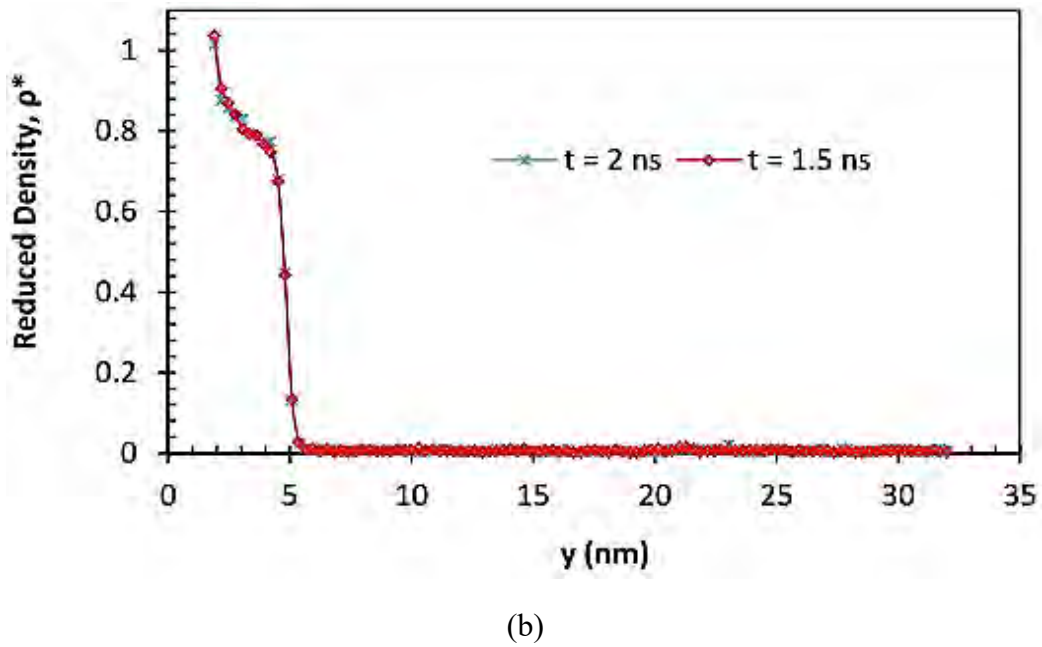
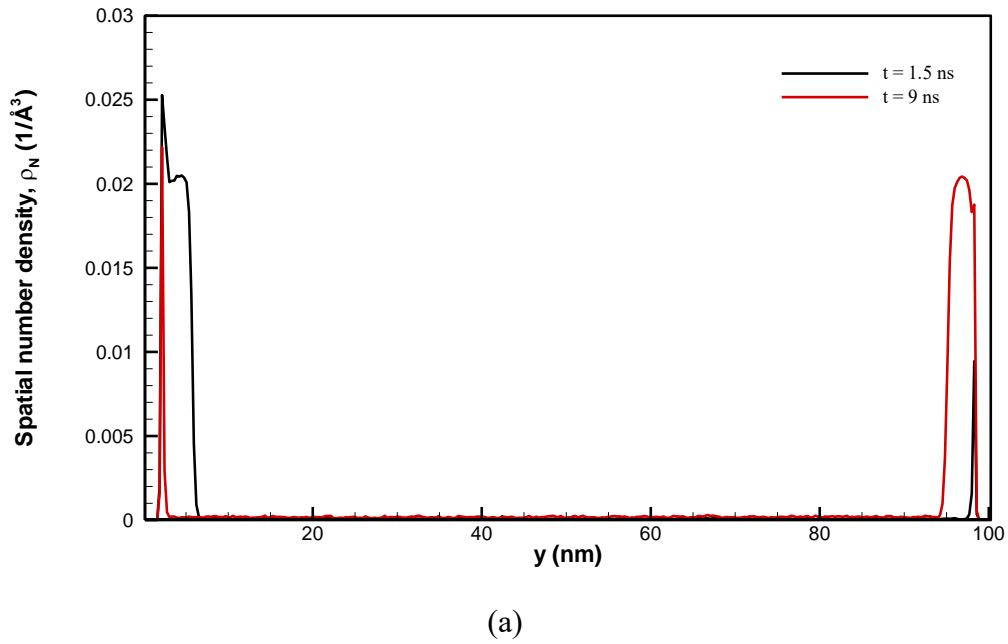
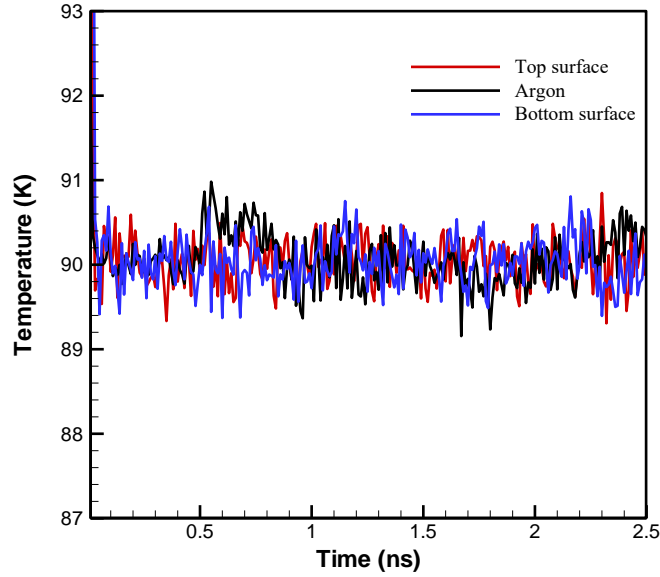


Figure 5.1: (a) Spatial number density, ρ_N profile of Argon along y-direction and (b) Reduced density profile of argon on a flat Pt-surface as depicted in Morshed et al. [124]

Morshed et al. [124] in an atomistic study of similar model near the evaporating surface. Besides, the similarity of ρ_N with Morshed et al. density of working fluid has also been evaluated near the bottom surface using equation (4.10). The calculated density at 1 nm distance from the bottom surface is equal to 1327

Kg/m^3 corresponding to $\rho_N = 0.02 \text{ \AA}^{-3}$ in figure 5.1. The bulk density of liquid argon at 90 K is equal to 1367 Kg/m^3 which is very close to the calculated spatial density. From the aforementioned discussion of spatial number density profile, it can be stated that the atomistic distribution is properly modelled to study the phase change characteristics of argon.

5.1.2 Temperature of system components



(a)

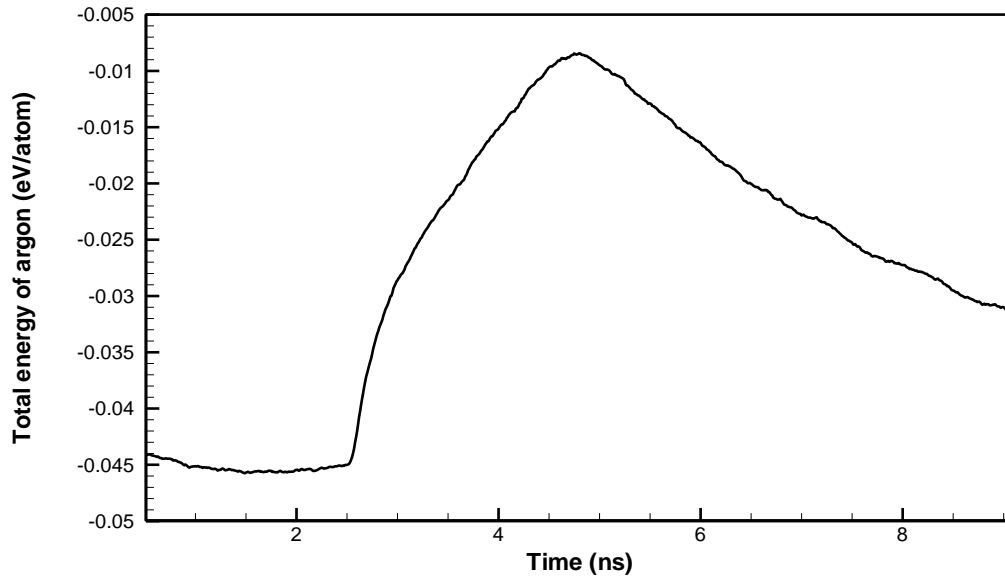
Figure 5.2: Temperature of the system components during equilibration period ($\alpha = 0.2$).

In this study, the entire atomistic system is equilibrated at 90 K. The temperature of each group atoms is calculated using equation (4.6). From figure 5.2 (a) it is observed that the temperature of argon, top and bottom surface fluctuates around 90 K. This is clear indication proper equilibration of the entire system at 90K.

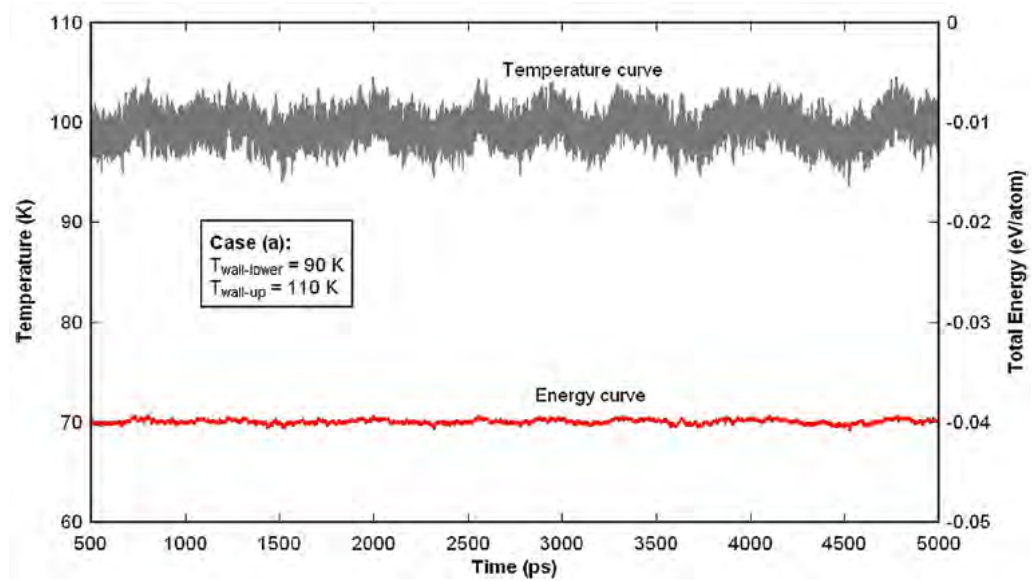
5.1.3 Total energy of argon atoms

The total energy of the argon atom is calculated from the summation of kinetic energy and potential energy as obtained from equation (4.7) and (4.8), respectively. The per atom value of total energy is plotted in figure 5.3. From figure 5.3, it is noticed that the per atom value of total energy of argon atom becomes constant at around -0.045 eV/atom by the end of equilibrium period. This constant value of total energy ensures proper thermal equilibrium of the atomistic system. In

addition, the total energy of the system conforms with the earlier study [125] of similar atomistic configuration in terms of order of magnitude during the equilibration period.



(a)



(b)

Figure 5.3: (a) Temporal variation of total energy of argon atom ($\alpha = 0.2$), and (b) system energy curve during equilibration period in ref. [125].

5.1.4 Wall heat flux during equilibrium period

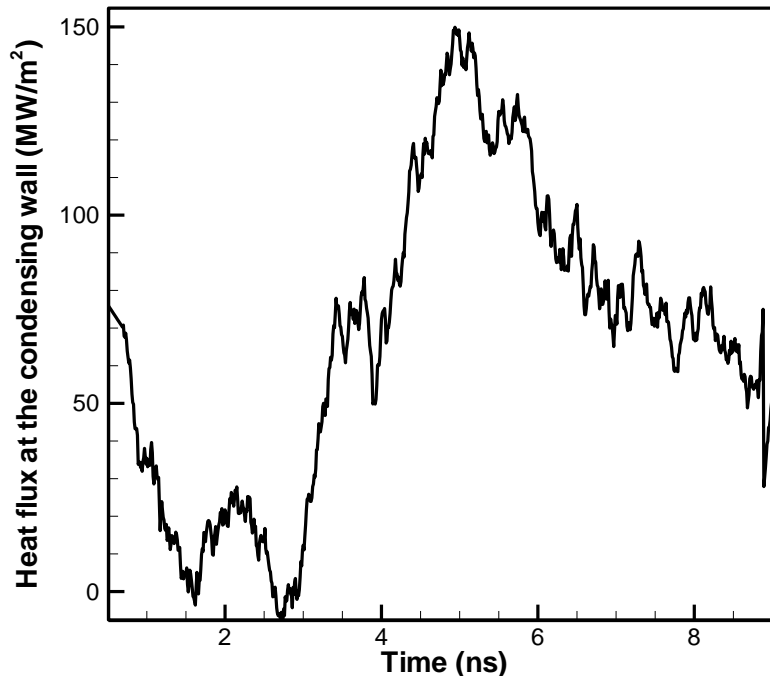
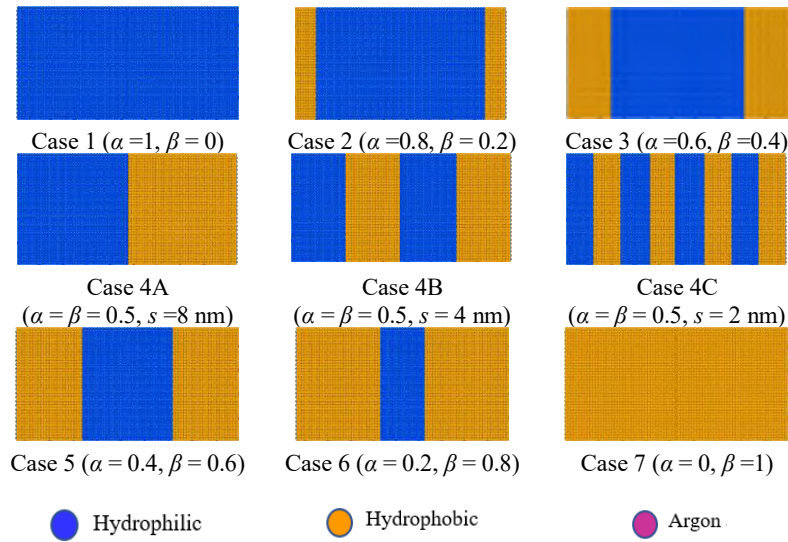


Figure 5.4: Heat flux at the condensing wall ($\alpha = 0.2$).

Figure 5.4 depicts the wall heat flux at the top condensing surface obtained by using equation (4.11). From figure 5.4, it can be reported that wall heat flux at the condensing wall is very close to zero by the end of equilibration period. This indicates that the argon atoms have attained thermal equilibrium with the top condensing surface.

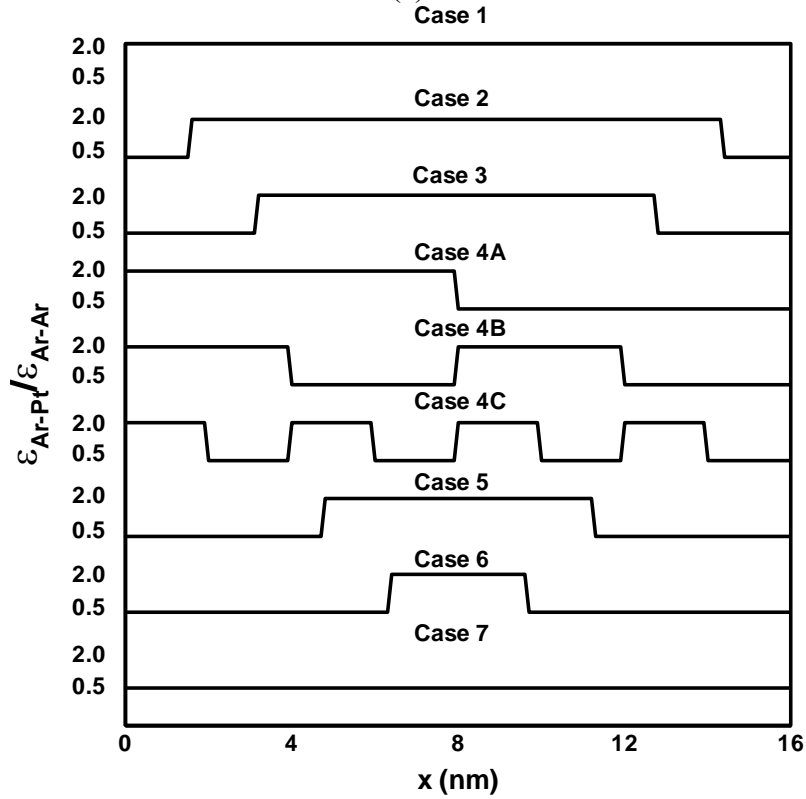
5.2 Effect of philic-phobic content and patterning

In this section, based on the wetting condition of top condensing surface, 9 different surface configurations are considered as shown in figure 5.5. The hydrophilic fraction of the hybrid condensing surface is reduced from case 2 to case 6 with a decrement of 0.2 in our study with a view to study the condensation characteristics of the hybrid wetting surface with change in hydrophilicity of the hybrid wetting surface.



Wetting Configuration of the condensing wall
 Fraction of hydrophilic portion = α ,
 Fraction of hydrophobic portion = β
 Strip size = s

(a)



(b)

Figure 5.5: (a) Wetting configuration of the top surface for different cases (b) Change in interaction energy parameter ratio, $\epsilon_{\text{Ar-Pt}}/\epsilon_{\text{Ar-Ar}}$ for various cases.

Also, for studying variation in hydrophilic-hydrophilic arrangement on the condensation characteristics of the hybrid wetting surface, the strip size of the hydrophilic and hydrophobic portion is changed in case 4A, case 4B and case 4C keeping the hydrophilic and hydrophobic content equal. The performance of hybrid wetting surfaces have been also been homogeneous wetting surfaces i.e., hydrophilic and hydrophobic surfaces of case 1 and case 7 respectively. In all the aforementioned cases, the wetting condition of the bottom surface is kept hydrophilic with $\epsilon_r = 2$ for all cases so that the system ensures equal number of evaporated atoms.

After the equilibration period of 2.5 ns, in NEMD simulation when the bottom surface temperature is raised to 130 K, the evaporation of liquid atoms has taken place at a higher rate which has resulted in condensation of vapor atoms at the top surface whose temperature is set at 90 K. The performance of the condensing surface is reported by evaluating the number of condensed atoms, condensation mass flux, heat flux at condensing wall and local liquid-vapor interfacial surface tension. The growth mode of condensate as obtained in the present study for various cases hybrid wetting conditions of the condensing surface has been correlated with classical growth mode.

5.2.1 System characteristics for different cases

Figure 5.6 depicts the transient variation of total energy content of argon atoms. It is visualized that total energy content of the argon atoms has become constant at the end of equilibration period in all cases. This clearly ensures that the system has become properly equilibrated before the beginning of NEMD simulation. Then in the NEMD simulation, the total energy content of the argon atoms started to increase when the temperature of the bottom platinum surface is raised to 130 K. This rate of increment started to decrease as vapor atoms generated from the bottom side has started to get condensed by dissipating heat on the top platinum surface which is at 90 K. At one point, the rate of condensation became higher than the rate of evaporation which resulted in the decrement of total energy content of argon atoms. From figure 5.6(a), it is observed that the decrement of total energy in figure 5.6(a) started earlier with the increment of hydrophilic fraction of the surface and also the total energy content of argon atoms is lower in case of surfaces with higher hydrophilic content. This indicates that the rate of condensation is faster in case of surfaces with higher hydrophilic content. This phenomenon is further depicted in numerical form in figure 5.12.

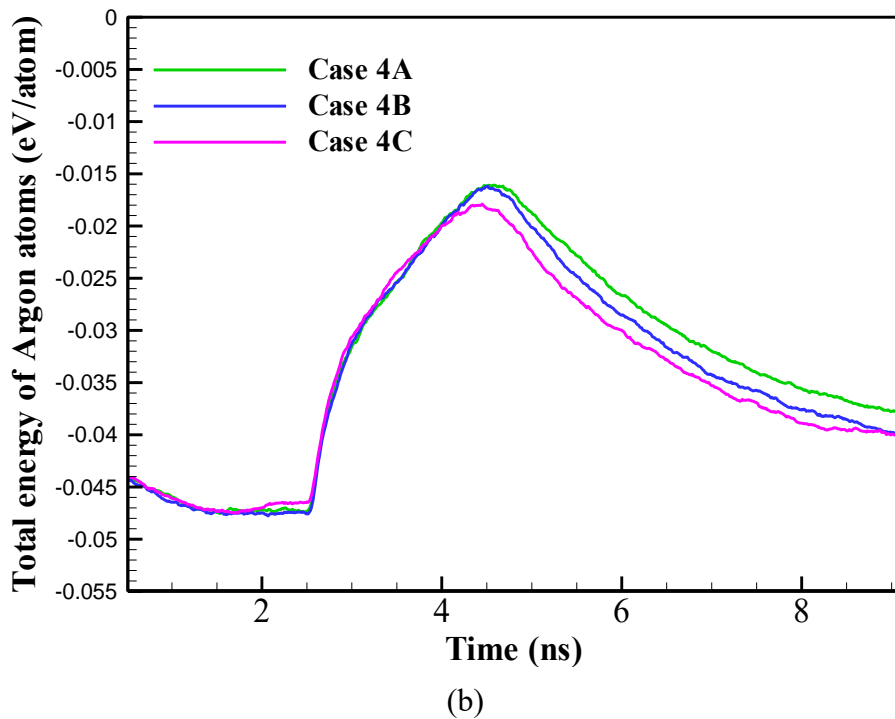
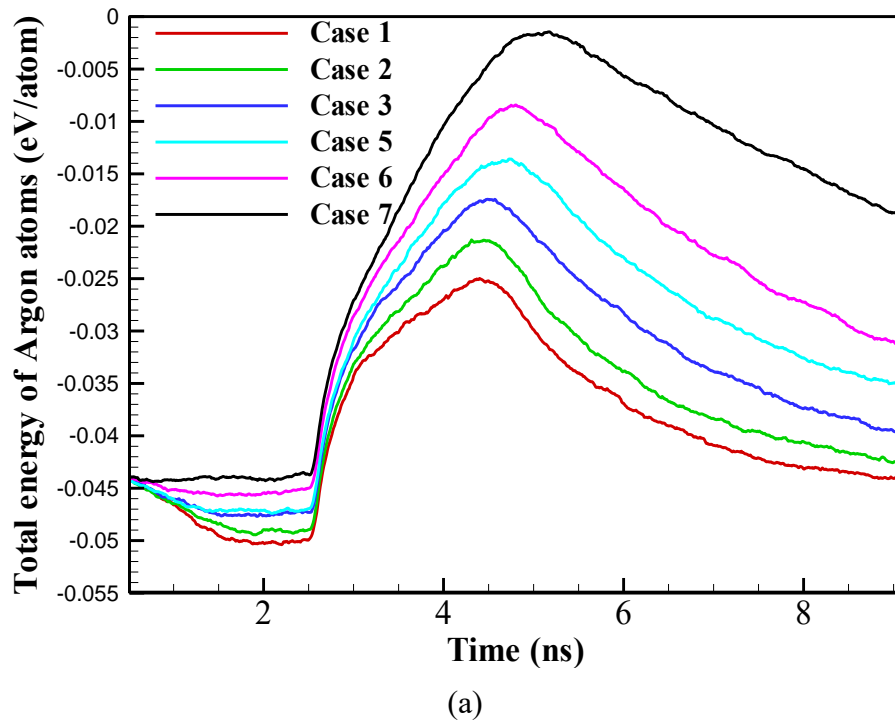


Figure 5.6: Temporal variation of total energy content of Argon atoms (a) at different portion of hydrophilic and hydrophobic region (b) at different strip size having equal portion of hydrophilic and hydrophobic region.

The rate of condensation is also dependent on the arrangement of hydrophilic-hydrophobic patterning. It is depicted that the total energy content of argon atoms is lower in hybrid wetting surfaces with smaller strip size of hydrophilic and hydrophobic pattern which indicates higher rate of condensation heat transfer with smaller strip size.

5.2.2 Solid-liquid interfacial thermal resistance for different hybrid wetting surface

From the previous studies, it is well known that solid-liquid interfacial thermal resistance or Kapitza resistance plays an important role in nanoscale phase change phenomenon [34,35,126]. Lower solid-liquid interfacial thermal resistance offers higher condensation rate of atoms. Solid-liquid interfacial thermal resistance, R_{int} can be calculated from the following formula:

$$R_{int} = \Delta T/q \quad (5.1)$$

Here, ΔT is the temperature difference between solid and liquid atoms at the interface and q is the heat flux transferred from heat source to heat sink across the argon atoms.

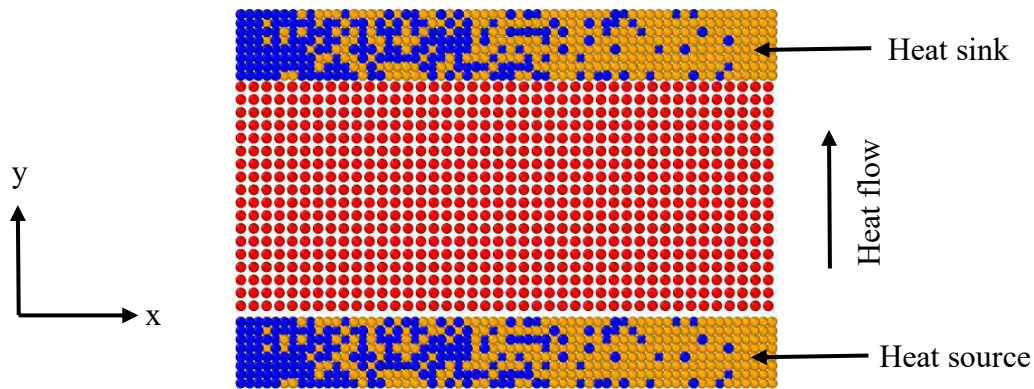


Figure 5.7: Simulation domain with dimensions 10 nm x 8.9 nm x 7 nm along x, y and z-axis at the beginning for calculating solid-liquid interfacial thermal resistance.

For evaluating thermal resistance at the solid-liquid interface in accordance to the method reported in ref. [127], a separate simulation domain (see figure 5.7) with dimension 10 nm x 8.9 nm x 7 nm along x, y and z direction respectively is considered. The simulation domain consists of two solid platinum surface of 1.37 nm thickness and all the liquid Argon atoms were sandwiched between them. The bottom surface acted as heat source whereas the top one acted as heat sink. The wetting characteristics of the source and sink was replicated exactly the same according to the wetting

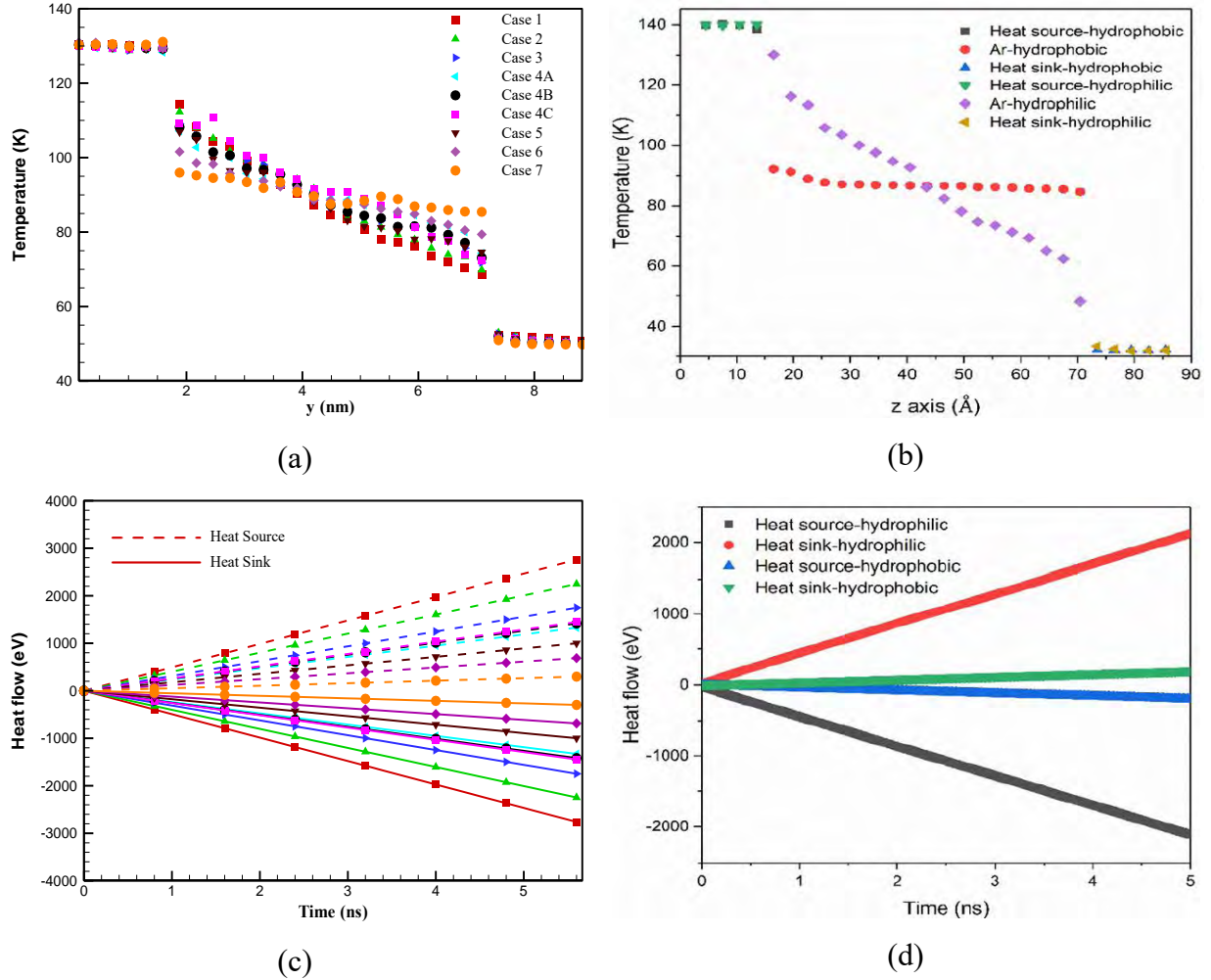
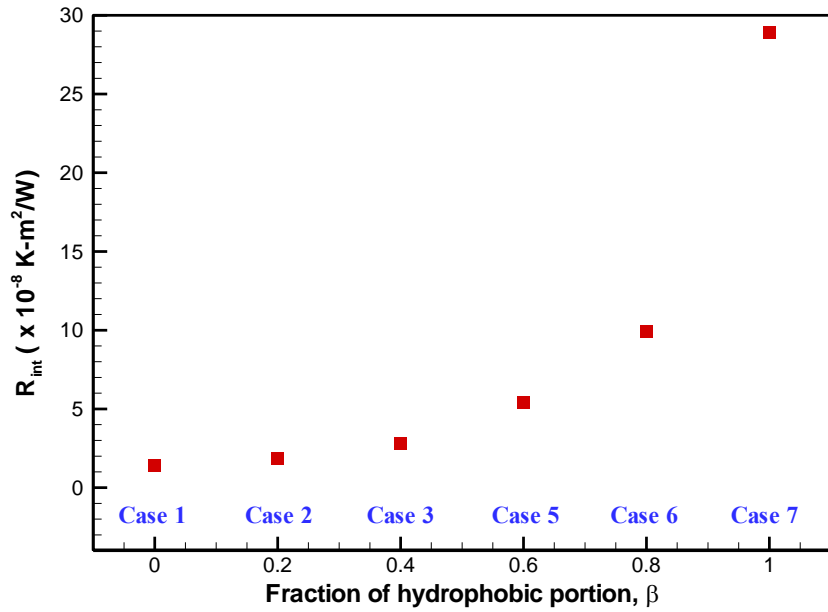


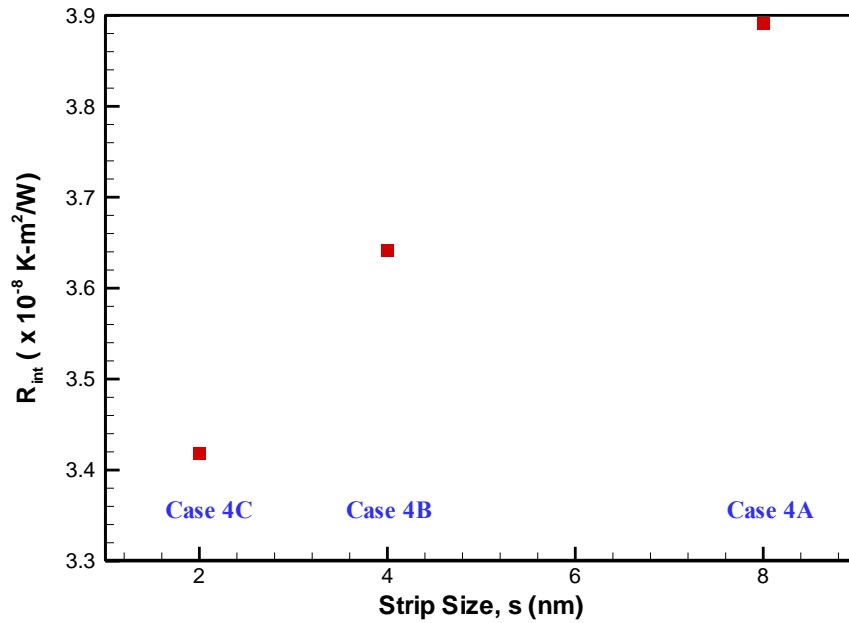
Figure 5.8: (a) Spatial variation of temperature along the direction of heat flow for different cases, (b) Similar variation of temperature along the direction of heat flow in ref. [127], (c) Temporal variation of heat flow through heat source and heat sink for different cases, and (d) Similar variation of heat flow across heat source and heat sink in ref. [127].

characteristics considered in this study for all cases (see figure 5.5). The system is consisted of 7344 liquid argon atoms and 7344 platinum atoms at each solid surface. At first, the temperature of the whole system was kept at 90 K under NVT ensemble. Then the simulation was carried out under NVE ensemble fixing the temperature of the heat source and sink at 130 K and 50 K respectively using Langevin thermostat as done in [127]. The simulation run time was 5.6 ns with a timestep of 5 fs. For estimation of near wall thermal condition, the simulation cell is subdivided into 31 one dimensional bins each of thickness 0.2895 nm along y-axis for obtaining the spatial

temperature distribution profile. The temperature jump across the solid-liquid interface can be identified from the spatial temperature profile plotted in figure 5.8(a). It is depicted that the



(a)



(b)

Figure 5.9: Thermal resistance profile at the solid-liquid interface, R_{int} with the variation in (a) hydrophobic fraction, (b) hydrophilic-hydrophobic patterned strip size of hybrid wetting surface.

interfacial temperature difference between solid and fluid is decreased with the increment of hydrophilic content and decrement of strip size of hybrid wetting surface because higher flow of thermal energy through the fluid atoms. The heat flow from the source to sink across the argon atoms is shown in figure 5.8(c). The results shown in figure 5.8 conforms with the results of ref. [127] both in terms of pattern and order of magnitude. The value of heat flux q was determined from the simulation data of figure 5.8 (c) for all the cases. The solid-liquid interfacial thermal resistance, R_{int} determined from equation (5.1) is plotted in figure 5.9 for all the cases considered in this study which is in same order of magnitude with the previous researches [126–129]. The results from figure 5.9 clearly shows that the solid-liquid interfacial thermal resistance is decreased with the increment of hydrophilic content and decrement of strip size of hydrophilic-hydrophobic pattern of hybrid wetting surface. This will allow the surface with more hydrophilic portion to have a higher adsorption and condensation rate compared to the surface with less hydrophilic portion at the initial period of condensation in agreement with earlier findings [92].

5.2.3 Nucleation and growth mode of condensate for different condensing surface

According to classical nucleation theory, a free energy barrier, G^* is needed to be overcome for the development of stable nucleation with a required number of stable clusters. Thus, the lower value of G^* will be suitable for faster nucleation. This free energy barrier G^* is expressed as [73],

$$G^* = \frac{16 \pi \gamma_{lv}^3}{3 \rho_l^2 \Delta\mu^2} F \quad (5.2)$$

Here, γ_{lv} denotes surface tension at the liquid-vapor interface, ρ_l is density of the fluid at liquid phase, $\Delta\mu$ denotes difference between chemical potential energy of liquid phase and vapor phase and F is the Fletcher factor. In case of nucleation on flat surface, $F = (2 - 3\cos\theta_c + \cos^3\theta_c)/4$ where, θ_c is the contact angle between droplet and the solid surface. So, F increases with the increment of contact angle.

Pu et al. [73] explained in their MD study that surfaces with higher value of solid-liquid energy parameter (wettability) decreases the value of G^* and therefore offers higher nucleation rate compared to the surfaces with lower one. For this reason, in our present study, hydrophilic regions of the hybrid wetting surface offered higher scope of nucleation and in the initial period large

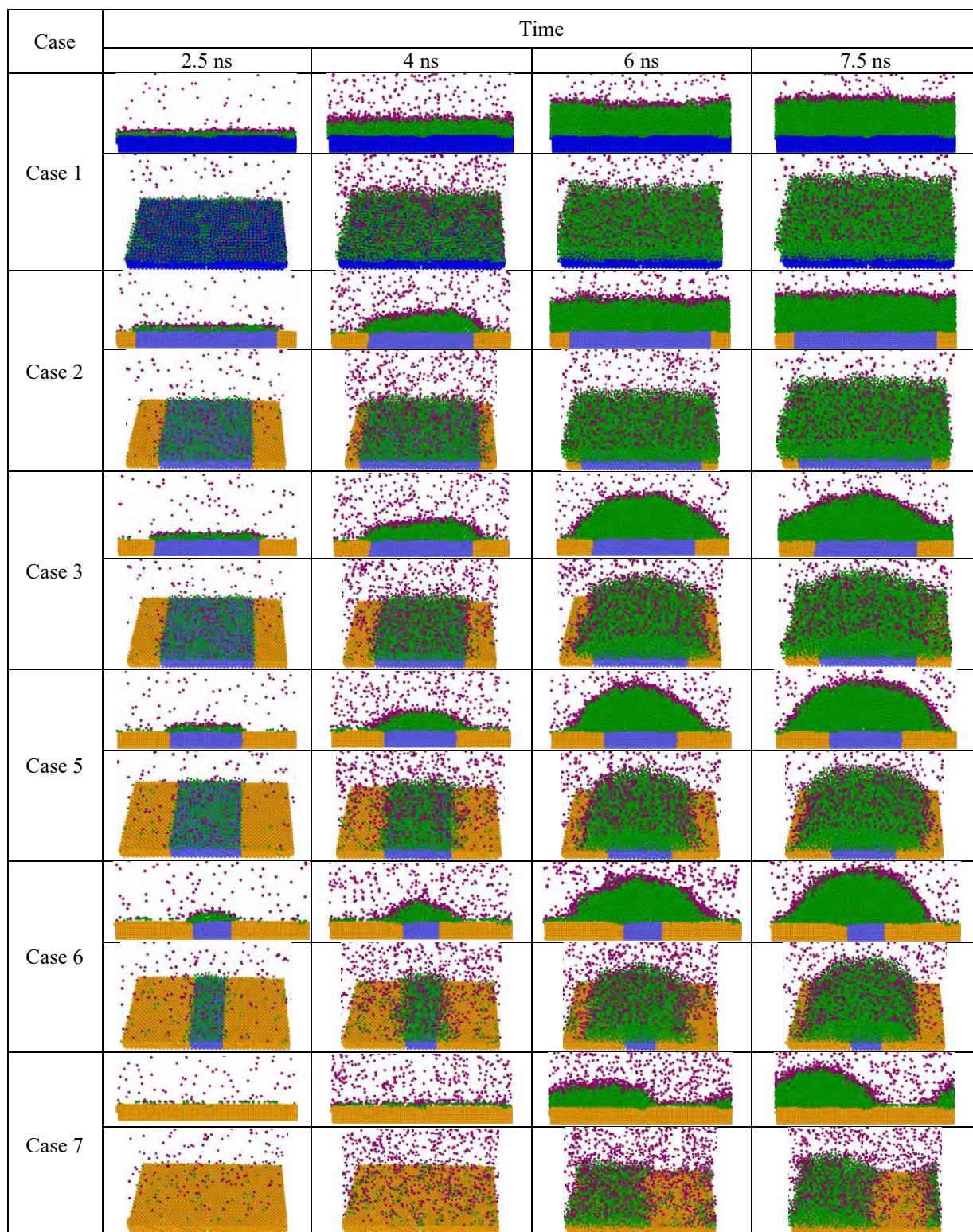


Figure 5.10: Snapshots of atomic trajectory at top surface for showing difference in nucleation and growth of liquid clusters of Argon atoms with change in hydrophilic portion percentage. Colours indicating- blue for hydrophilic region, orange for hydrophobic region, purple for vapor Ar atoms, green for liquid Ar atoms.

amounts of liquid atoms were present on the hydrophilic regions of the hybrid wetting surface in figure 5.10. Thus, the area of nucleating zones increased with the increase of hydrophilic content of the hybrid wetting surface. When the size of hydrophilic-hydrophobic strip is reduced to a small value the fluid atoms find it more attracted to get adsorbed on the hydrophilic region of the solid substrate because of the presence of the hydrophobic region at a closer distance. For this reason, larger number of fluid atoms have been adsorbed in figure 5.12 (b). Thus, with the decrement of strip size of hydrophilic-hydrophobic pattern, the hydrophilic region was split into smaller segments which increased the opportunity of the vapor atoms to nucleate on the hydrophilic region. Therefore, higher number of vapor atoms condensed with the increment of hydrophilic content and decrement of hydrophilic-hydrophobic pattern strip of the hybrid wetting surface. It is also known from the MD study of Wang et al. [85] that the liquid atoms of a droplet spontaneously migrate from hydrophobic region to hydrophilic region. For this reason, in figure 5.10 and 5.11, it is noticed that few atoms which nucleated on the hydrophobic region migrated from hydrophobic region to nearby hydrophilic region.

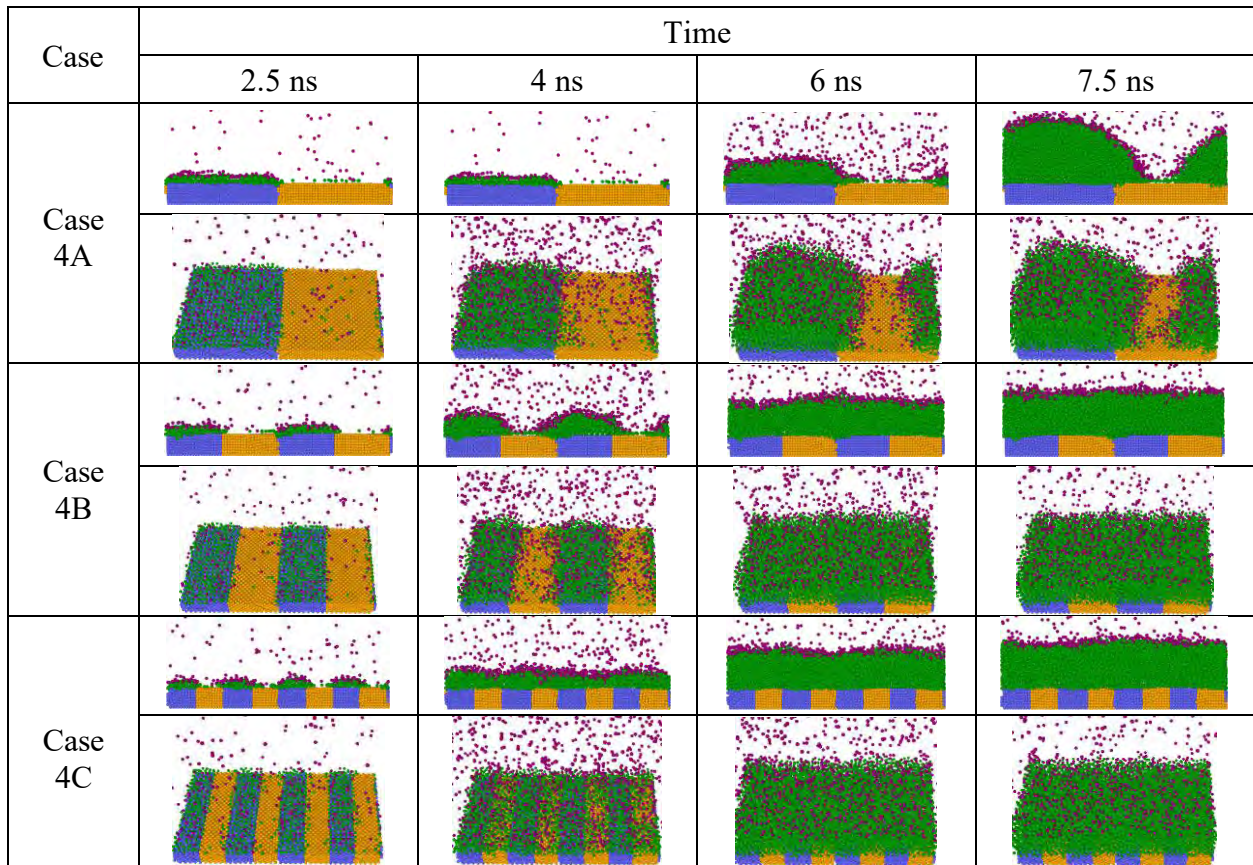


Figure 5.11: Snapshots of atomic trajectory at top surface for showing difference in nucleation

and growth of liquid clusters of Argon atoms with change in strip size of patterned hybrid wetting surface. Colours indicating- blue for hydrophilic region, orange for hydrophobic region, purple for vapor Ar atoms, green for liquid Ar atoms.

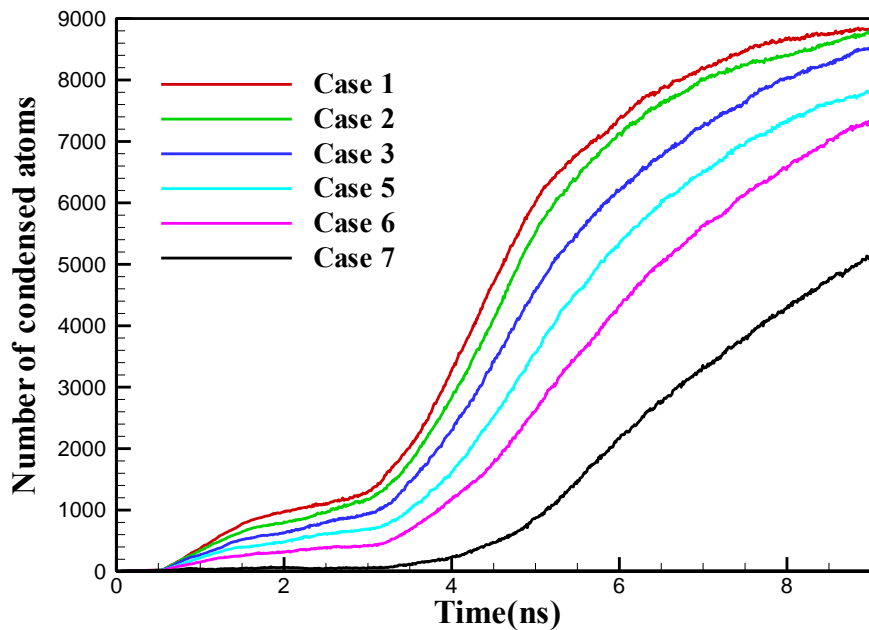
Based on the nucleation and growth of atoms during condensation, the growth mode has been classified into 3 principal types– (i) Frank-van der Merve (FM) mode or layer by layer growth mode (ii) Volmer-Weber (VW) mode or island growth mode and (iii) Stranski-Krastanov (SK), mode or layer plus island growth mode [130]. FM growth mode is visualized when the solid-liquid attraction is higher than the liquid-liquid attraction whereas, VW growth mode is seen when liquid-liquid attraction is higher than the solid-liquid interaction. SK growth mode is an intermediate mode between VW and FM growth mode where 3D growth of island take place after the formation of initial 2D layer. From the snapshots of figure 5.10, it can be shown that the MD simulation result conforms with the classical theory of growth mode. In case 7, for hydrophobic surface the island type or VW growth mode takes place due to lower solid-liquid attraction of atoms than liquid-liquid attraction. In case 7, the nucleation and growth rate are also very slow compared to other cases. For case 1 with hydrophilic wetting condition throughout the surface solid-liquid attraction is considerably higher than the liquid-liquid attraction which resulted in layer by layer or FM growth mode. For cases 2-6 it is depicted that, growth mode is transformed from FM to VW mode with the decrement of hydrophilic content on hybrid wetting surface. For case 2, the growth mode can be considered as FM growth mode although the formation of initial complete layer takes place at a slower rate than case 1. Here, because of width of hydrophobic regions being very low, atoms migrated easily from hydrophobic region to hydrophilic region which resulted in layer-by-layer growth in case 2. For case 3, the growth mode noticed can be considered as SK growth mode where at first a layer of liquid atoms was formed on the solid surface on which cluster of liquid atoms started to grow on hydrophilic region. Initially, during the adsorption period, few atoms which nucleated on the hydrophobic region started to migrate spontaneously from the hydrophobic region which conforms to the study of Wang et al. [85]. But with the increment in thickness of liquid cluster on hydrophilic region, this migration rate started to decrease and growth of cluster started to expand to nearby hydrophobic region which eventually formed a complete layer of condensate on the solid surface. Hamaker constant is a coefficient whose magnitude reflects the van der-Waals force between two particles, or between a particle and a substrate [131]. The magnitude of Hamaker constant depends on the density of two particles and London coefficient in

the particle–particle pair interaction [132]. A recent study reported that with the increment of liquid film thickness, the value of Hamaker constant decreases [133] and it is known that liquid atoms have a tendency to move from region having lower Hamaker constant to higher Hamaker constant [134]. Thus, the condensed atoms dispersed from hydrophilic zone to nearby hydrophobic zone and formation of complete liquid layer took place. Then, after the formation of liquid layer, cluster of liquid atoms started to grow on hydrophilic region compared to that on the hydrophobic region which resulted in layer plus island or SK growth mode. But in case 5 and 6, the length of hydrophobic region was larger which hindered the growth of complete layer of liquid atoms on the solid substrate and allowed them to grow as an island on the hydrophilic region. The growth mode also depends on the strip size of hydrophilic-hydrophobic pattern. From figure 5.11, it is observed that the growth mode changed from VW (island type) to FM (layer by layer type) with the reduction of strip size. For strip size 8 nm in case 4A it is depicted in figure 5.11 that, the liquid atoms condensed at the right edge of the hydrophobic region can't migrate to hydrophilic region due to larger strip size. Earlier MD study has also confirmed that the motion of droplet is enhanced across the gradient surface when the width of the different wetting segment is smaller [85]. When the difference of thickness of liquid atoms is high, higher difference in Hamaker constant takes place between hydrophilic and hydrophobic zone. This difference has caused condensed atoms to disperse from hydrophilic to nearby hydrophobic zone but this dispersion is not good enough to form a complete layer due to relatively large strip size (8 nm). For this case cluster of liquid atoms is noticed at the edge of hydrophobic region apart from on the hydrophilic region. On the other hand, in case 4B and case 4C with smaller strip size, a continuous layer of atoms is formed on the solid surface due to higher migration rate and higher dispersion of atom from hydrophilic zone to nearby hydrophobic zone. For this reason, flat layer of condensed atoms was developed which ultimately resulted in layer-by-layer growth for patterned hybrid wetting surfaces with smaller hydrophilic-hydrophobic strip size.

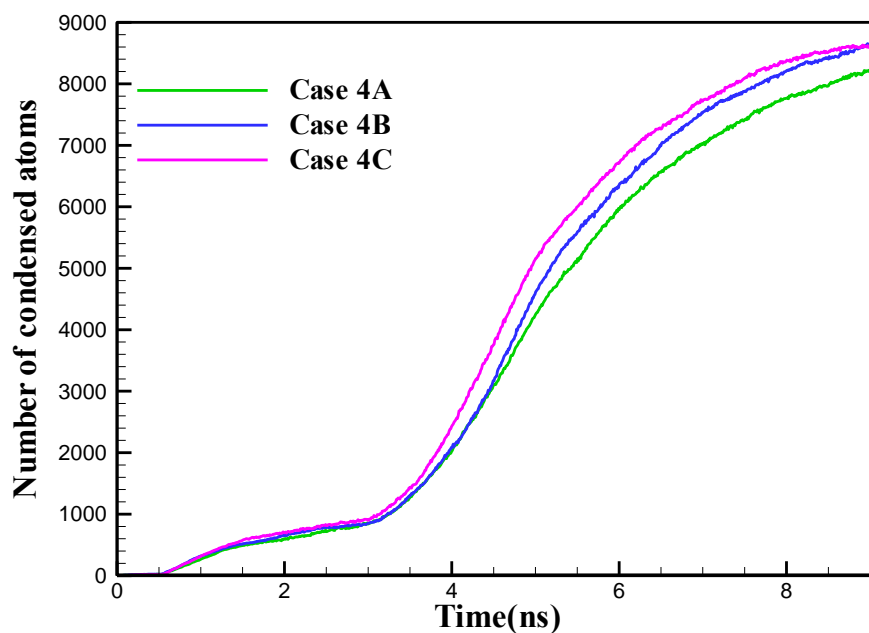
5.2.4 Transient condensation over different hybrid wetting surfaces at nanoscale

To explain the transient condensation characteristics of surfaces the number of condensed atoms and condensation mass flux, m_c has been plotted in figure 5.12 and figure 5.13. Figure 5.12 (a) and (b) shows the number of condensed atoms on top condensing surface under different hybrid wetting conditions while figures 5.13 (a) and (b) demonstrate transient condensation mass flux

calculated from the instantaneous slope of the condensation number vs time curves illustrated in figure 5.12 (a) and (b). From figures 5.12 (a) and (b) it is evident that at the beginning period of simulation, some of vapor atoms present in the simulation domain get adsorbed on the solid surface

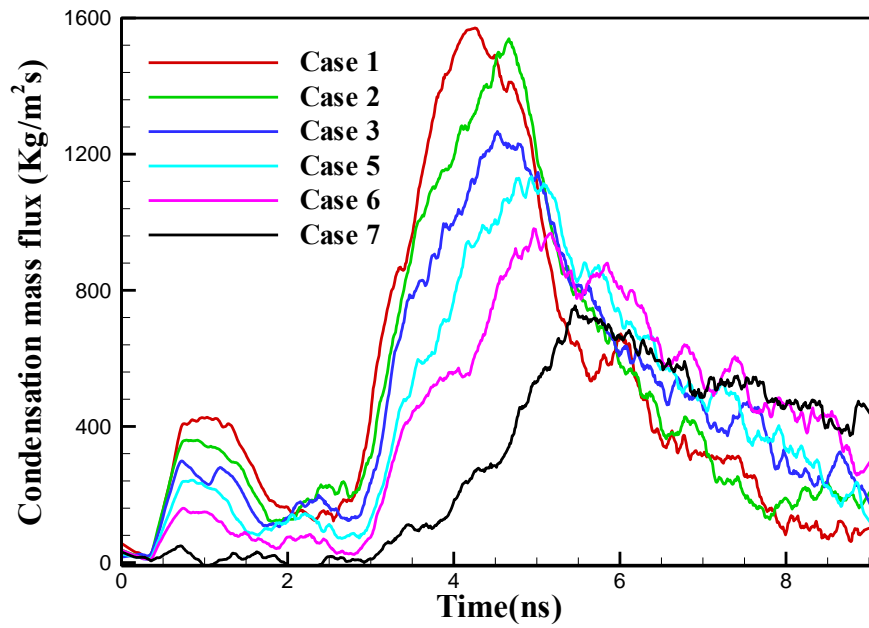


(a)

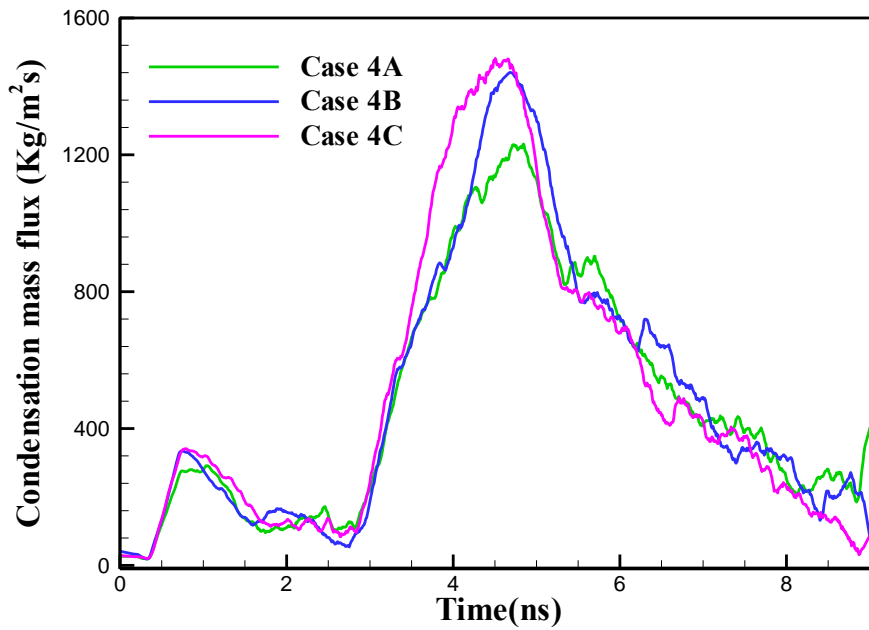


(b)

Figure 5.12: Temporal variation of number of condensed atoms in cases with (a) different portion of hydrophilic and hydrophobic region (b) different strip size having equal portion of hydrophilic and hydrophobic region.



(a)



(b)

Figure 5.13: Temporal variation of condensation mass flux at (a) different portion of hydrophilic and hydrophobic region (b) different strip size having equal portion of hydrophilic and hydrophobic region.

changing their phase from vapor to liquid by exchanging energy with the solid surface during the equilibration. Higher amounts of liquid atom were adsorbed on the surfaces with higher hydrophilic content and smaller strip size of hydrophilic-hydrophobic patterning. This adsorption rate started to decrease as the simulation proceed on which is readily traceable from figure 5.12 as the system started in reaching equilibrium near the end of equilibration stage. At the end of equilibration period (after 2.5 ns), the temperature of solid surface is increased to 130 K and liquid atoms started to get evaporated at a high rate from the bottom surface. The liquid atoms after being evaporated from the bottom surface started to condense on the top surface. From the previous studies [82,92], it is known that solid-liquid interfacial thermal resistance depends on the solid-liquid energy parameter (wettability of the solid surface) and remains constant during the entire simulation period [92]. This solid-liquid interfacial thermal resistance plays the most dominant role in the initial stage of condensation. For this reason, in our present study the value of condensation mass flux was higher with hybrid wetting surfaces having higher hydrophilic content or smaller strip size of hydrophilic-hydrophobic pattern (as shown in figure 5.13 (a) and 5.13 (b)). But with the elapse of time when the thickness of deposited liquid film is raised to a certain level the bulk thermal resistance of the liquid film becomes the most dominant factor [92]. In our study it is found that with the increment of hydrophilic content and decrement of hydrophilic-hydrophobic pattern strip size in case 1-6 the thickness and continuity of liquid film on the solid surface is increased (shown in figure 5.10 and 5.11) which eventually reduced condensation mass flux to a low value at later period as compared to the hybrid wetting surfaces with lower hydrophilic content and higher strip size. In case 7, the number of adsorbed atoms was very low (about zero) due to very high solid-liquid interfacial thermal resistance at low wetting surface. But the value of condensation mass flux is highest in the later period because in case 7, some of the solid surface was still unoccupied by the liquid atoms.

For this reason, vapor Argon atoms had more capability to exchange heat with solid surface compared to other cases in that period. From figure 5.12 (a) and (b) it is depicted that higher number of atoms were condensed on surfaces with higher hydrophilic content and smaller hydrophilic-hydrophobic pattern strip size. Since the condensation mass flux showed a different behaviour for various cases at initial and later period of simulation, time average condensation mass flux, $m_{c,avg}$ is calculated to estimate the overall performance of the condensing surface in all cases. From figure 5.16 it can be reported that the value of $m_{c,avg}$ is decreased with the

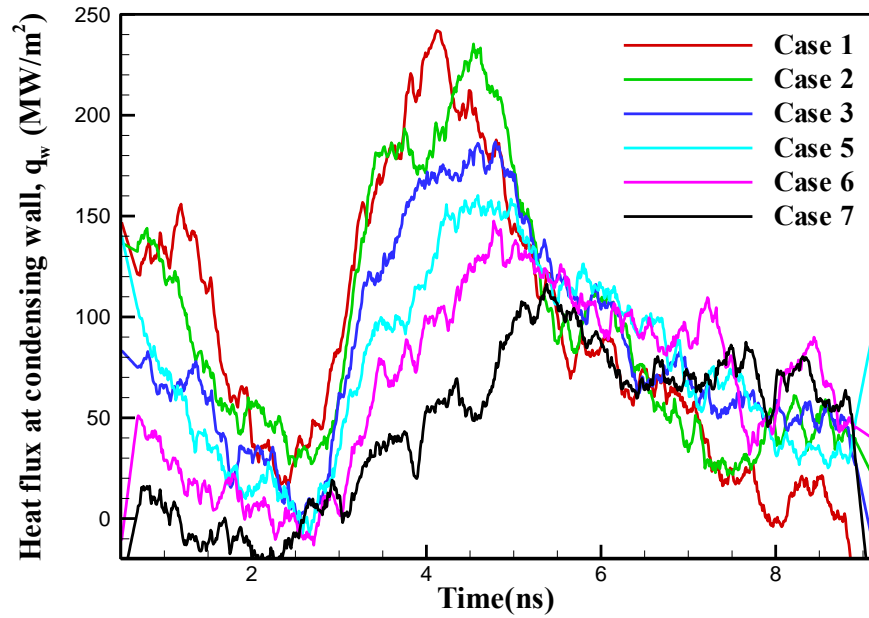
decrement of hydrophilic portion of the condensing surface. The average condensation mass flux is also calculated for case 4A, case 4B and case 4C having hydrophilic-hydrophobic pattern strip size of 8 nm, 4 nm and 2 nm respectively. The value of the average condensation mass flux as obtained for case 4A, 4B and 4C are 472.7, 482.4 and 490.4 kg/m²s respectively. So, from this discussion it can be said that the average condensation mass flux is increased with the increment of hydrophilic portion and decrement of strip size in patterned hybrid wetting surface.

5.2.5 Heat flux characteristics at the condensing wall

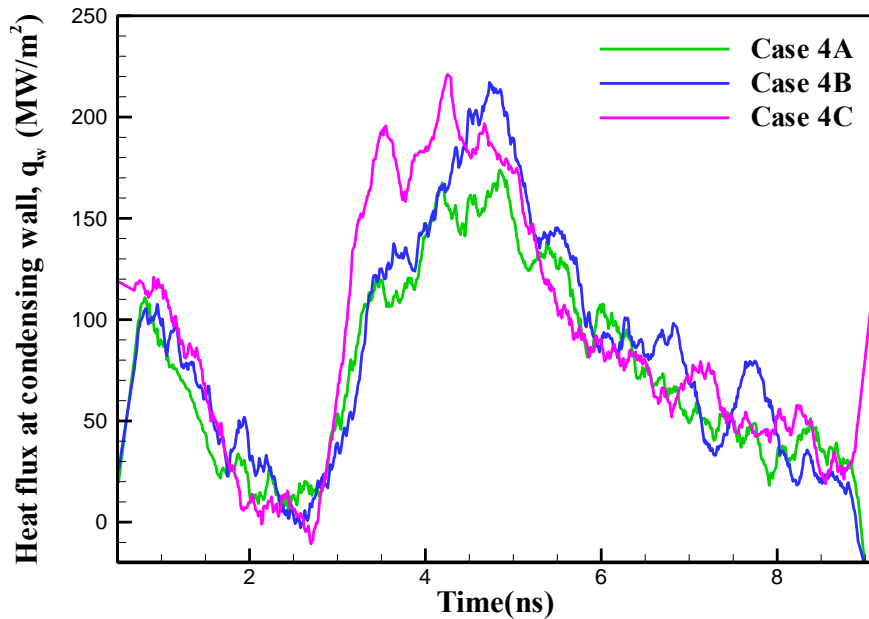
Heat flux at condensing wall, q_w represents the amount of energy transported from Argon atoms to the solid substrate per unit area and time. From MD study, Liang et al. [135] obtained the value of condensation heat flux in the range of 50-200 MW/m² for different thermal conditions which also complied with the Schrage's relationship [136]. The value of wall heat flux obtained in the present study for various system configurations as depicted in figure 5.14 is also in the same order of magnitude. From figure 5.14, it is evident that during the equilibration period the value of upper wall heat flux is higher for surface with higher fraction of hydrophilic region and smaller strip size of hydrophilic-hydrophobic patterning. This indicates that higher amount of energy is exchanged with the solid surface by argon atoms in cases of hybrid surfaces with higher hydrophilic fraction and smaller strip size of hydrophilic-hydrophobic patterning. Accordingly, the number of adsorbed atoms at the top condensing wall is also higher for these cases, which is clearly visible from the spatial number density profile of argon atoms as shown in figure 5.15.

From figure 5.14 it is also clear that as the system reaches towards equilibrium, exchange of energy from argon atoms to the condensing surface drops which has caused the value of wall heat flux to decrease to a very small value. In the non-equilibrium period, the argon atoms after being evaporated from the bottom surface started to get condensed on the top condensing surface. Initially, higher wall heat flux is observed due to higher amount energy exchange with an increment in number of condensed atoms. As shown in figure 5.14 (a), for cases 1-6, the value of heat flux at the condensing wall after attaining maximum value started to decrease. The maximum wall heat flux is found to be higher on the surface with larger hydrophilic content. This happens because hybrid wetting surface with higher hydrophilic fraction offers lower solid-liquid interfacial thermal resistance which causes the Argon atoms to exchange heat with solid surface at

a higher rate compared to the surface with lower hydrophilic fraction at the initial period of condensation. Also, the rate of decrement of heat flux at the condensing wall is the steepest in



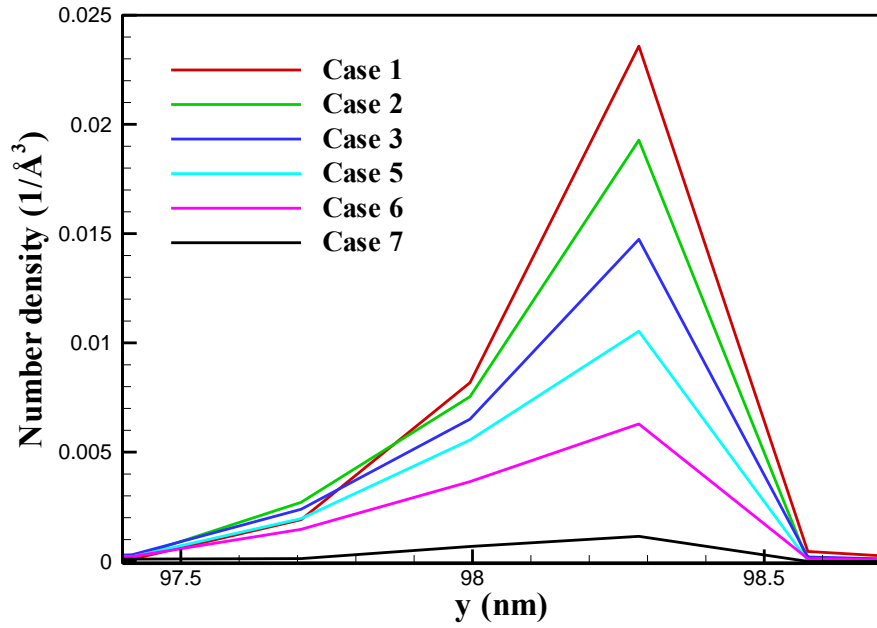
(a)



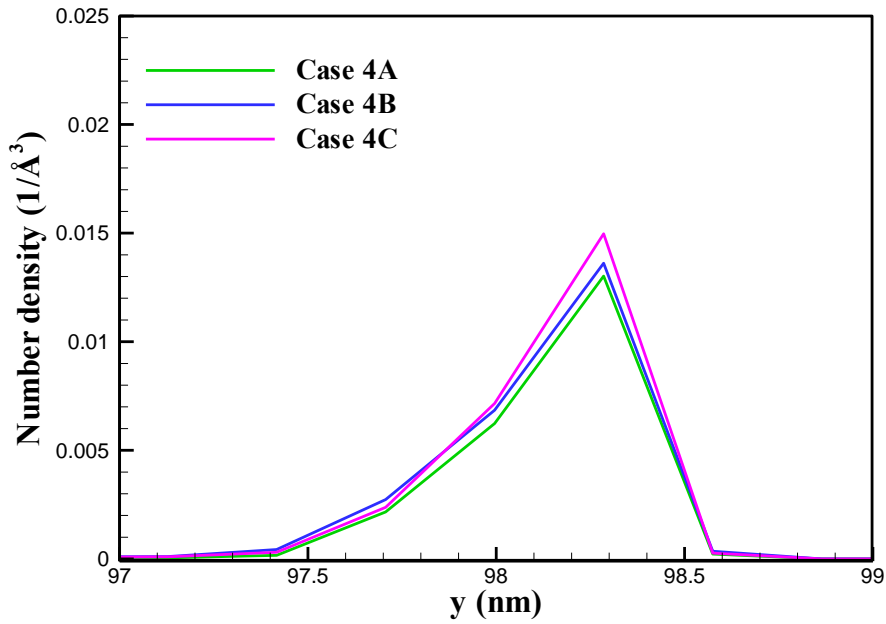
(b)

Figure 5.14: Temporal variation of heat flux at condensing wall for (a) different portion of hydrophilic and hydrophobic region (b) different strip size having identical portion of hydrophilic

and hydrophobic region.



(a)



(b)

Figure 5.15: Variation of number density profile of Argon atoms near the condensing wall at 2.3 ns for various cases with change in (a) fraction of hydrophilic and hydrophobic portion (b) strip size having equal portion of hydrophilic and hydrophobic region.

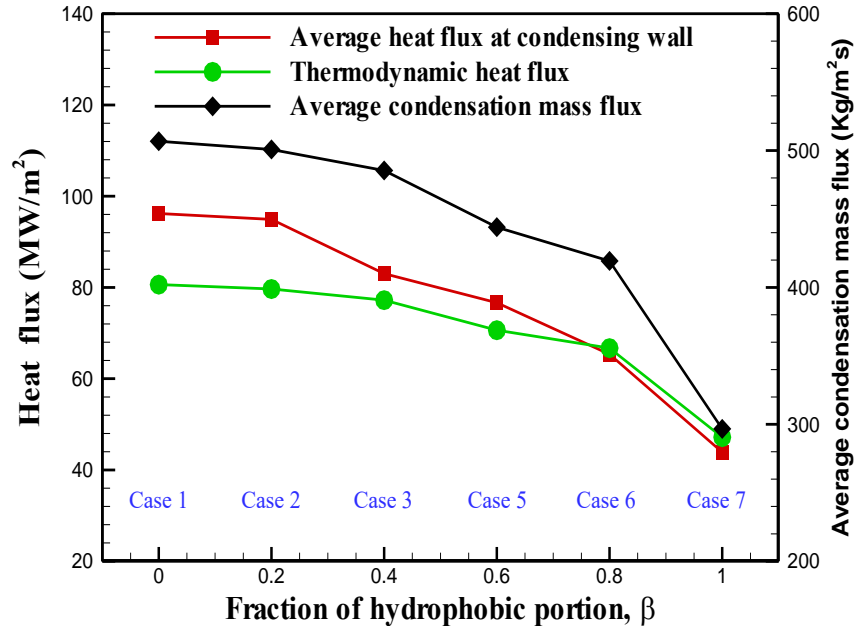


Figure 5.16: Variation of average condensation mass flux, average heat flux at condensing wall and thermodynamic heat flux for different cases with change in fraction of hydrophobic and hydrophilic portion.

cases with condensing surface having higher hydrophilic fraction. The reason can be attributed to the fact that in cases of surfaces with higher hydrophilic fraction, continuity of condensed atoms' layer is increased (as shown in figure 5.10) which acts as a barrier for vapor atoms to exchange heat with solid substrate and this bulk thermal resistance becomes the dominant factor at the later period of condensation [92]. Due to this reason, at later stage (after 7 ns) it has been found that surface with lower hydrophilic portion offered higher wall heat flux than the surfaces with larger hydrophilic portions. From figure 5.14 (b) it is also evident that hybrid wetting surface with smaller hydrophilic-hydrophobic strip size results in higher maximum wall flux due to its provision of easier local migration of atoms from hydrophobic region to hydrophilic region at the initial period of condensation. But at later stage (after 6.5 ns), as it is shown in figure 5.11, a continuous layer of liquid film was yet to form on condensing surface in case 4A which resulted in higher amount of wall heat flux compared to case 4B and case 4C due to lower bulk thermal resistance in this case. Therefore, the heat flux at the condensing wall shows different behaviour at initial and later period of simulation depending on wetting configuration of the hybrid surface. For this reason, time average value of heat flux at the condensing wall, $q_{w,avg}$ has been calculated. As shown in figure 5.16, the average value of heat flux at condensing wall is increased with the increment of

hydrophilic fraction of hybrid wetting surface. For comparing the result of our present MD study with the classical thermodynamic study, namely in terms of thermodynamic heat flux, q_{therm} , is calculated based on time average consideration of phase change process at the condensing wall temperature. From the comparison of $q_{w,\text{avg}}$ and q_{therm} as presented in figure 5.16, the present MD results is in good agreement with classical thermodynamic approach.

The value of $q_{w,\text{avg}}$ and q_{therm} for case 4A, case 4B and case 4C are 72.4, 80.2, 90.3 MW/m² and 75.2, 77.5, 78.0 MW/m² respectively. Thus, it is evident that both the average wall heat flux ($q_{w,\text{avg}}$) and thermodynamic heat flux (q_{therm}) attain higher value with the decrement of strip size of hydrophilic-hydrophobic patterning. Previously, Peng et al. [86] performed an experimental study on vertical hydrophilic and hydrophobic patterned hybrid wetting surface where they changed the width of the hydrophilic-hydrophobic stripes and observed that with the decrease of width of the hydrophilic-hydrophobic stripes the heat transfer performance of the hybrid wetting surface has been improved. The results of the experimental study in large scale conforms qualitatively with the results of our current work. Thus, from the above results of the present study, it can be concluded that the condensation performance is improved with the increment of hydrophilic fraction and decrement of hydrophilic-hydrophobic strip size of patterned hybrid wetting surface.

5.2.6 Local surface tension profile near the condensing wall

Due to the substantial anomaly between normal and tangential pressure components a significant value of surface tension is obtained at the liquid-vapor interface. In this study, mechanical approach is used to obtain the local liquid-vapor interfacial surface tension by integrating the difference between normal and tangential pressure components of a group of atoms. The simulation domain is divided into 5899 two dimensional bins where each of the bins is of 1 nm x 0.2895 nm along x and y axis respectively. Then, the surface tension is calculated using equation (4.12). Same approach was adopted by Ghahremanian et al. [95] for similar kind of atomic system. It is known that in bulk liquid and bulk vapor each atom is attracted equally by all neighbour atoms which causes the surface tension to be equal to zero. But during condensation at the liquid-vapor interface the atoms are more strongly attracted by the liquid atoms than the vapor atoms. For this reason, a finite value of surface tension is obtained at the liquid-vapor interface [137]. From the previous studies, it is known that the thickness of the liquid-vapor interface is in the range of 1.5 nm-3 nm [138–140]. The thickness of the liquid-vapor interface shown in figure 5.17 agrees with the results of the previous works. From figure 5.17, it can be reported that the interfacial area is increased with the increment of hydrophilic content in

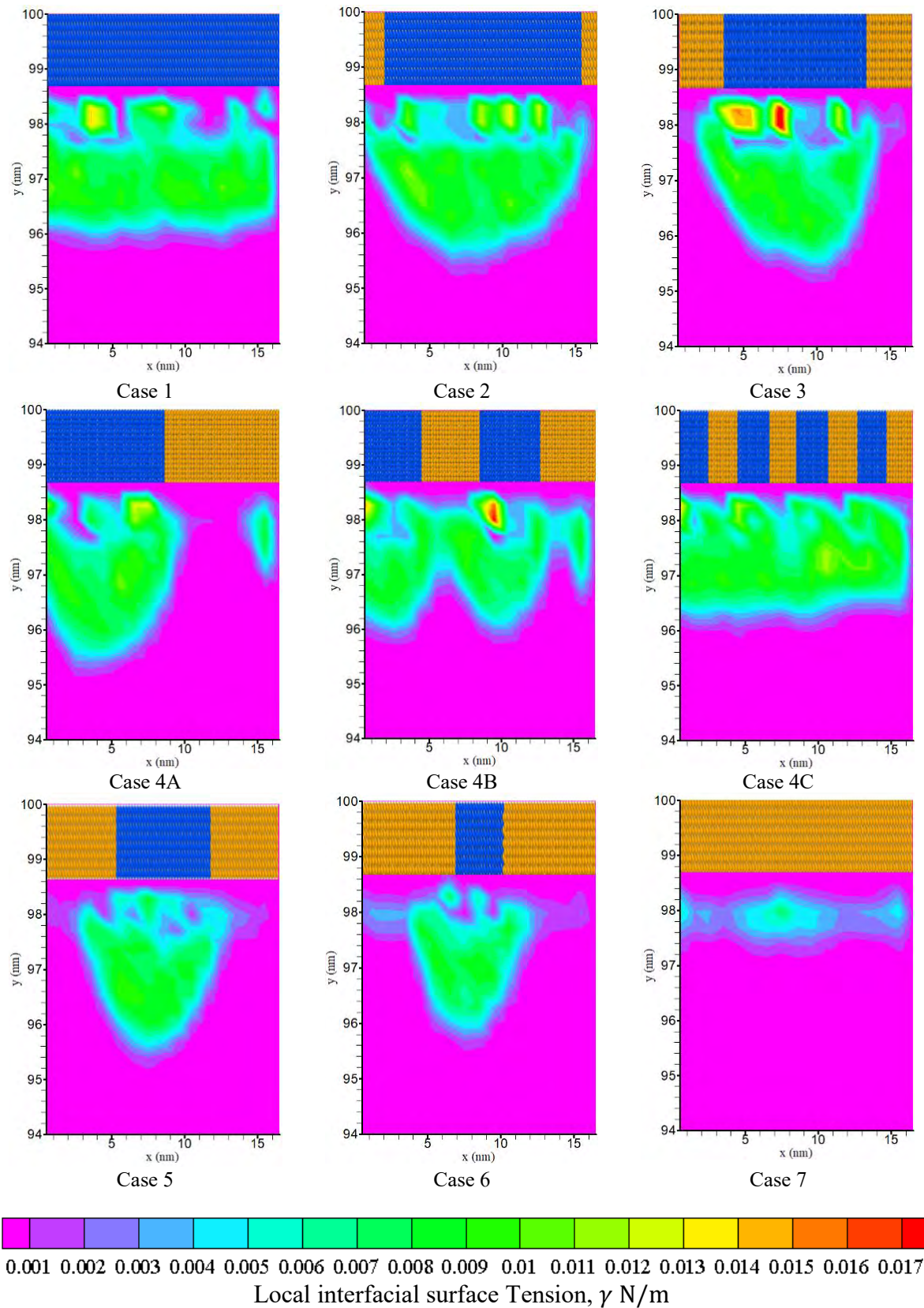


Figure 5.17: Contour plot of local liquid-vapor interfacial surface tension at 4.5 ns.

hybrid wetting surface and decrement of hydrophilic-hydrophobic strip size of hybrid wetting surface. From the previous studies [126,141,142], it is already known that higher liquid-vapor interfacial area offers more heat transfer during liquid-vapor phase change process. So, it can be concluded that patterned hybrid wetting surface with higher hydrophilic fraction and smaller strip size offer better performance in condensation heat transfer.

5.3 Effect of gradient and patterned wetting configuration

Table 5.1: Overview of all the cases of condensing surface.

Case	Wetting profile of condensing surface	Hydrophilic fraction, α	Hydrophobic fraction, β
Case 1A	FWG ($p = 4$)	0.8	0.2
Case 2A	FWG ($p = 1.5$)	0.6	0.4
Case 3A	FWG ($p = 0.67$)	0.4	0.6
Case 4A	FWG ($p = 0.25$)	0.2	0.8
Case 1B	Patterned	0.8	0.2
Case 2B	Patterned	0.6	0.4
Case 3B	Patterned	0.4	0.6
Case 4B	Patterned	0.2	0.8

In this section, the condensation characteristics of a hybrid wetting surface for different wetting profile such as strip patterned and functional wettability gradient configuration has been discussed. All the hybrid wetting condensing surfaces have been modelled with Platinum atoms having two different wetting characteristics i.e., hydrophilic and hydrophobic with a value of ϵ_r equal to 2 and 0.5, respectively. In this section, cases with FWG and patterned wetting profiles are classified into groups A and B, respectively. Different cases are modelled following the variation in hydrophilic-hydrophobic proportions of the condensing surface. All of the FWG and patterned surfaces are modelled following the method delineated in section 4.1. The wetting profile of the bottom surface is kept fixed at hydrophilic condition to ensure equal number of evaporated atoms from the bottom surface in all of the cases while the wetting profile of the condensing surface is changed with a view to study the condensation characteristics of different hybrid wetting surfaces. Eight different

cases of hybrid wetting surfaces are considered in this section for achieving this objective. Table 5.1 provides the overview of configuration of different types of hybrid wetting surface considered in this section. The hydrophilic proportion is reduced from 80% hydrophilic- 20% hydrophobic combination in case 1 to 20% hydrophilic-80% hydrophobic combination in case 4 with a decrement of 20% in each case for both FWG and patterned surfaces configuration as shown in table 5.1. Figure 5.18 demonstrates the initial configuration of the simulation domain and wetting profile of all the condensing surfaces.

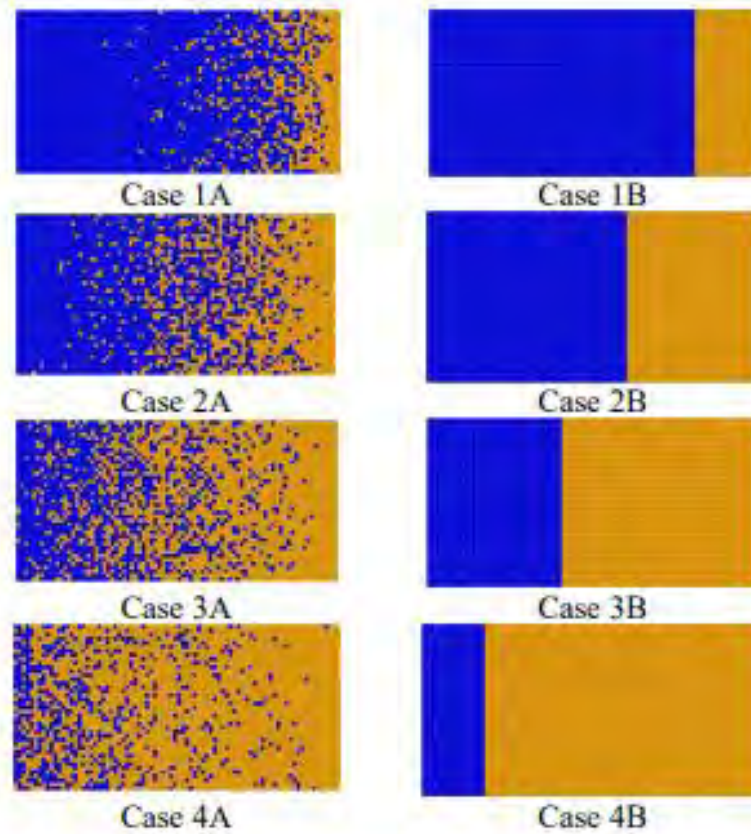
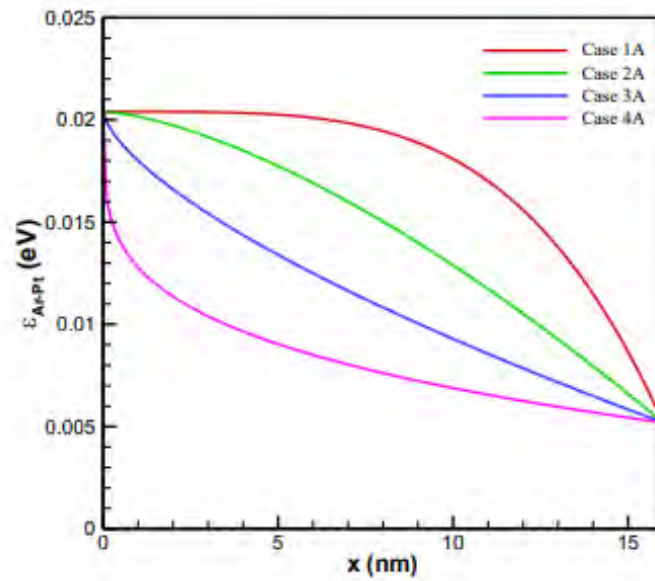


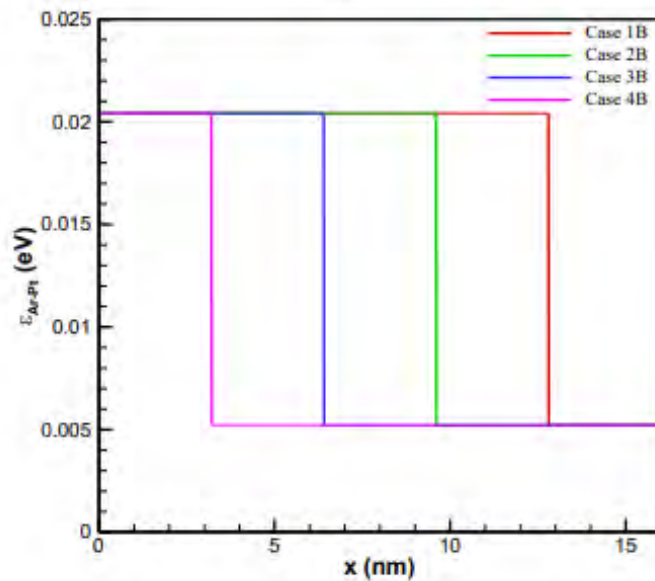
Figure 5.18: Wetting profile of the condensing surface in different cases.

The numerical representation of solid liquid energy parameter of argon and platinum, ϵ_{Ar-Pt} in figure 5.19 illustrates the wettability gradient of all the cases considered in this section. The area under each curve indicates the total hydrophobic proportion in each case. The nanoscale condensation characteristics of all these different cases of the hybrid wetting surfaces are analysed and compared by evaluating necessary condensation parameters such as system characteristics, solid-liquid interfacial thermal resistance, nucleation, coalescence and growth of the condensate,

number of condensed atoms, condensation mass flux, heat flux at the condensing wall and surface tension profile near the condensing surface.



(a)



(b)

Figure 5.19: Wettability gradient profile, namely, the spatial variation of the Ar-Pt energy parameter, ϵ_{Ar-Pt} for different (a) FWG (group A) and (b) patterned surfaces (group B).

5.3.1 Transient variation of system behavior

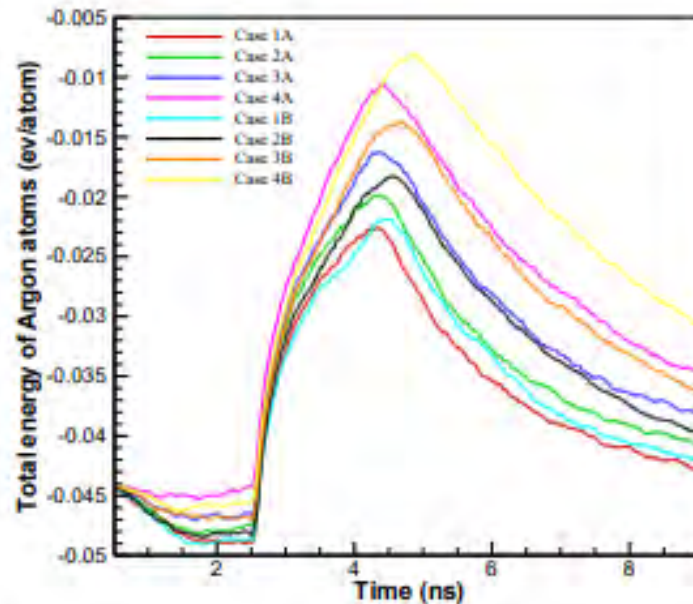
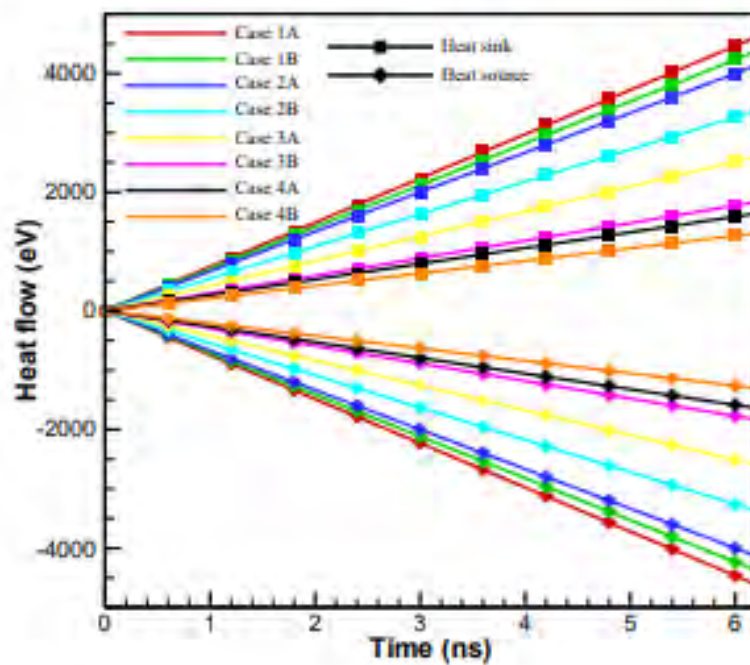


Figure 5.20: Temporal evolution of total energy of fluid atoms for different cases.

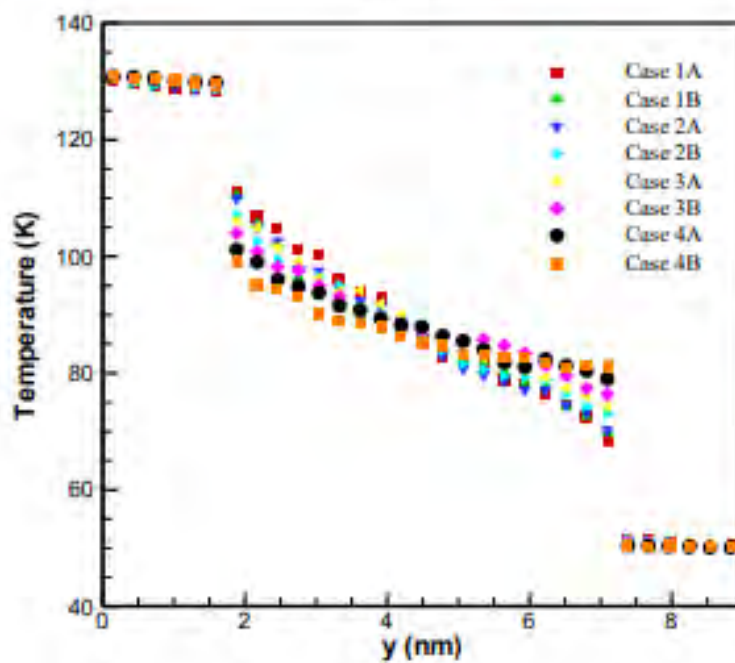
Figure 5.20 illustrates the temporal evolution of the total energy of fluid atoms. The numerical value of per atom total energy conforms with the earlier findings of similar atomistic system [125]. From the constant value of total energy for all cases at the time interval 2–2.5 ns, it is quite evident that the entire system has achieved thermal equilibrium before the onset of the non-equilibrium period. Due to the elevation of the lower surface's temperature to 130 K, argon atoms were energized, which is noticed from figure 5.20. The energized atoms of the vapor phase eventually started to condense on the top surface by dissipating heat to that one, resulting in a decrement of total energy. Thus, the lower value of total energy indicates a higher condensation rate as compared to the higher ones. From figure 5.20, considering all cases, it can be reported that condensation process is faster in FWG surfaces than in patterned surfaces having identical hydrophilic-hydrophobic proportions, and the condensation rate is enhanced with the increase of the fraction of hydrophilic atoms.

5.3.2 Thermal resistance at the solid-liquid interface

To elucidate the condensation characteristics over different cases of hybrid wetting surfaces, solid-liquid interfacial thermal resistance, R_{int} is evaluated using equation (5.1) for a simulation



(a)



(b)

Figure 5.21: (a) Temporal evolution of heat flow across source and sink (b) Spatial distribution of temperature of the fluid atoms along the direction of heat flow.

domain as shown earlier in figure 5.7 following the methodology delineated in section 5.2.2. Under this atomistic configuration, the simulation is performed in an NVE ensemble by setting the

temperatures of the source and sink at 130 K and 50 K, respectively, following an NVT ensemble of the whole system at 90 K. The simulation was conducted for 6.2 ns and the data was recorded after a timestep of 5 fs. The heat flow and spatial distribution temperature shown in figure 5.21 follow the behavior of the earlier findings both qualitatively and quantitatively [126,127]. Solid-liquid interfacial thermal resistance, R_{int} , is calculated for different cases using equation (5.1), utilizing the simulation data q and ΔT from figure 5.21. The value of R_{int} plotted in Figure 5.22 for different cases is in the same order of magnitude with the earlier findings [126–129].

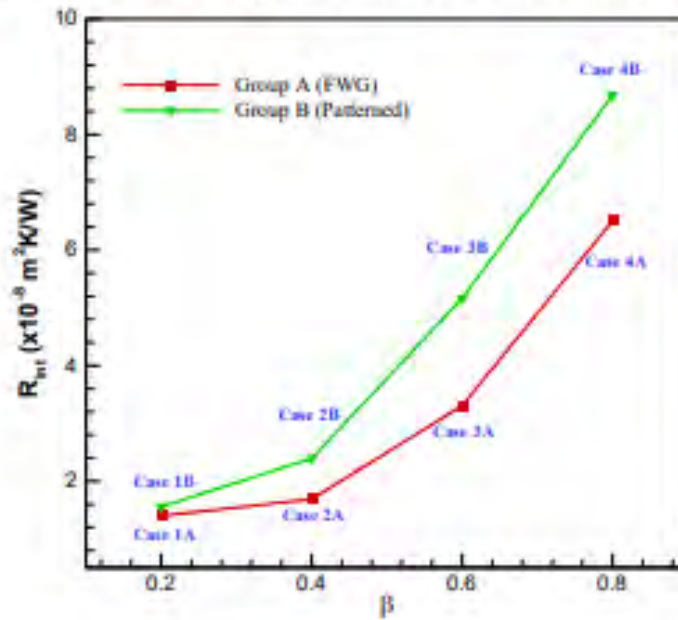


Figure 5.22: Solid-liquid interfacial thermal resistance, R_{int} for various cases of FWG and patterned hybrid wetting surface.

The value of R_{int} has decreased with the increase of the fraction of hydrophilic atoms in both patterned and FWG surfaces. It is observed that the value of R_{int} of the FWG surface is lower than the patterned one under an identical proportion of hydrophilic and hydrophobic atoms. As shown in figure 5.22, with the increase of the hydrophobic fraction, the difference in solid-liquid interfacial thermal resistance between FWG and the patterned surface has increased owing to the decrement of the spread of hydrophilic atoms compared to the FWG surface.

5.3.3 Nucleation, coalescence and growth characteristics

To define the liquid cluster the Ten Wolde and Frenkel criterion [143] is employed in this study, which is proven to provide good results for L-J atoms like argon [144]. $1.5\sigma_{A_0-A_0}$ is taken as the

critical radius in the cluster analysis of the condensed atoms [69,73,144]. Also, clusters in which the atoms are within a $3.5\sigma_{Ar-Ar}$ distance away from the solid surface are considered as the surface clusters of condensed atoms in this study [73]. According to the classical nucleation theory (CNT), Gibbs free energy barrier must be transcended for the development of a stable nucleus in the condensation process. The Gibbs free energy barrier, G^* is expressed in equation (5.2) as,

$$G^* = \frac{16 \pi \gamma_{lv}^3}{3 \rho_l^2 \Delta\mu^2} F \quad (5.2)$$

Sheng et al. [68] and Pu et al. [73] have demonstrated that the value of G^* is reduced in the case of condensation on surfaces having a larger value of the solid-liquid energy parameter.

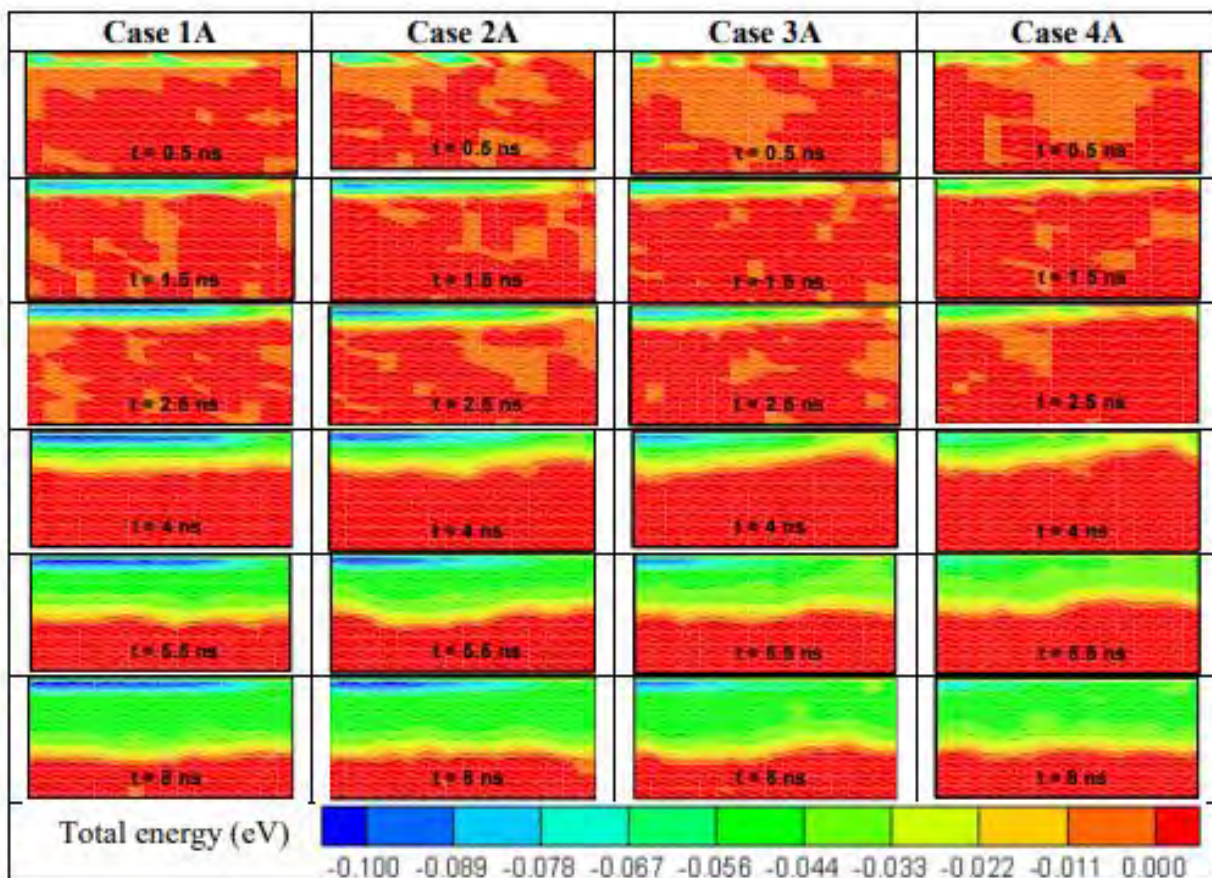


Figure 5.23: Total energy contour of the fluid atoms at the vicinity of the condensing surface for different cases of FWG configuration.

As a result, in comparison to the hydrophobic zone, the hydrophilic region will operate as a preferential site for condensate nucleation. So, the argon atoms have started to nucleate on platinum atoms with hydrophilic wettability. Then, the condensed atoms act as a region of lower energy, and the vapor atoms start to condense on this layer by dissipating their energy to the condensed atoms of earlier timesteps (see figures 5.23 and 5.24) [73]. Thus, the layer of condensate starts to grow on top of the earlier layer of condensed atoms. Furthermore, earlier research has illustrated that during condensation, droplets spontaneously transit from a low to a high surface energy zone [84].

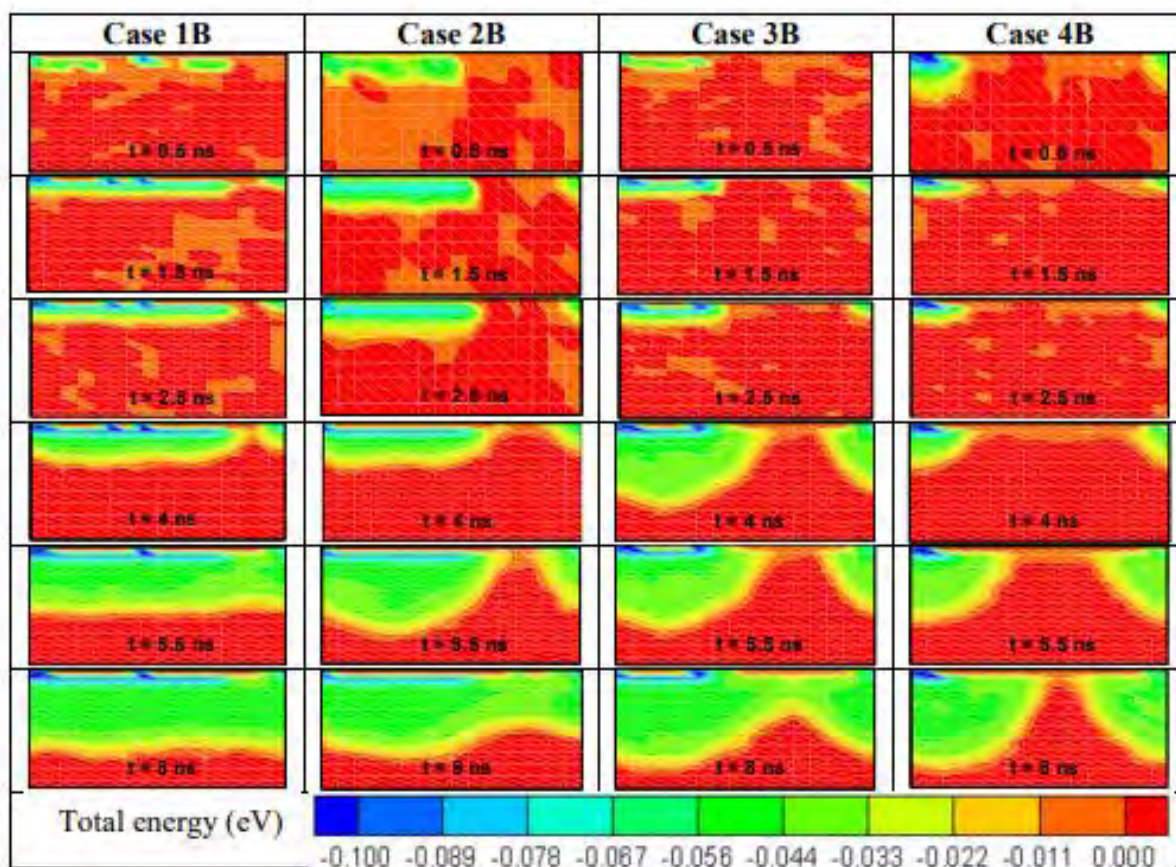
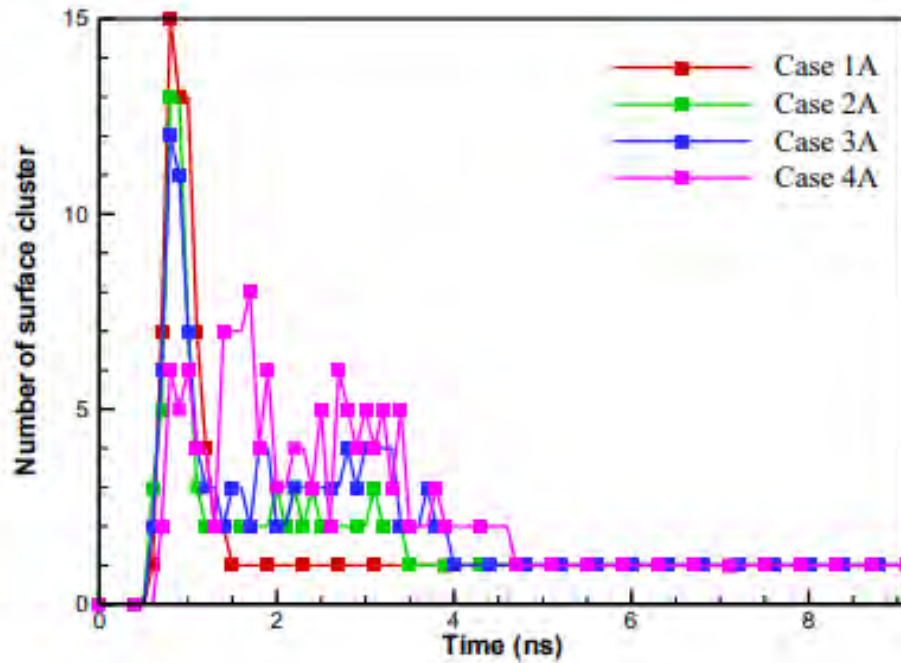
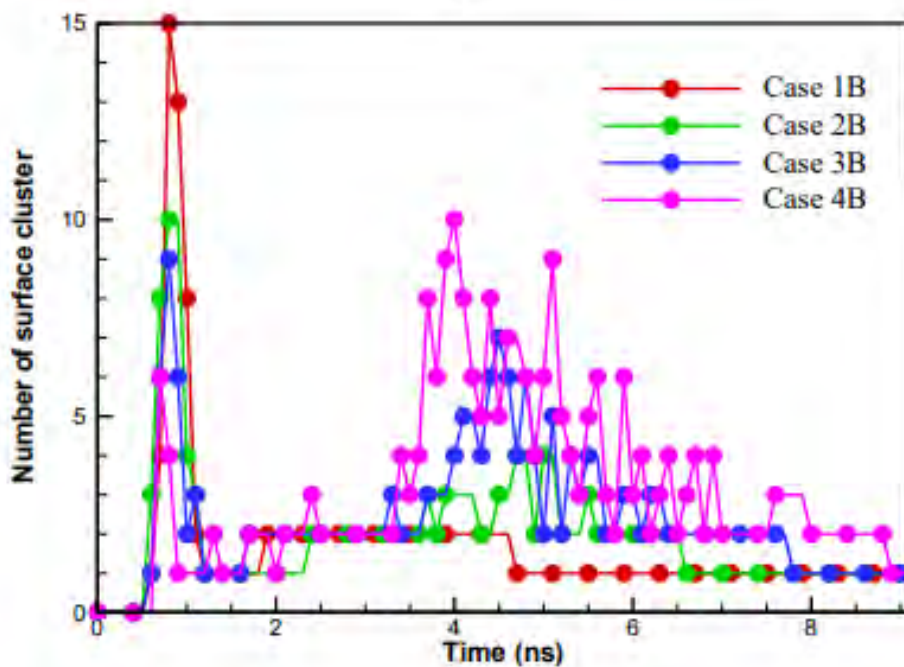


Figure 5.24: Total energy contour of the fluid atoms at the vicinity of the condensing surface for different cases of patterned wetting configuration.



(a)



(b)

Figure 5.25: Temporal variation of surface clusters for (a) FWG condensing surfaces, (b) patterned condensing surfaces.

As a result of the aforementioned facts, at the initial stage the number of surface clusters appears to grow faster with an increase in the fraction of hydrophilic atoms in both patterned and FWG

surfaces in figures 5.25 (a) and (b). When comparing the number of surface clusters between FWG and patterned surfaces, it's clear that the disparity widens in cases where the fraction of hydrophobic atoms is higher, such as case 2 (60% hydrophilic-40% hydrophobic) and case 3 (40% hydrophilic-60% hydrophobic). In case 1 (80% hydrophilic-20% hydrophobic), the atomistic distribution of platinum atoms with hydrophilic wetting conditions is almost equal (shown in figure 5.18), indicating that there are nearly equal numbers of preferential nucleation sites. The number of nucleation sites is quite low in case 4 (20% hydrophilic-80% hydrophobic) due to the reduced fraction of hydrophilic atoms. As a result, for both FWG and patterned surface conditions, the number of surface clusters is lowest in case 4. Because the dispersion of hydrophilic atoms on patterned surfaces is limited to a small region compared to FWG surfaces, clusters form quickly due to the small distance between them. However, in case 1, the rate of coalescence is approximately comparable on FWG and patterned surfaces due to the nearly equal atomistic distribution of hydrophilic atom on both types of surfaces. Among the different cases of patterned and FWG surfaces, it has been noticed that with the increase of the hydrophilic fraction of atoms, filmwise condensation mode (number of surface cluster equal to 1) has started earlier. Following our previous explanation, a layer of new liquid atoms grows on top of the preceding layer of condensate as time passes. With the increase in condensate, the bulk thermal resistance began to rise [92]. The local thickness of condensate over the hydrophilic region of cases with patterned surfaces is greater than the FWG surfaces of identical hydrophilic-hydrophobic combinations due to the nonuniformity of the condensate layer along the surface (see figure 5.23 and figure 5.24). It results in a high value of bulk thermal resistance. According to findings of earlier study, when the thickness of the condensate is high, the effect of bulk thermal resistance of the condensate outweighs the effect of interfacial resistance [92]. As a result, at a later stage of simulation on various patterned surfaces, some clusters of condensates have started to develop on the hydrophobic zone (illustrated in figure 5.24 and figure 5.27). These newly formed clusters have started to grow and consolidate like those above the hydrophilic region in the initial stage. The rate of coalescence of clusters into a single cluster accelerates as the condensing surface's hydrophilic atom content rises. This happens because of the reduction of distance between surface clusters with the increment of fraction of hydrophilic atoms and it facilitates the liquid clusters to merge with the nearby relatively easily compared to the surfaces with the lower fraction of hydrophilic atoms. Figure 5.26 shows that in the nonequilibrium period,

several discrete clusters of small size form at the nucleation sites on the FWG surfaces in cases 2A, 3A, and 4A, which finally consolidate into a single cluster after a finite time. Similar to the patterned surfaces, the time required to form a single film decreases as the percentage of hydrophilic atoms increases in FWG surfaces. Due to the reduced energy content of liquid atoms, once a complete film is developed, the filmwise condensation mode proceeds over the existing condensed layer, as seen in figure 5.23. When comparing the cluster growth features of FWG and patterned surfaces in figure 5.25, it can be concluded that under identical hydrophilic-hydrophobic content, filmwise condensation mode develops earlier on FWG surfaces than on patterned surfaces. Previous researches have shown that at the nanoscale the filmwise condensation mode is more favorable to heat transfer compared to the dropwise condensation mode. As a result, in terms of condensation heat transfer enhancement, the FWG surface is preferable to patterned surfaces. According to classical nucleation theory (CNT), the nucleation rate, J is expressed as,

$$J = \rho_f Z f^+ \exp\left(-\frac{\Delta G_c}{k_B T}\right) \quad (5.3)$$

Where ρ_f is the numerical density of the vapor, Z is the Zeldovich factor; f^+ is the particle addition rate of the critical cluster, which is related to the diffusion rate of the molecules; ΔG_c is the free energy barrier for forming a critical cluster; k_B is the Boltzmann constant; and T is the absolute temperature of the liquid phase. The expression for Z is as follows:

$$Z = \sqrt{\frac{\Delta\mu}{6\pi k_B T N_c}} \quad (5.4)$$

where $\Delta\mu$ is the difference in potential chemical energy between the gas phase and the liquid phase; and N_c is the number of molecules in the critical cluster.

Yang et al. [35] demonstrated that the high wetting characteristic of the surface increases the Zeldovich factor, Z which further increases the value of J resulting in higher nucleation rate on the hydrophilic surface than hydrophobic one.

The approach employed by Yasuoka and Matsumoto [69], Tanaka et al. [70], and Xu et al. [71] to calculate the nucleation rate, J is followed in our study. According to CNT, for the stability of a nucleus, the liquid cluster has to contain a minimum number of atoms [69]. This critical size of nucleus is denoted by n^* . Yasuoka and Matsumoto [69] reported that for nucleating on a flat surface, n^* is equal to 9.6 in order to develop a stable nucleus by surpassing the Gibbs free energy

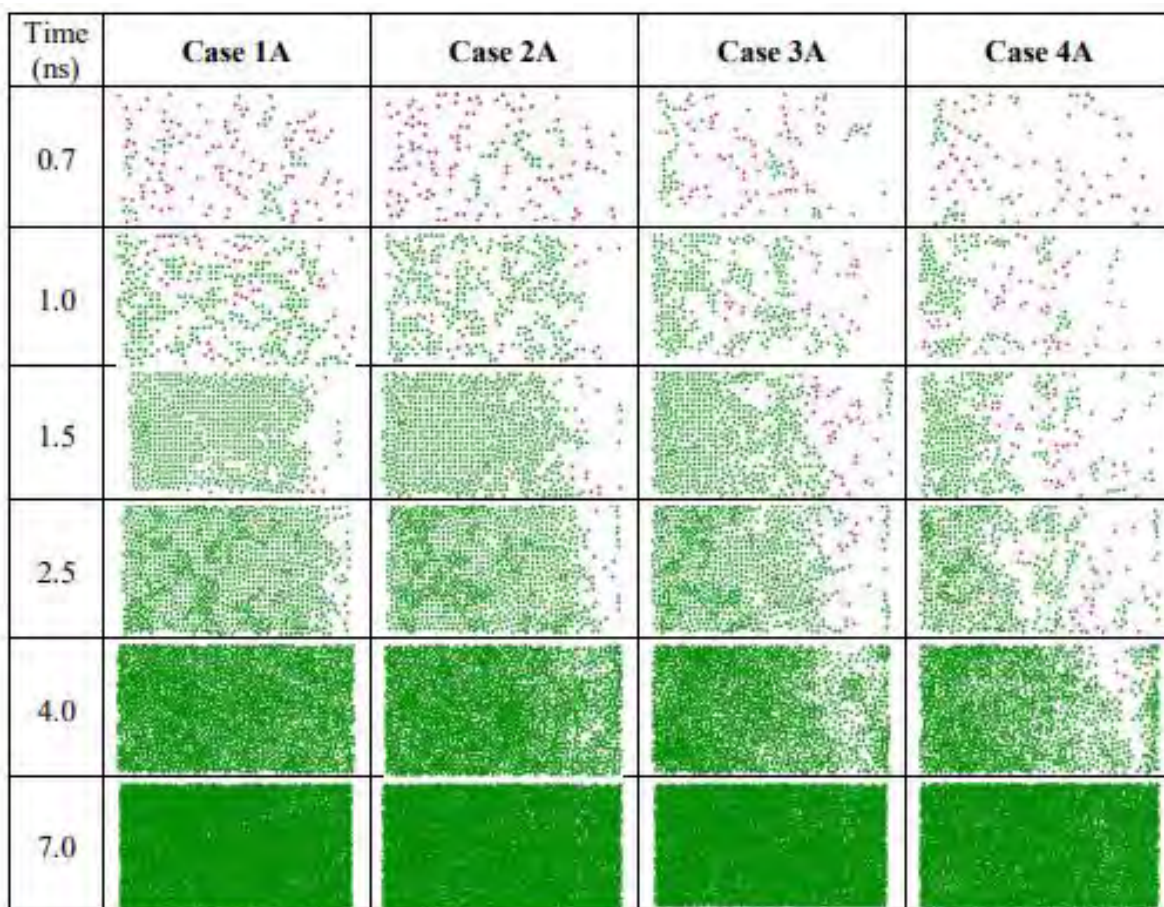


Figure 5.26: Snapshots of surface cluster on condensing surface (z-x plane) at different timesteps for different cases of FWG surfaces (Green color indicates the condensed argon atoms in the surface clusters and pink color indicates condensed argon atoms not in any surface cluster).

barrier (expressed in equation 5.2). Following this analogy, in our study a threshold size of 10 is used to identify the number of stable nuclei [69,71]. Figure 5.28 show that the number of nuclei initially grows in a linear fashion with time. Due to cluster coalescence, it has started to diminish after reaching its maximum value. Xu et al. [71] found similar results for the same value of ϵ_r in their study. The nucleation rate, J is then calculated using the slope of the number of surface clusters above a threshold size vs. time curve (figure 5.28). The nucleation rate for the various cases stated in table 5.2 agrees with the earlier finding in terms of order of magnitude [71]. Table 5.2 shows that the nucleation rate, J in the FWG surfaces is higher than the patterned surfaces for the same hydrophilic-hydrophobic composition. It is also observed that in circumstances where

there is a larger proportion of hydrophobic atoms, the disparity is greater. Larger value of nucleation rate on cases with larger hydrophilic proportion in table 5.2 conforms qualitatively with the CNT.

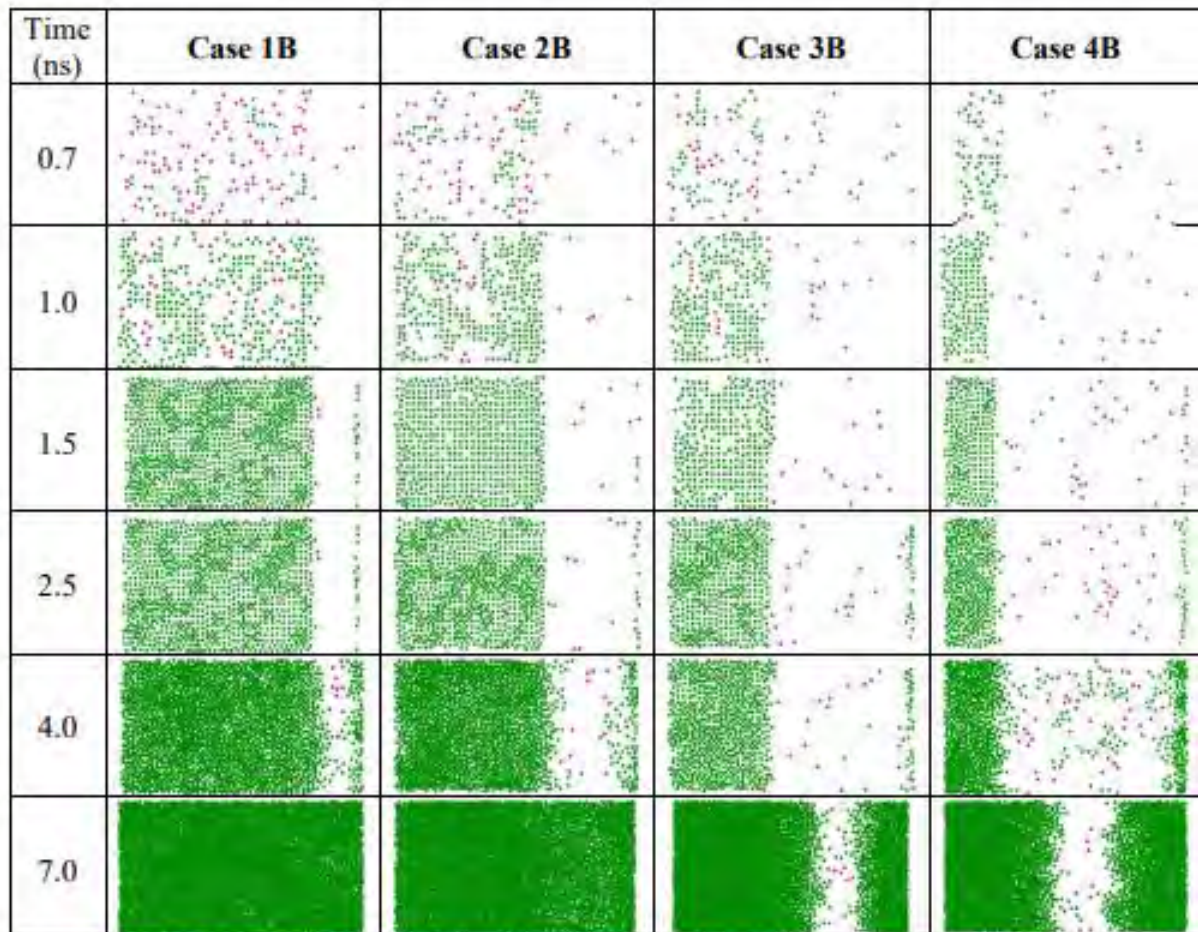
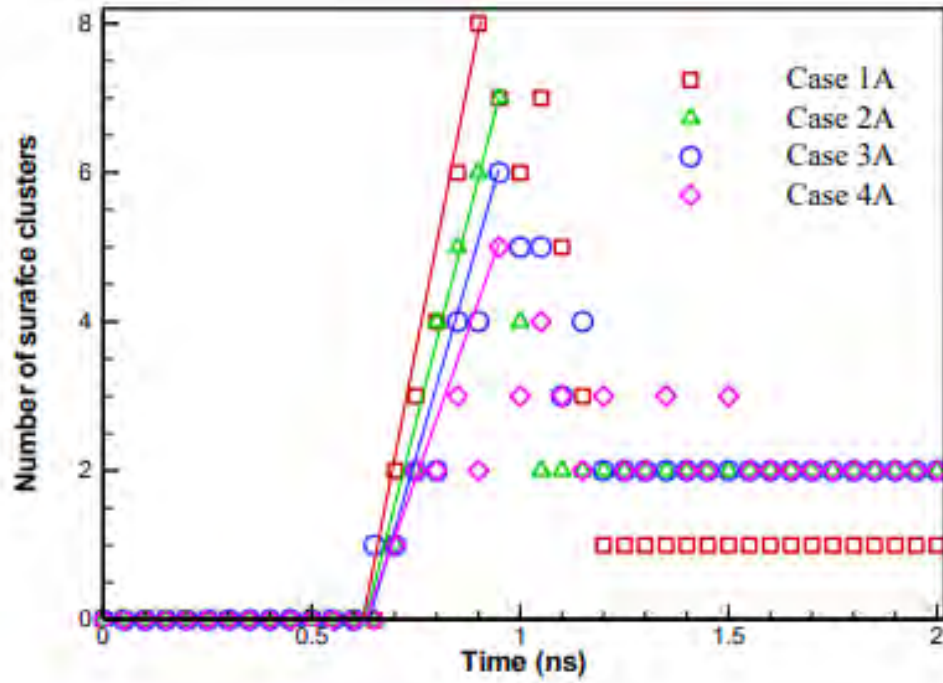
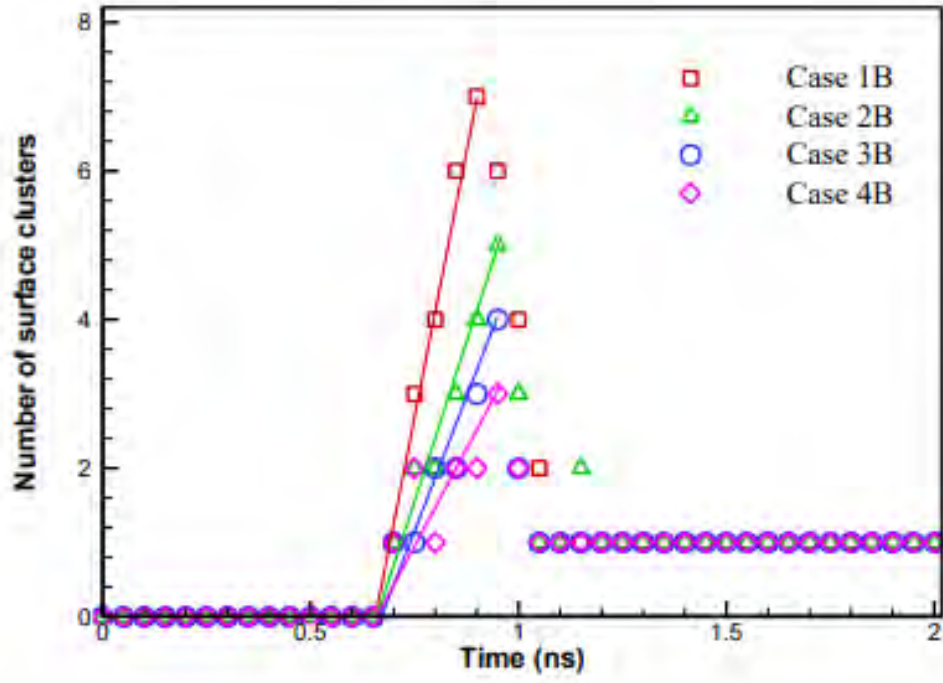


Figure 5.27: Snapshots of surface cluster on condensing surface (z-x plane) at different timesteps for different cases of patterned surfaces (Green color indicates the condensed argon atoms in the surface clusters and pink color indicates condensed argon atoms not in any surface cluster).



(a)



(b)

Figure 5.28: Temporal variation of surface clusters above threshold sizes for (a) FWG condensing surfaces, (b) patterned condensing surfaces.

Table 5.2: Rate of nucleation, J for different cases.

Cases	Nucleation rate, J ($\times 10^{25} \text{ m}^{-2} \text{ s}^{-1}$)
Case 1A	25.0
Case 2A	18.2
Case 3A	15.6
Case 4A	13.0
Case 1B	21.9
Case 2B	12.5
Case 3B	9.4
Case 4B	6.3

5.3.4 Transient condensation over different hybrid wetting surfaces

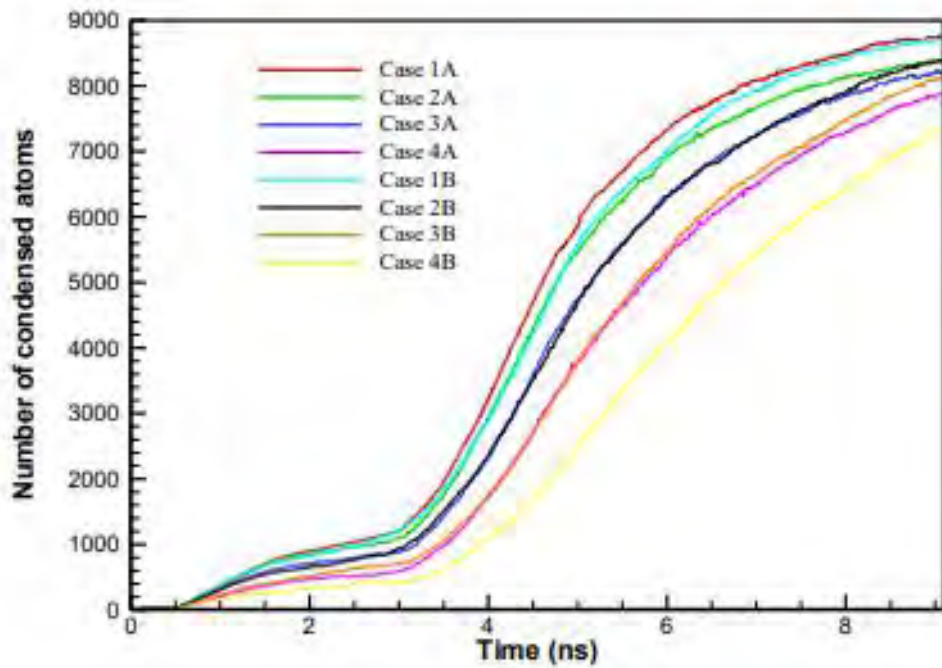
To estimate the temporal variation of condensation performance on different types of surfaces, the amount of condensed fluid atoms and condensation mass flux are calculated as depicted in figure 5.29 (a) and (b).

Figure 5.29 (a) shows that some fluid atoms were adsorbed on the condensing surface prior to the commencement of the non-equilibrium period. On surfaces having a larger proportion of hydrophilic atoms, the volume of adsorbed atoms was higher. Because of their lower solid-liquid interfacial thermal resistance, a larger volume of fluid atoms was adsorbed on FWG surfaces than on patterned ones for the same percentage of hydrophilic-hydrophobic content, as illustrated in figure 5.22. In the non-equilibrium process, with the elevation of the temperature of the bottom surface, large volumes of fluid atoms start to condense on the top surface after being evaporated from the bottom one. The total amount of condensed fluid atoms is increased as the fraction of hydrophilic atoms in FWG and patterned surfaces increases. Under the same amount of hydrophilic-hydrophobic proportion, FWG surfaces appear to have a larger amount of condensed fluid atoms than patterned surfaces. The difference in the total number of condensed atoms between FWG and patterned is elevated in those cases with larger hydrophobic atoms' proportion, which obeys our analysis of section 5.3.3.

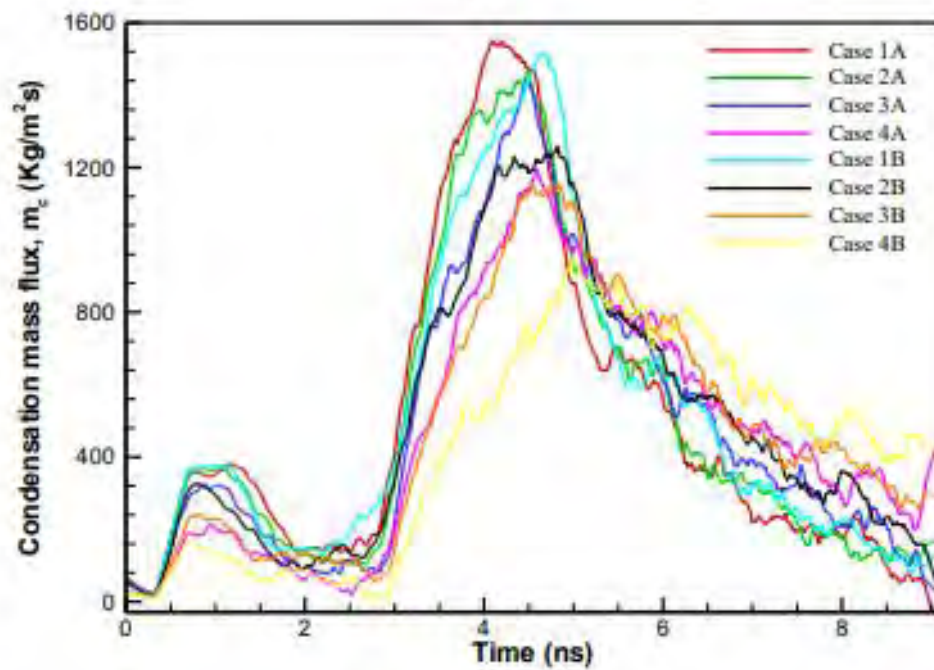
The instantaneous slope of figure 5.29 (a) is used to calculate the condensation mass flux, which represents the rate of condensation per unit surface area. Before the onset of the non-equilibrium period, the condensation mass flux ceased to nearly zero value, ensuring the propriety of the NVE ensemble. Then, following the initial dominant influence of solid-liquid interfacial thermal resistance, the condensation mass flux is elevated to its maximum value in the non-equilibrium session, demonstrating a gradual decrease in maximum mass flux of the condensate from case 1 to case 4. In all respective cases, the FWG surface offered a larger value of maximum condensation mass flux than the patterned one. With the progress of time, the condensate has started to grow and the thickness of the condensates' layer rises on the condensing surface. This results in a rise in bulk thermal resistance, that acts as the presiding factor in the latter part of the simulation [92]. In FWG surfaces, the spread of condensate film is greater than the patterned surfaces along the direction of the wettability gradient, specifically in cases with a higher fraction of hydrophobic atoms (see figure 5.23, figure 5.24, figure 5.26 and figure 5.27). Because of the nonuniformity of condensate on patterned surfaces, a portion of the condensing surface remains unoccupied by condensates. This allows the vapor atoms to dissipate the energy to the condensing surface directly without encountering higher bulk thermal resistance of the condensate compared to the respective cases of FWG surfaces. As a result, the condensation mass flux for patterned surfaces with increased hydrophobic content exceeds that of FWG surfaces in the final simulation time. To estimate the overall characteristics of the condensing surfaces, a time-average value of average condensation mass flux, $m_{c,avg}$ is determined as shown in figure 5.31. The results demonstrate features similar to maximum condensation mass flux showing an increase in $m_{c,avg}$ with the elevation of hydrophilic proportion and higher value of $m_{c,avg}$ in FWG surfaces than the patterned ones.

5.3.5 Heat flux characteristics at the condensing wall

Condensing wall heat flux, q_w , can be regarded as how much energy is dissipated by the fluid atoms while condensing on the surface. Higher wall heat flux makes the surface more conducive to condensation heat transfer. In figure 5.30, before the onset of the non-equilibrium period, q_w has ceased to almost zero, ensuring the appropriateness of thermal equilibrium. In the non-equilibrium period, with the large volume of condensation of fluid atoms, the graph of heat flux



(a)



(b)

Figure 5.29: Temporal variation of condensation characteristics in terms of (a) amount of condensed fluid atoms and (b) condensation mass flux.

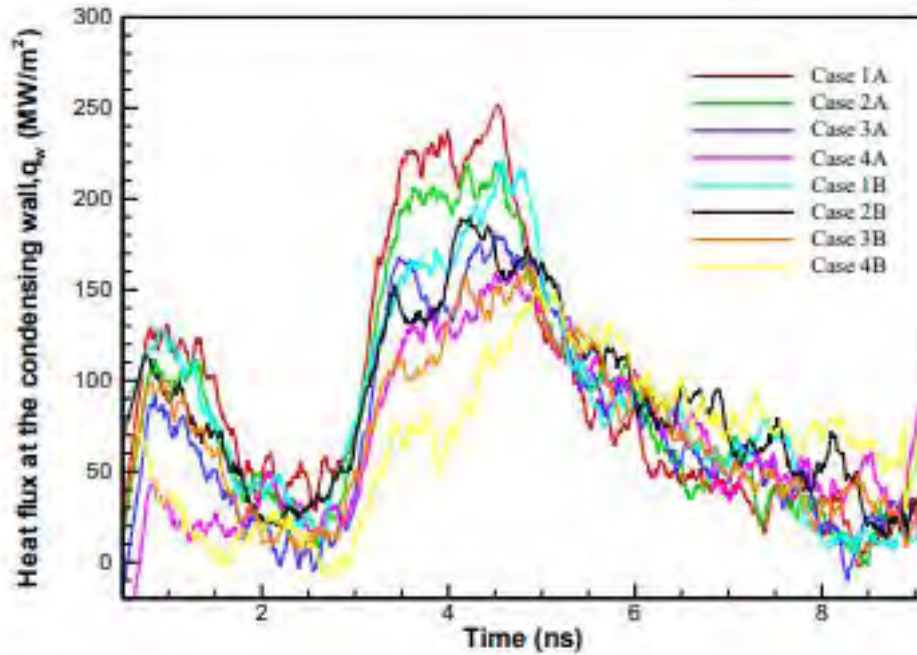


Figure 5.30: Temporal variation of heat flux at the condensing wall for different cases.

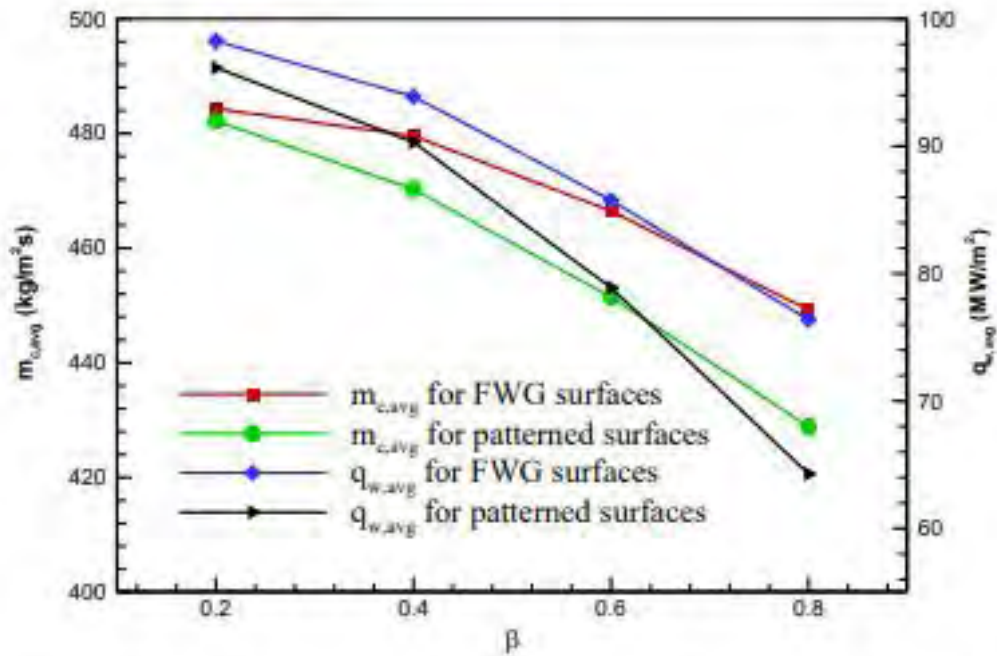


Figure 5.31: Average mass flux of the condensate and average condensing wall heat flux for different cases.

has achieved a sharp rise. Thus, the maximum value of q_w is attained after a short time interval. In this initial stage of condensation, solid-liquid interfacial thermal resistance was the preponderant factor of condensation [34,35,92]. As a result, surfaces with a larger hydrophilic proportion have reached a higher value of maximum condensing wall heat flux. From figure 5.22, it is perceived that solid-liquid interfacial thermal resistance is lower in FWG surfaces than in patterned surfaces in their respective cases. As a result, FWG surfaces attained a higher value of q_w than the patterned surfaces of their respective cases. With the increase in thickness of condensate, the bulk thermal resistance starts to increase, resulting in the decrement of q_w after attaining its maximum value. But in a patterned surface, some parts of the condensing surface remain unoccupied by the condensate at the latter stage, which has provided scope for fluid atoms to dissipate energy directly on the condensing surface. As a result, at a later stage, in the cases with higher content of hydrophobic atoms, the patterned surface has achieved a higher value of heat flux than the FWG surfaces.

To assess the overall heat flux characteristics of different condensing surfaces, an average value of condensing wall heat flux over the entire simulation time, $q_{w,avg}$ is evaluated for all cases. The results are plotted in figure 5.31. Figure 5.31 illustrates that the results follow our earlier pattern of maximum wall heat flux, showing an increment in the $q_{w,avg}$ with the rise in hydrophilic proportion, and $q_{w,avg}$ is larger in cases of FWG surfaces compared to the patterned ones.

5.3.6 Surface tension profile at the vicinity of condensing surface

To evaluate the spatial distribution of surface tension, the entire simulation system is split into 5933 planar segments of dimension $1 \text{ nm} \times 0.2895 \text{ nm}$ along the direction normal to the surface. Then Kirkwood's mechanical approach [123] is adopted for determining the surface tension, γ at each planar segment using the expression shown in equation (4.12). In a phase change process, the surface tension of a fluid achieves a finite value only at the liquid-vapor interface because of the equal amount of attraction by all atoms in the bulk vapor and liquid region [137]. Therefore, in figure 5.32, the region where surface tension has attained a finite value specifies the liquid-vapor interfacial region. The numerical value of surface tension shown in figure 5.32 conforms with the previous study of similar atomistic model [95]. The thickness of the interface also follows the findings of earlier researches [138,139]. The liquid-vapor interfacial area is spotted to rise with the elevation of hydrophilic proportion. Moreover, the liquid-vapor interfacial area is

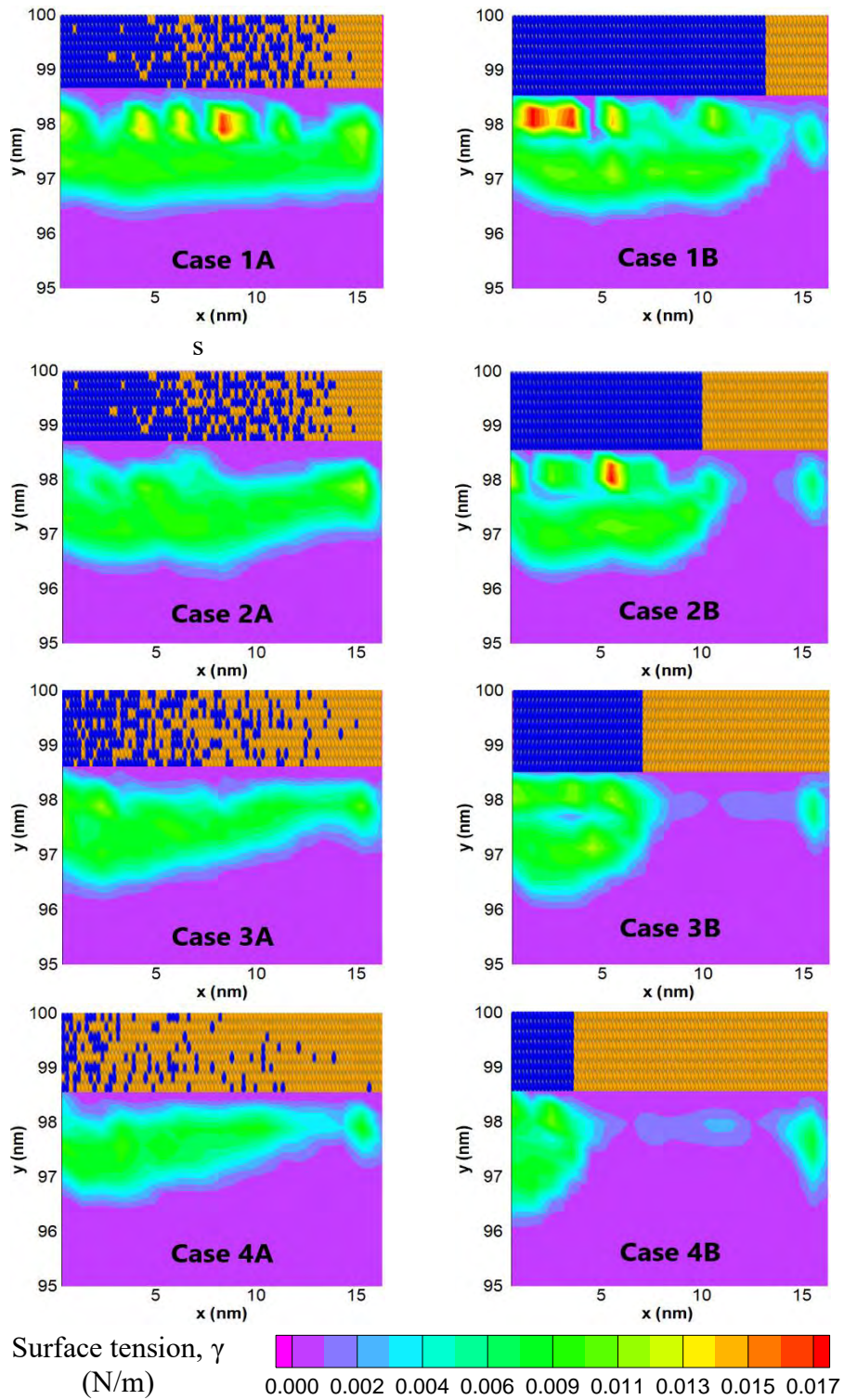


Figure 5.32: Liquid-vapor interfacial surface tension profile for different cases near the condensing surface at 4 ns.

larger in FWG surfaces than in patterned surfaces for the same amount of hydrophilic-hydrophobic proportion. Since a higher liquid-vapor interface is regarded to be conducive to phase change heat transfer [126,141], it can be stated that FWG surfaces will be more suitable than patterned surfaces in terms of condensation heat transfer.

5.4 Effect of wettability contrast

In this section, the condensation characteristics of a hybrid wetting surface for different wettability contrasts have been discussed to investigate the change in nucleation, coalescence, and growth of the condensate layer and its subsequent effect on the condensation heat transfer with the change in wettability of the philic-phobic region. Previously, Xu et al. [75] reported that the change in drainage of the condensate is associated with the change in wettability contrast of two different wetting regions. In this study, the wettability contrast between the atoms having different types of wetting characteristics and the fluid atoms is altered by altering the ratio of the solid-fluid interaction energy parameter to the fluid-fluid interaction energy parameter, namely, ϵ_r . For hydrophilic solid atoms, two different values of ϵ_r have been considered, i.e., $\epsilon_r = 2$ and 4, leading the atomistic wetting characteristics of the solid substrate from hydrophilic to superhydrophilic. On the other hand, for hydrophobic solid atoms, two different values of ϵ_r have been considered, i.e., $\epsilon_r = 0.5$ and 0.25, which lead to the atomistic wetting characteristics of the solid substrate changing from hydrophobic to superhydrophobic. From the combinations of the aforementioned values of ϵ_r , four different cases are considered in this section, as shown in table 5.3.

Table 5.3: Solid-fluid energy parameter for different cases of wettability contrast.

Case	$\epsilon_{Ar-pt,philic}$ (eV)	$\epsilon_{Ar-pt,phobic}$ (eV)
Case 1	0.0416 ($\epsilon_r = 4$)	0.0026 ($\epsilon_r = 0.25$)
Case 2	0.0416 ($\epsilon_r = 4$)	0.0052 ($\epsilon_r = 0.5$)
Case 3	0.0208 ($\epsilon_r = 2$)	0.0026 ($\epsilon_r = 0.25$)
Case 4	0.0208 ($\epsilon_r = 2$)	0.0052 ($\epsilon_r = 0.5$)

On the basis of the total fraction of hydrophilic-hydrophobic combination of hybrid wetting surfaces, two different surfaces are considered, which are further classified into group A and group B for FWG and patterned wetting configurations as shown in figure 5.33.

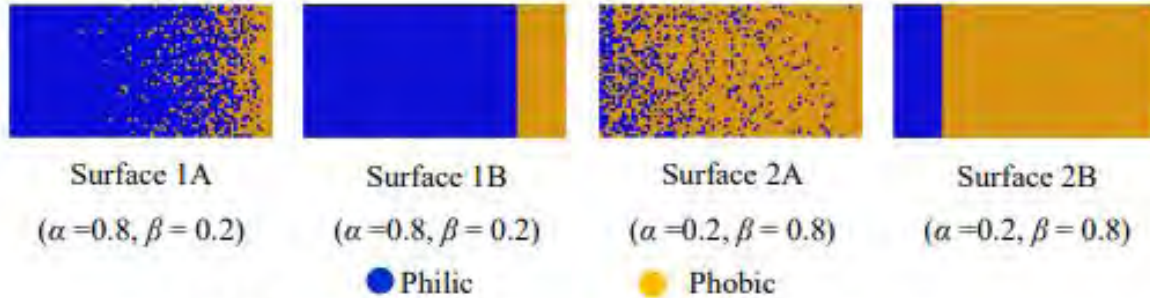


Figure 5.33: Wetting configuration of the different types of condensing surface.

5.4.1: System characteristics for different cases

Figure 5.34 and Figure 5.35 illustrate the temporal evolution of the total energy of fluid atoms for different cases considered in this section. The numerical value of the per atom total energy conforms with the earlier findings of similar atomistic systems [125]. From the constant value of total energy for all cases at the time interval 2–2.5 ns, it is quite evident that the entire system has achieved thermal equilibrium before the onset of the non-equilibrium period. Due to the elevation of the lower surface temperature to 130 K, argon atoms have been energized, which is noticed from figures 5.34 and 5.35. The energized atoms of the vapor phase has eventually started to condense on the top surface by dissipating heat to that one, resulting in a decrement of total energy. Thus, the lower value of total energy indicates a higher condensation rate as compared to the higher ones. Figure 5.34 depicts the total energy content of argon atoms at different timesteps for surfaces having a higher fraction of philic atoms, i.e., $\alpha = 0.8$. The results indicate that on both FWG and patterned surfaces, the total energy content of the argon atoms is lower in cases 1 and 2 than in cases 3 and 4 during the NEMD simulation. While comparing between cases 1 and 2, cases 3 and 4, it can be stated that the total energy content of the argon atoms is lower in case 2 than in case 1, and in case 4 than in case 3. Although the differences are minor due to the lower percentage of phobic atoms ($\beta = 0.2$) on surfaces 1A and 1B. On the other hand, figure 5.35 depicts the total energy content of argon atoms at different timesteps for surfaces having a lower fraction of phobic atoms, i.e., $\alpha = 0.2$. From figure 5.35, it is observed that the total energy of argon atoms is the lowest in case 1 on the surface with superhydrophilic and hydrophobic combinations, i.e., ($\epsilon_r = 4$

and 0.5) for both the FWG and patterned surface. Then the total energy is gradually increased in cases 2, 4, and 3 in figure 5.35 (a) for the FWG surface. This happens because in patterned surface the philic atoms are confined in a small region compared to the FWG ones.

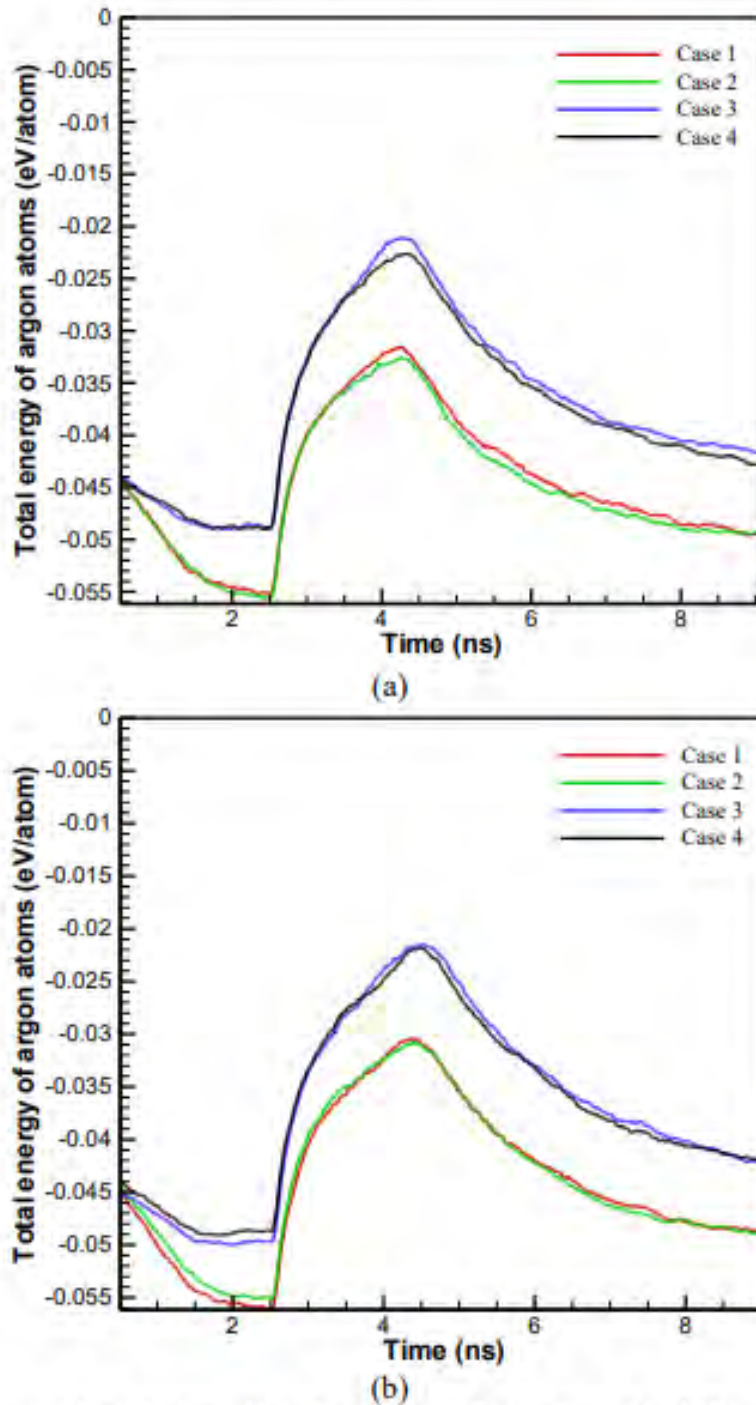
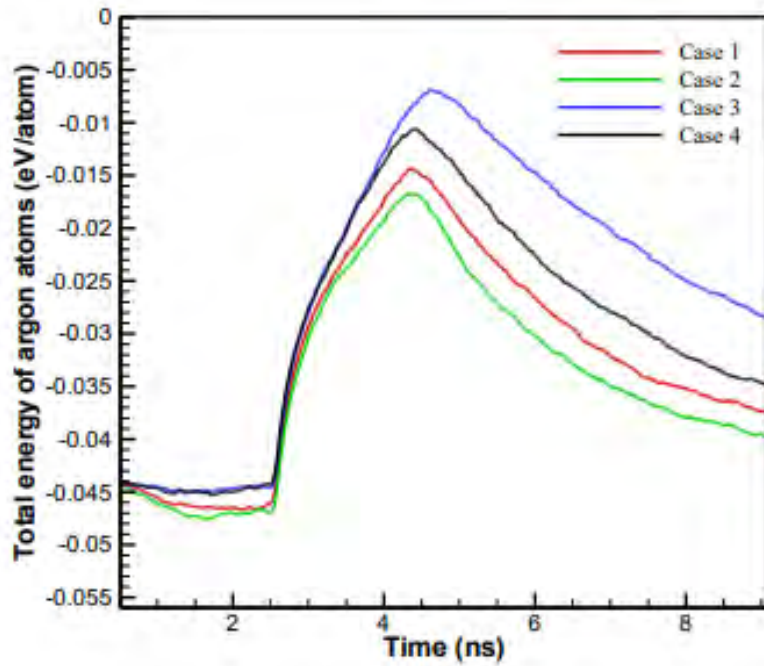
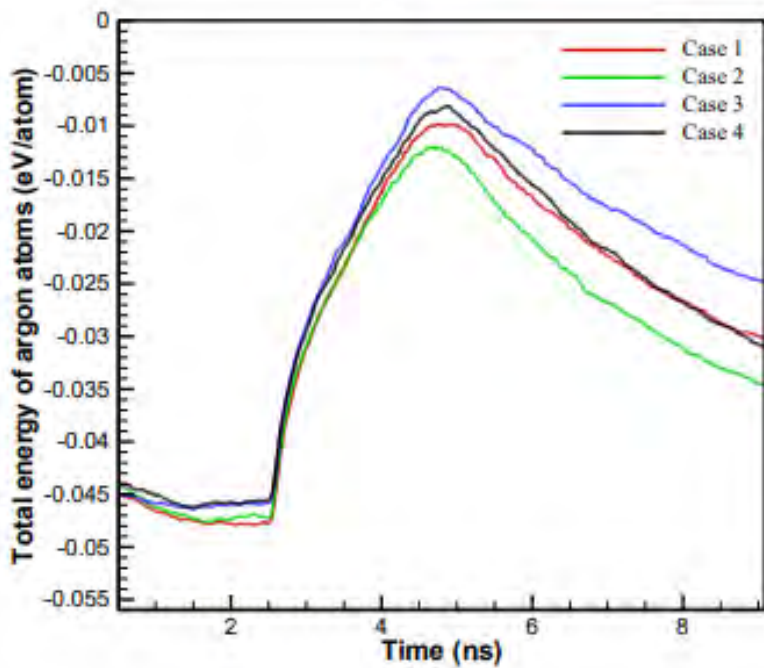


Figure 5.34: Temporal evolution of total energy of fluid atoms for different cases of (a) surface 1A and (b) surface 1B.



(a)



(b)

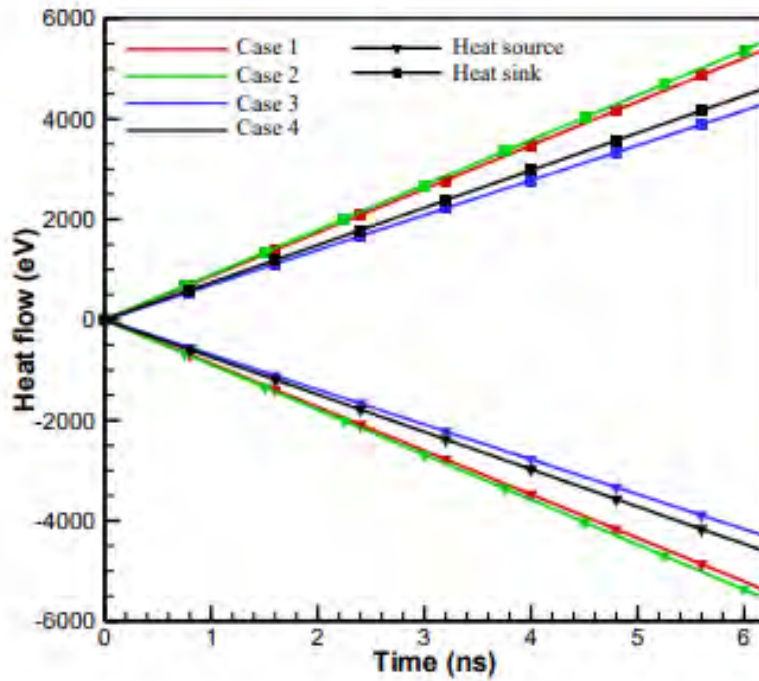
Figure 5.35: Temporal evolution of total energy of fluid atoms for different cases of (a) surface 2A and (b) surface 2B.

For this reason, in patterned surfaces with a smaller fraction of hydrophobic atoms, the effect of the wettability of the phobic atoms plays an important role in condensation after initial nucleation

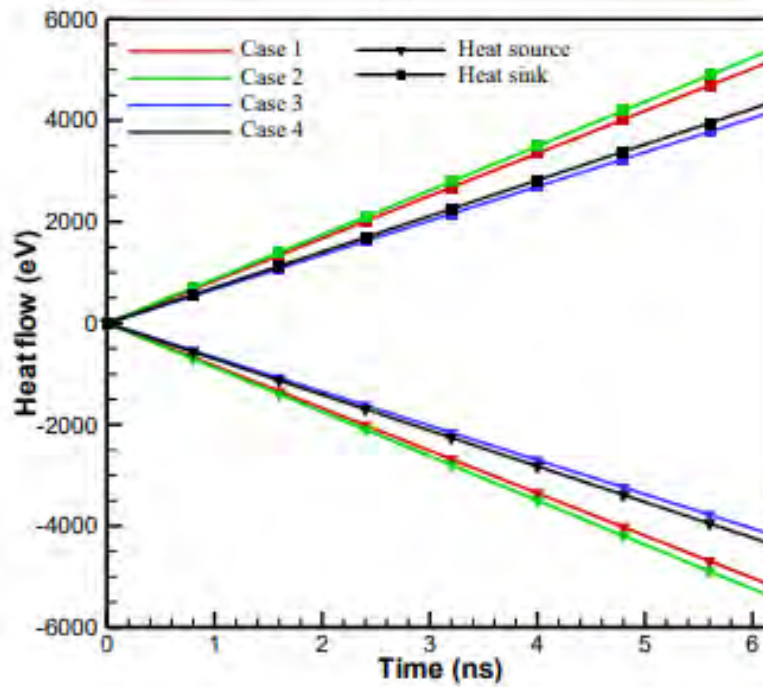
on the philic atoms. For this reason, in patterned surface higher condensation rate i.e., lower total energy of argon atoms is noticed in case 4 than case 2 and case 3 compared to the FWG surfaces.

5.4.2 Thermal resistance at the solid-liquid interface

To elucidate the condensation characteristics over different cases of hybrid wetting surfaces, solid-liquid interfacial thermal resistance, R_{int} is evaluated using equation (5.1) for a simulation domain as shown earlier in figure 5.7, following the methodology delineated in section 5.2.2. Under this atomistic configuration, the simulation is performed in an NVE ensemble by setting the temperatures of the source and sink at 130 K and 50 K, respectively, following an NVT ensemble of the whole system at 90 K. The simulation was conducted for 6.2 ns and the data was recorded after a timestep of 5 fs. The heat flow and spatial distribution temperatures shown in figures 5.36, 5.37, 5.38, and 5.39 follow the behavior of the earlier findings both qualitatively and quantitatively [126,127]. Solid-liquid interfacial thermal resistance, R_{int} , is calculated for different cases using equation (4.1), utilizing the simulation data q and ΔT from figures 5.36, 5.37, 5.38, and 5.39. The value of R_{int} plotted in figure 5.40 for different cases is in the same order of magnitude as the earlier findings [126–129]. From figure 5.40, it is noticed that the value of R_{int} is the lowest in case 2 (superhydrophilic-hydrophobic combination) than in the other cases on both surface 1A and surface 1B. Among the other cases, the value of R_{int} obeys the following order in terms of magnitude: Case 3 > Case 4 > Case 1. For surface 2A, it is observed that the numerical value of R_{int} follows the following trend: For Case 3 > Case 4 > Case 1 > Case 2. For surface 2B, the value of R_{int} shows the trend: Case 3 > Case 1 > Case 4 > Case 2 in terms of magnitude. The results of this section conform with the results of section 5.4.1, resulting in a lower value of total energy of argon atoms in cases with lower solid-liquid interfacial thermal resistance.

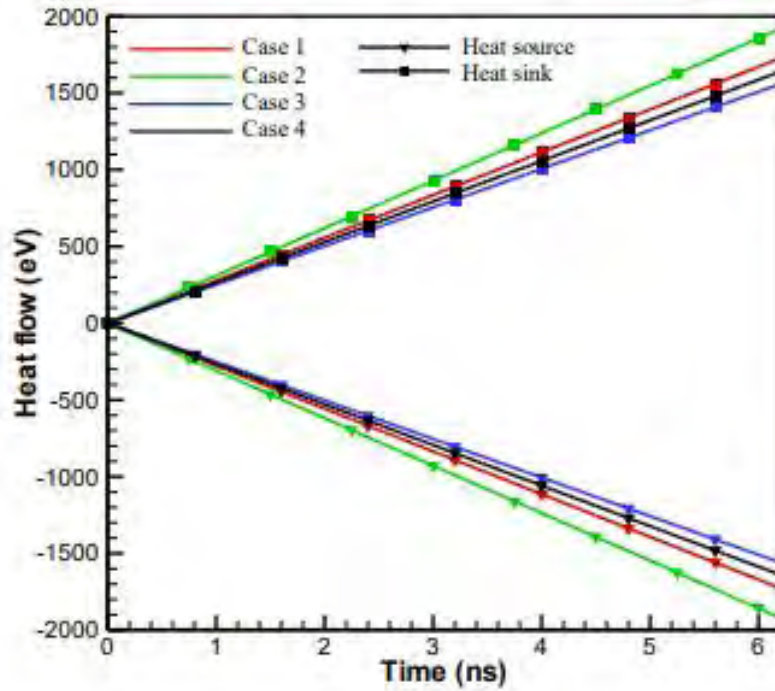


(a)

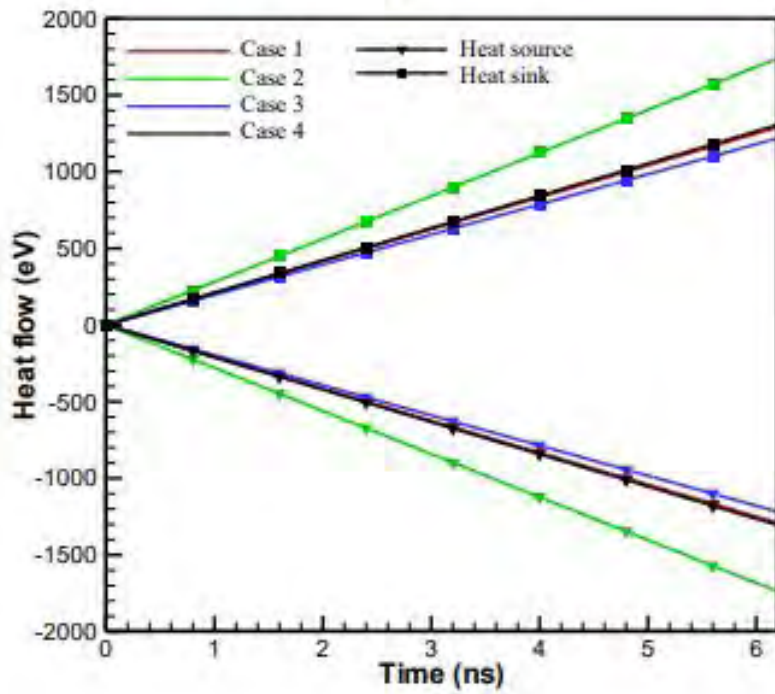


(b)

Figure 5.36: Temporal evolution of heat flow across source and sink for (a) surface 1A and (b) surface 1B.

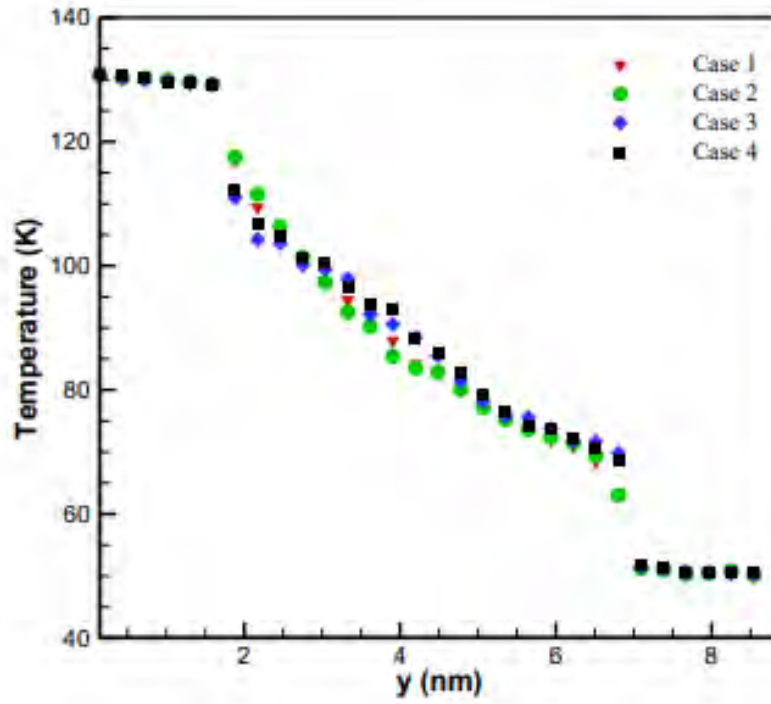


(a)

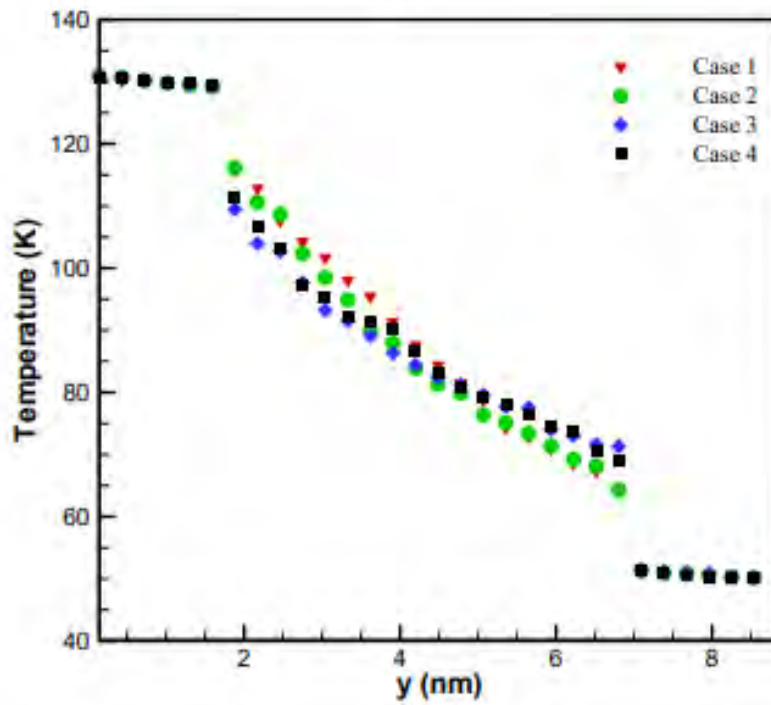


(b)

Figure 5.37: Temporal evolution of heat flow across source and sink for (a) surface 2A and (b) surface 2B.

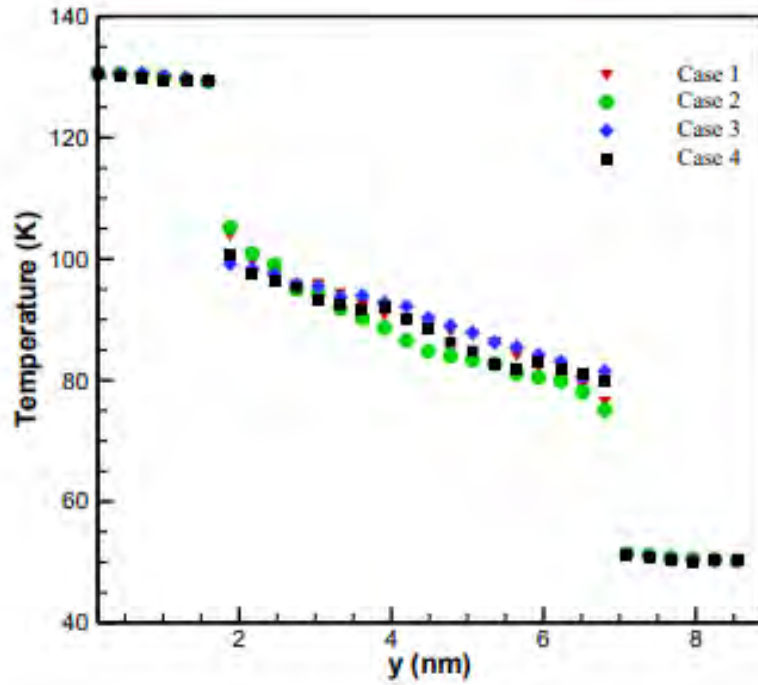


(a)

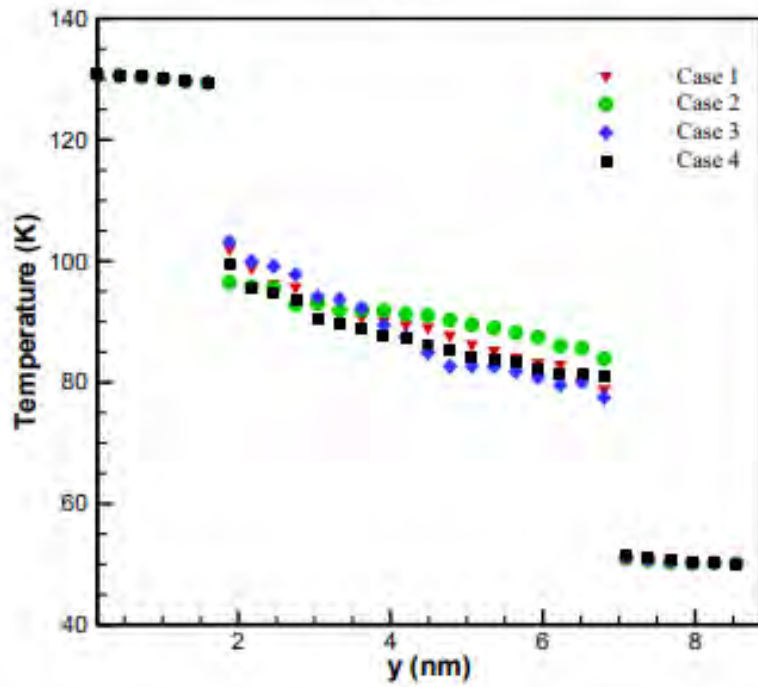


(b)

Figure 5.38: Spatial temperature distribution along y-axis for (a) surface 1A and (b) surface 1B.



(a)



(b)

Figure 5.39: Spatial temperature distribution along y-axis for (a) surface 2A and (b) surface 2B.

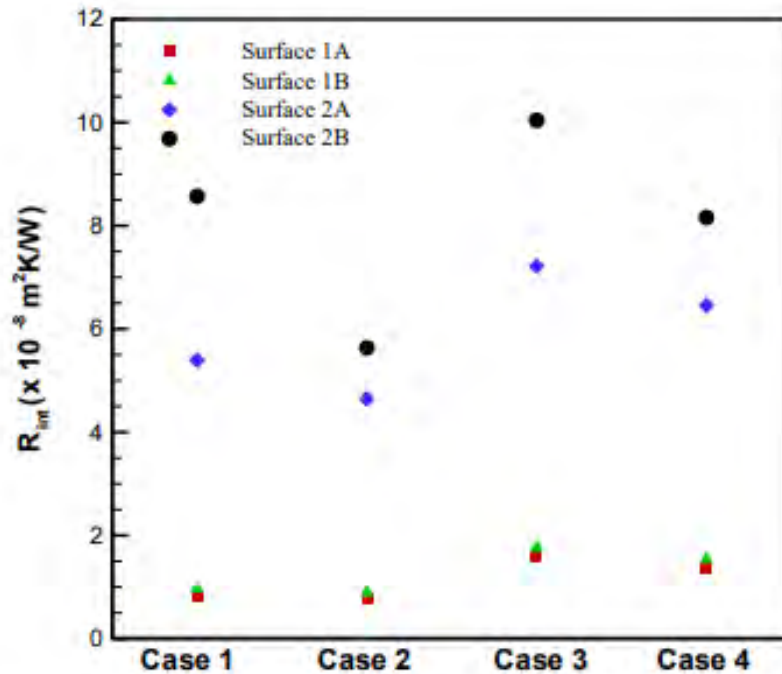
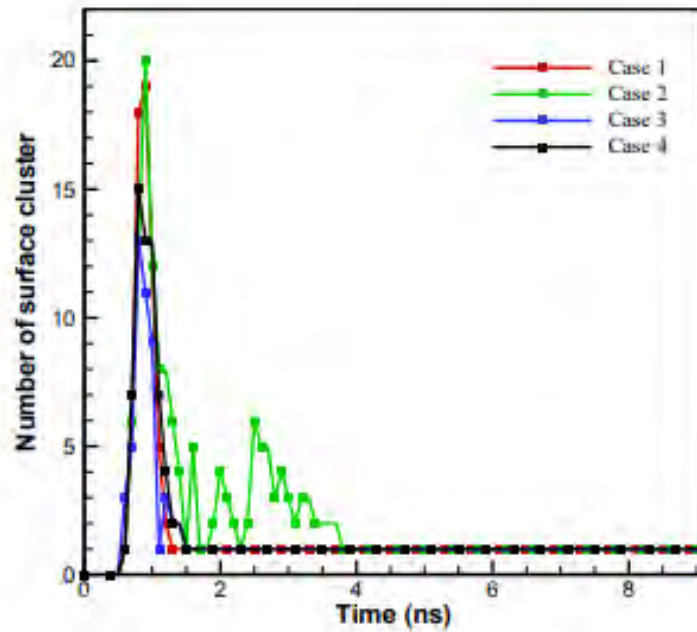


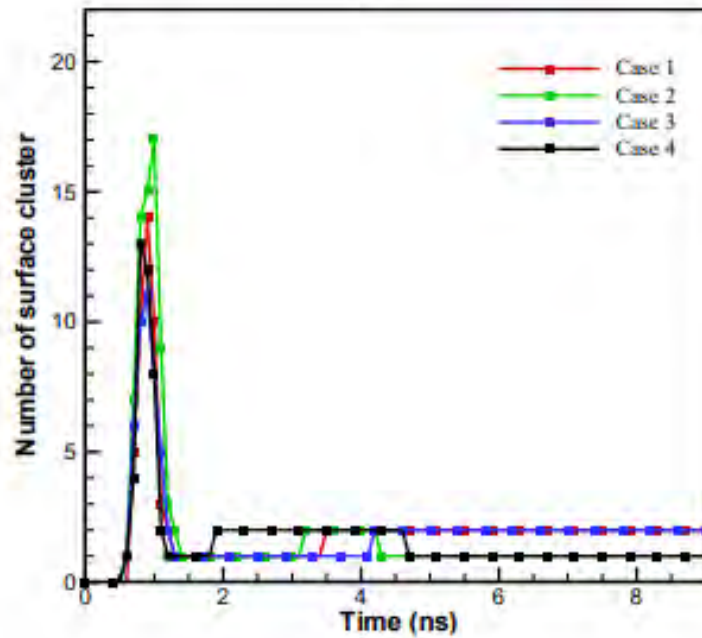
Figure 5.40: Solid-liquid interfacial thermal resistance, R_{int} for different cases of hybrid wetting surface

5.4.3 Nucleation, coalescence and growth characteristics for different cases

Figure 5.41 and Figure 5.42 depict the temporal variation of the number of surface clusters of the condensate formed during the condensation process for different cases of wettability contrast on the surfaces considered in this study. The number of surface clusters is determined in this section by following the definition of surface cluster as described in section 5.3.3. According to CNT, a free energy barrier, G^* , has to be surpassed to form a stable cluster. In section 5.3.3, it is described with necessary mathematical expression that, according to CNT, the value of G^* is reduced at a higher wetting surface, which eventually results in a higher rate of nucleation. For this reason, in this study, the maximum number of surface clusters is observed in case 2 during the initial period of condensation. In case 2, surfaces are comprised of atoms with superhydrophilic ($\epsilon_r = 4$) and hydrophobic ($\epsilon_r = 0.5$). The overall wettability in case 2 is greater than that of the other cases. As a result, the maximum number of surface clusters has been nucleated in this case. Among the other surfaces, the value of the maximum number of surface clusters has followed the following order: Case 2 > Case 4 > Case 3. For surface 1 with $\alpha = 0.8$, the philic atoms are dispersed over a large region along the length of the condensing surface. Particularly, on surface 1A, the philic atoms are dispersed along almost the entire length of the



(a)



(b)

Figure 5.41: Temporal variation of surface clusters for different cases of (a) surface 1A and (b) surface 1B.

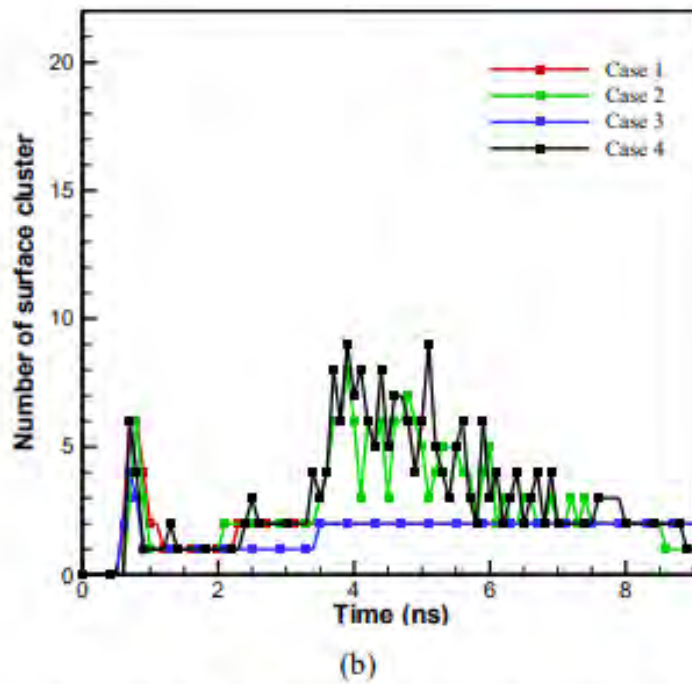
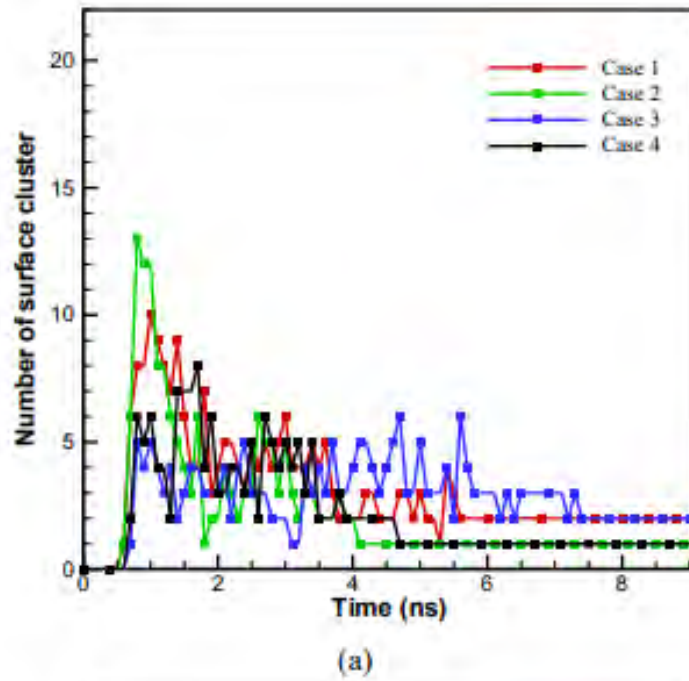


Figure 5.42: Temporal variation of surface clusters for different cases of (a) surface 2A and (b) surface 2B.

condensing surface (shown in figure 5.33), which has resulted in a complete film (number of surface clusters equal to 1) in all of the cases. A complete film was formed in cases 2 and 4 with surface 1B's patterned wetting configuration. But in cases 1 and 3, the formation of a complete

film has not been observed due to the low nucleation characteristics of the superhydrophobic atoms with $\epsilon_r = 0.25$ (shown in figure 5.44). Similar results were reported previously by Sheng et al. [64]. As shown in figure 5.33, the philic atoms are dispersed over a wide region on surface 2A when compared to surface 2B. For this reason, it is observed that on surface 2B, the nucleation sites are confined to a very small region of space. Since the region of atoms with $\epsilon_r = 0.25$ is widely dispersed in cases 1 and 3, the number of surface clusters is limited to 2 during the nonequilibrium period of the simulation after the initial coalescence after nucleation during the equilibrium period. On the other hand, in cases 2 and 4, a certain number of surface clusters coalesced and developed a complete film by the end of the simulation. On the other hand, for surface 2A, it is observed from figure 5.41 (a) that atoms continued to nucleate during the NEMD simulation after the initial nucleation and coalescence during the equilibrium period in all of the cases. This has happened due to the dispersion of philic atoms over a wide region, as shown in figure 5.33. After a certain period of time, the nucleated atoms coalesce into a complete film. This coalescence process has occurred quicker in case 2 due to its higher magnitude of overall wettability, which conforms with the findings of Pu et al. [73].

The wettability contrast of the hybrid wetting surface governs the growth mode of the condensate depending on the wetting profile of the surface. According to the classical theory of condensate growth mode, FM growth mode is expected to be observed on the surface with hydrophilic or superhydrophilic wettability due to the relatively higher attraction between solid and liquid than the liquid-liquid atom. For this reason, in figure 5.43, the FM growth mode is observed in all of the cases of surface 1A because of the wide dispersion of hydrophilic or superhydrophilic atoms along the length of the surface. On the other hand, depending on the wettability of the phobic atoms, different growth modes are observed on surface 1B in different cases considered in this study. On surface 1B, the dispersion of hydrophilic or superhydrophilic atoms is smaller than that on surface 1A. In addition, in cases 1 and 3, the wetting configuration of the phobic atoms follows $\epsilon_r = 0.25$, which causes the rate of nucleation to be very low in this region, as explained earlier in this section. For this reason, liquid atoms had a stronger tendency to condense over the philic region in cases 1 and 3 compared to cases 2 and 4. As a result, a liquid cluster of relatively large curvature following the shape of an island is noticed over the philic region in cases 1 and 3. A few atoms nucleated on the superhydrophobic region did not form a film but rather existed as

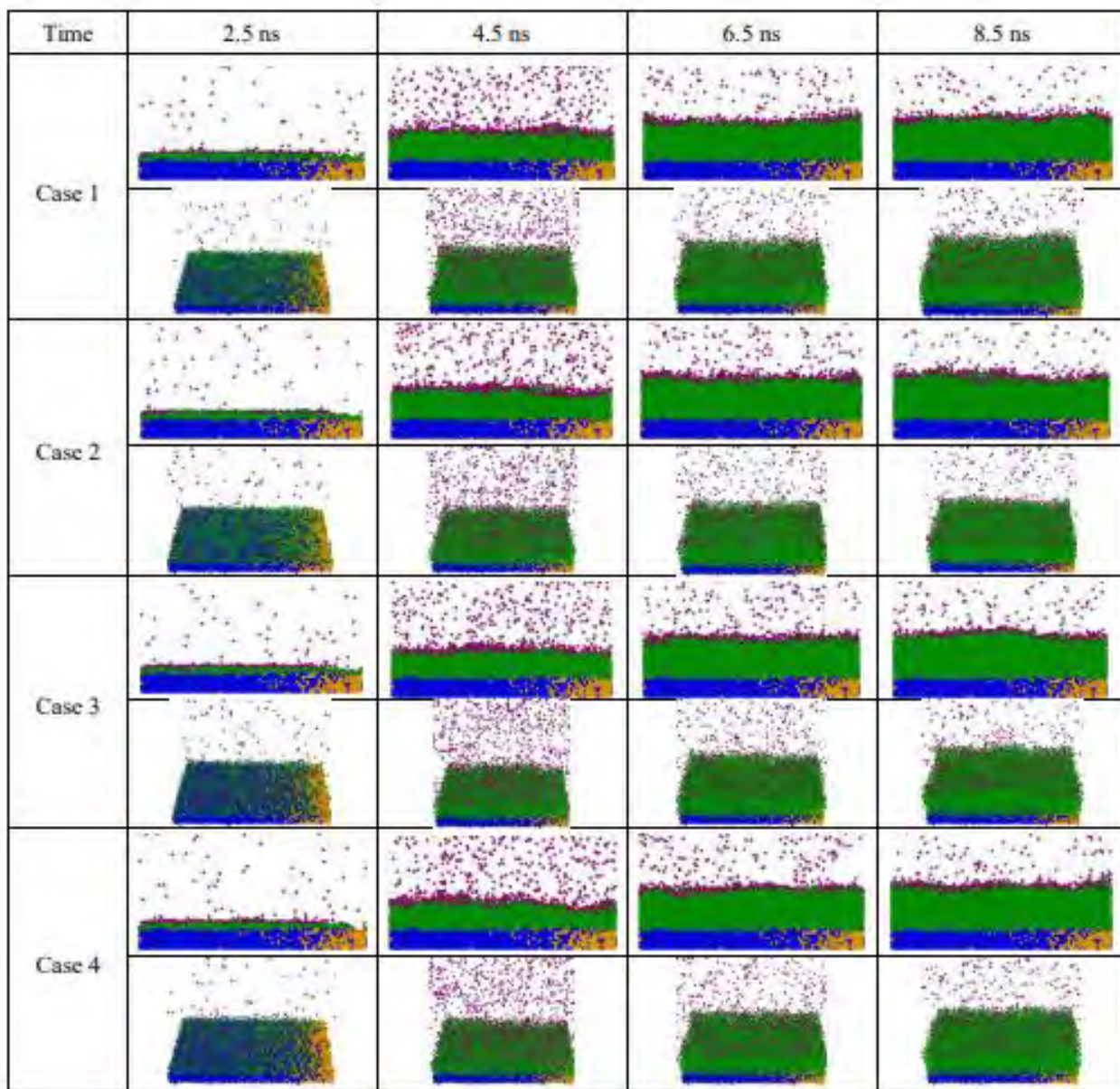


Figure 5.43: Snapshots of atomic trajectory at condensing surface for showing difference in nucleation and growth of liquid clusters of Argon atoms for different cases in surface 1A. Colors indicating- blue for hydrophilic region, orange for hydrophobic region, purple for vapor Ar atoms, green for liquid Ar atoms.

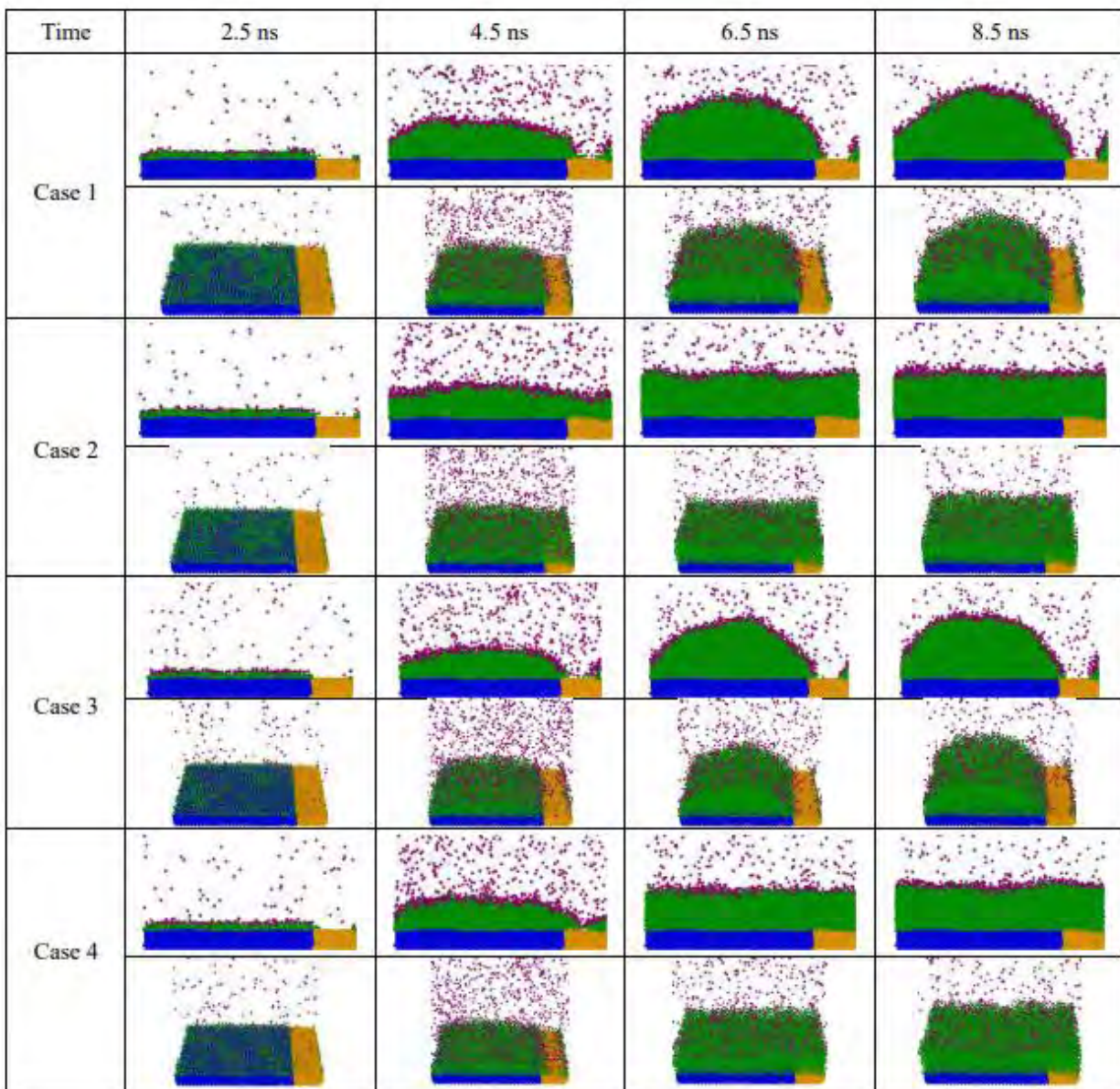


Figure 5.44: Snapshots of atomic trajectory at condensing surface for showing difference in nucleation and growth of liquid clusters of Argon atoms for different cases in surface 1B. Colors indicating- blue for hydrophilic region, orange for hydrophobic region, purple for vapor Ar atoms, green for liquid Ar atoms.

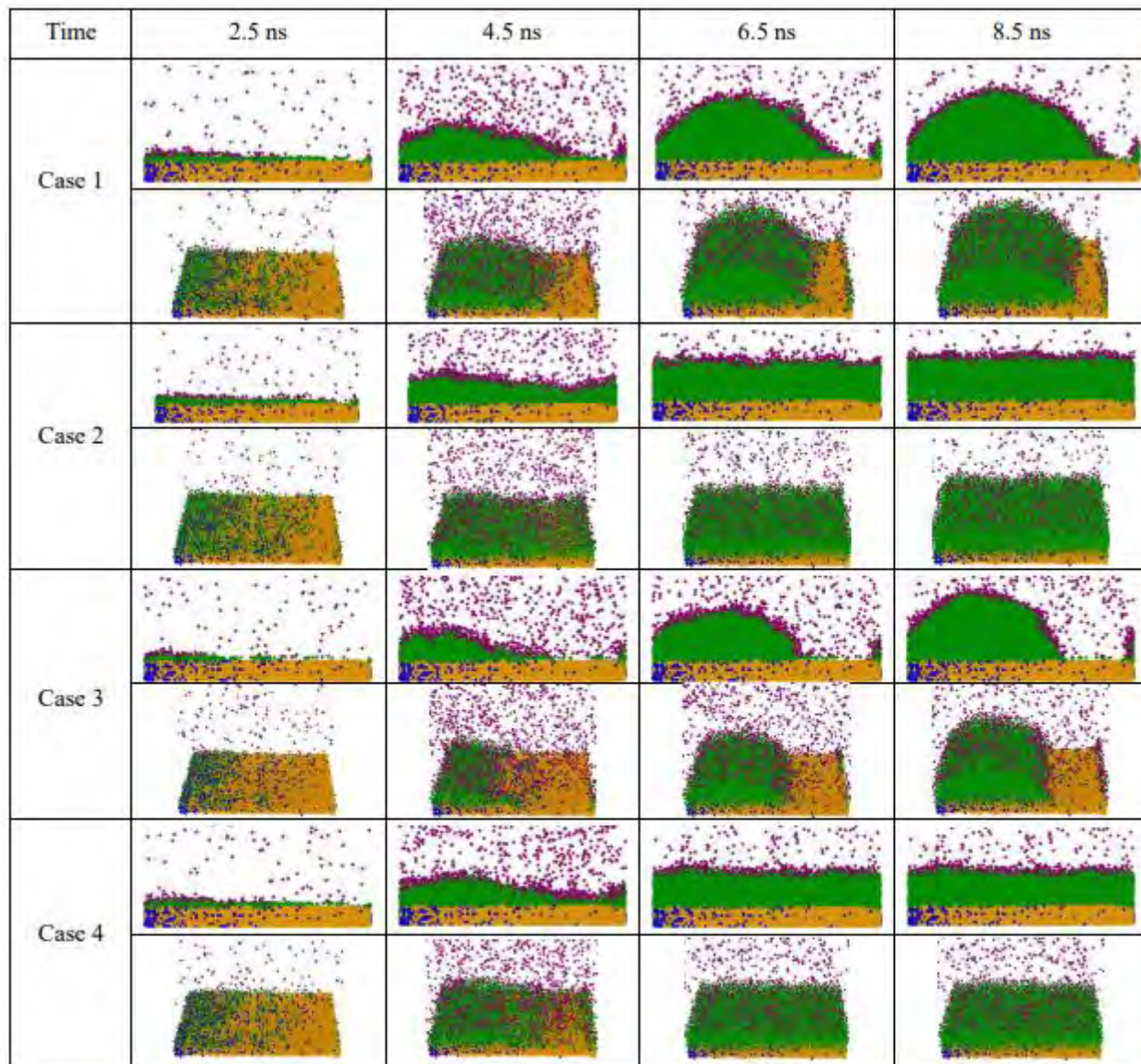


Figure 5.45: Snapshots of atomic trajectory at condensing surface for showing difference in nucleation and growth of liquid clusters of Argon atoms for different cases in surface 2A. Colors indicating- blue for hydrophilic region, orange for hydrophobic region, purple for vapor Ar atoms, green for liquid Ar atoms.

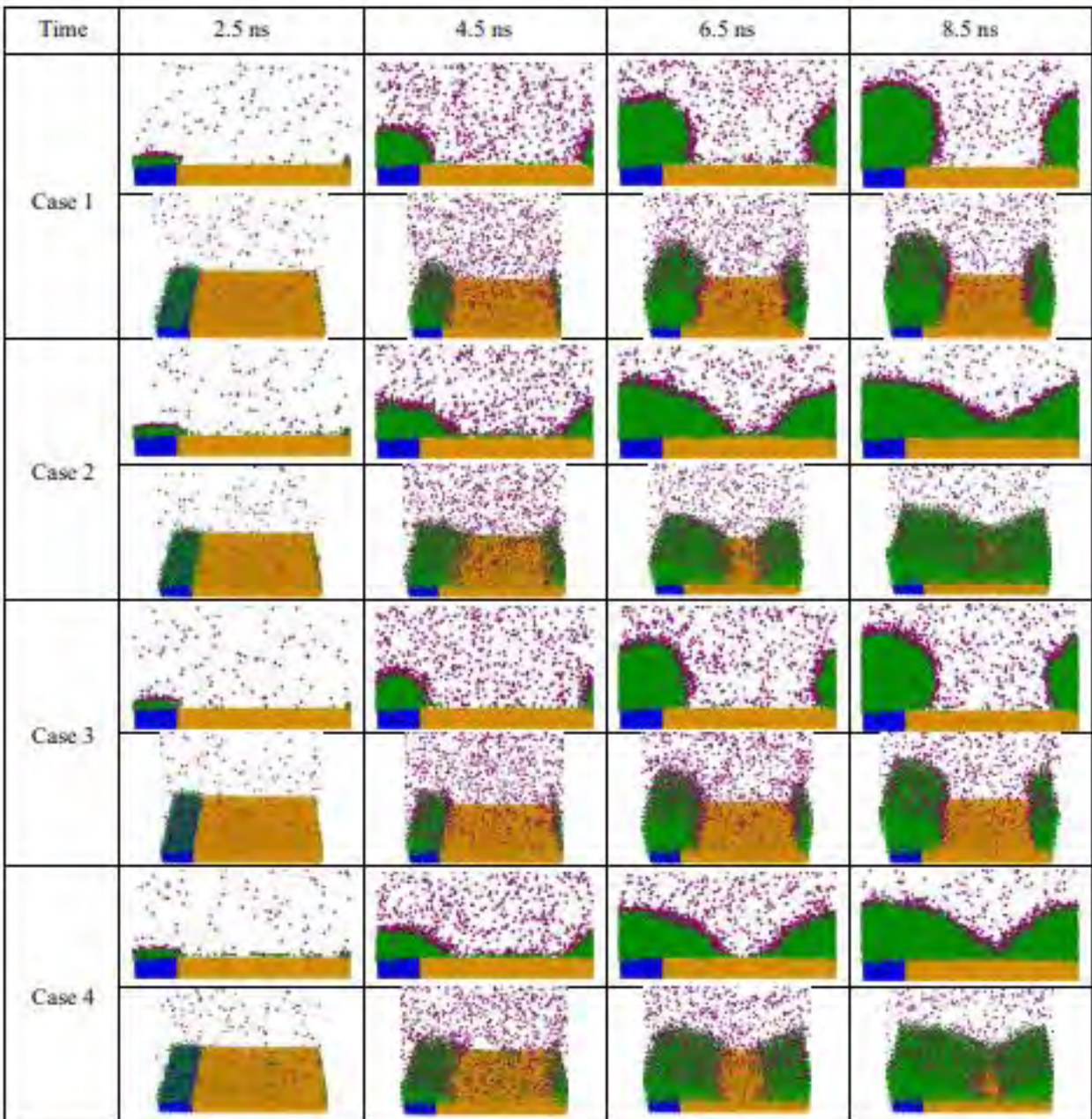


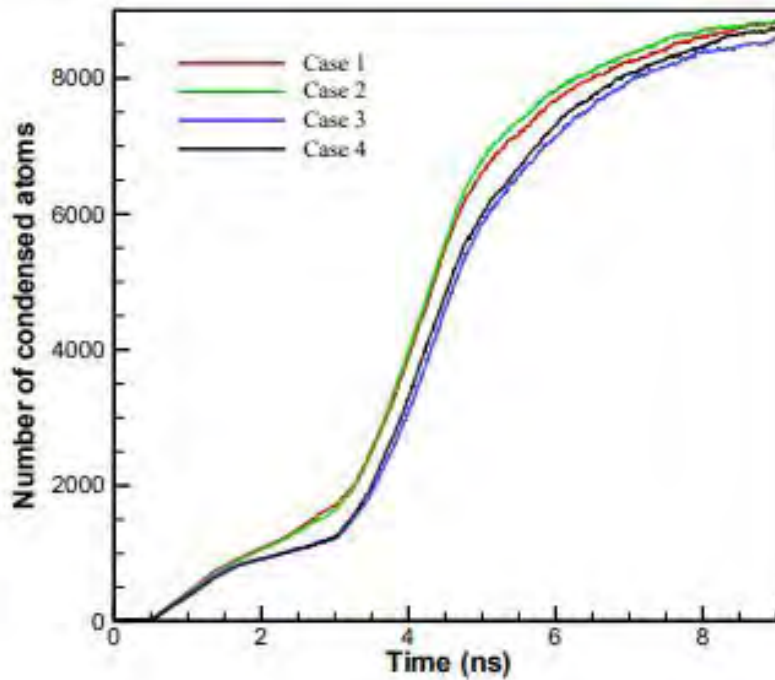
Figure 5.46: Snapshots of atomic trajectory at condensing surface for showing difference in nucleation and growth of liquid clusters of Argon atoms for different cases in surface 2B. Colors indicating- blue for hydrophilic region, orange for hydrophobic region, purple for vapor Ar atoms, green for liquid Ar atoms.

droplets, which is consistent with Sheng et al. [68]. On the other hand, for cases 2 and 4, relatively larger numbers of atoms were condensed on the hydrophobic region of the hybrid wetting surface

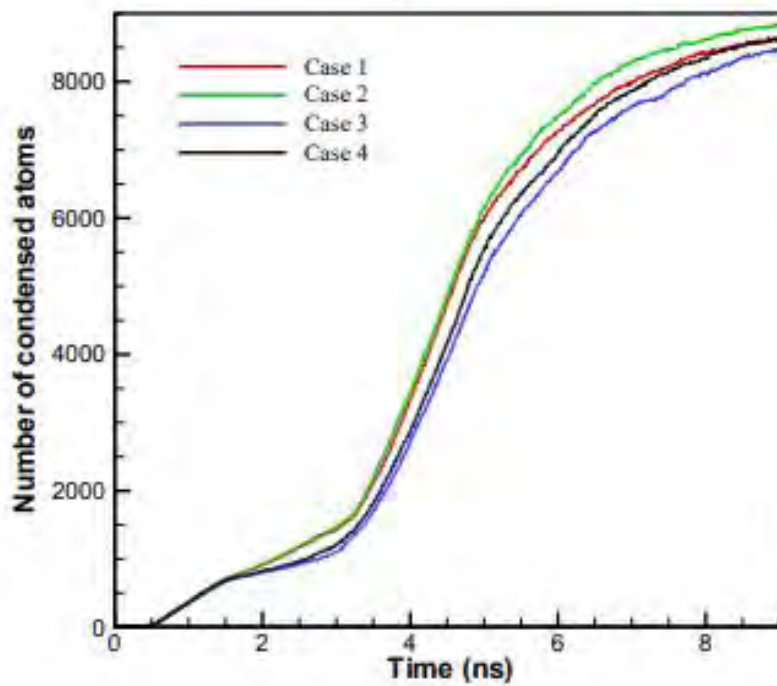
that eventually coalesced with the liquid cluster over the superhydrophilic or hydrophilic region and the growth of condensate followed the FM growth mode. In figure 5.45 for surface 2A, it is observed that the hydrophilic or superhydrophilic atoms are dispersed over a wide region along the length of the condensing surface. For this reason, the growth of the condensate is observed to follow the FM growth mode in cases 2 and 4. But in cases 1 and 3, very small numbers of atoms were condensed over the superhydrophobic region, which could not coalesce with the existing liquid cluster developed over the hydrophilic or superhydrophilic region, and the resulting growth of the condensate layer followed the VW growth mode. From figure 5.46 for surface 2B, two different islands were observed in the hydrophilic/superhydrophilic and superhydrophobic region. This happened because of the very large thickness of the condensate over the hydrophilic/superhydrophilic, which acted as a barrier for the vapor atoms to exchange energy with the solid substrate and change the phase from vapor to liquid [92]. On the other hand, in cases 1 and 3, the atoms condensed over the hydrophobic region coalesced due to their spontaneous transition from the low wetting region to the high wetting region [84,85]. For this region, an island of condensate layer is observed over the initial layer of condensate, which conforms to the SK growth mode.

5.4.4 Transient condensation over different hybrid wetting surfaces

To explain the transient condensation characteristics of surfaces, the number of condensed atoms and the condensation mass flux, m_c , have been calculated following the approach as discussed in section 5.2.4. The results are plotted in Figure 5.47, Figure 5.48, Figure 5.49, and Figure 5.50. From figures 5.47 and 5.48, it is observed that the highest number of atoms has been condensed in case 2 due to the largest magnitude of overall wettability. Among the other surfaces, on surface 1A and surface 1B, the total number of condensed atoms follows the following order: case 1 > case 4 > case 3. This result shows excellent agreement with the earlier analysis in sections 5.4.1, 5.4.2, and 5.4.3. From figures 5.48 (a) and (b), it is noticed that for surface 2A, the total number of condensed atoms follows the order case 2 > case 1 > case 4 > case 3 in terms of magnitude, whereas for surface 2B, the order is case 2 > case 4 > case 1 > case 3. In figure 5.33, it is shown that on surface 2A, the hydrophilic or superhydrophilic atoms are dispersed over a wide region compared to the surface 2B. For this reason, the wettability of the philic atoms

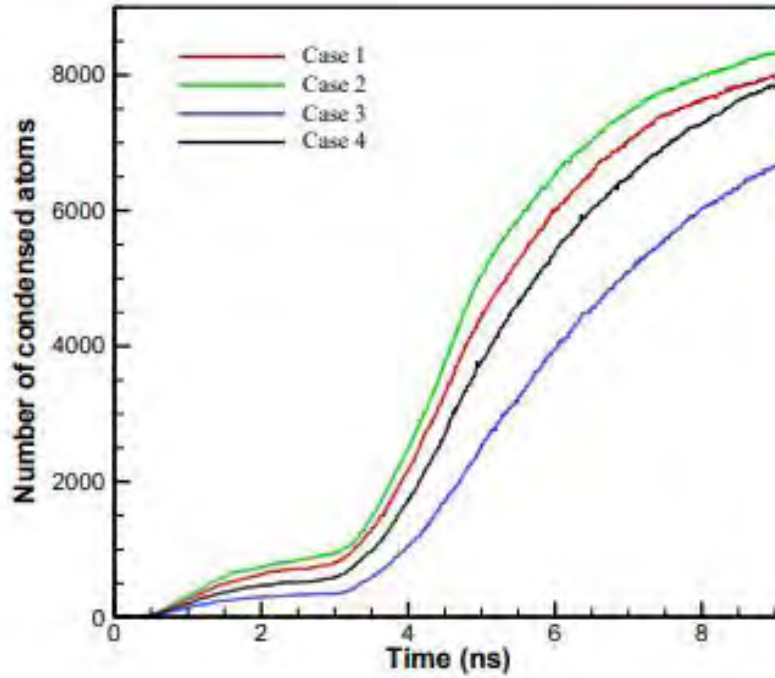


(a)

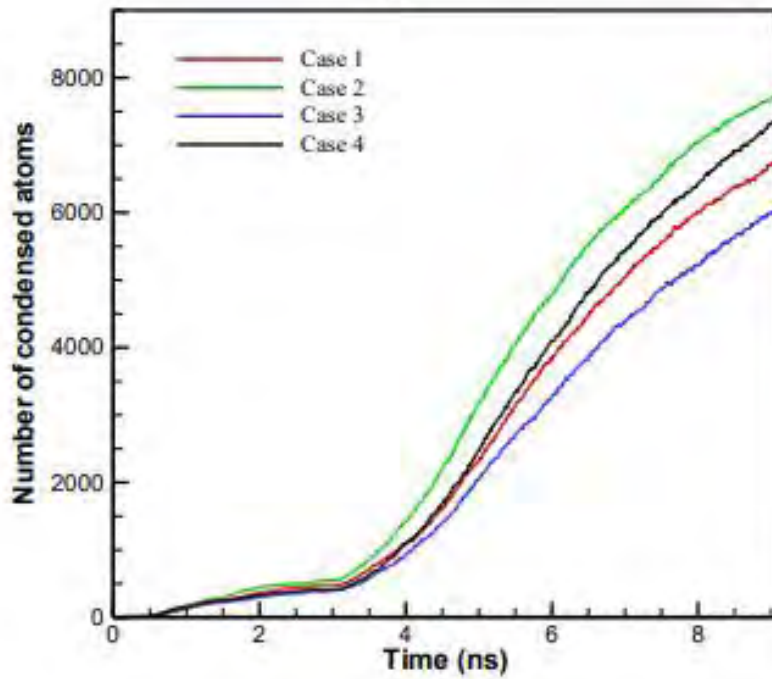


(b)

Figure 5.47: Temporal variation of number of condensed atoms for different cases of (a) surface 1A and (b) surface 1B.

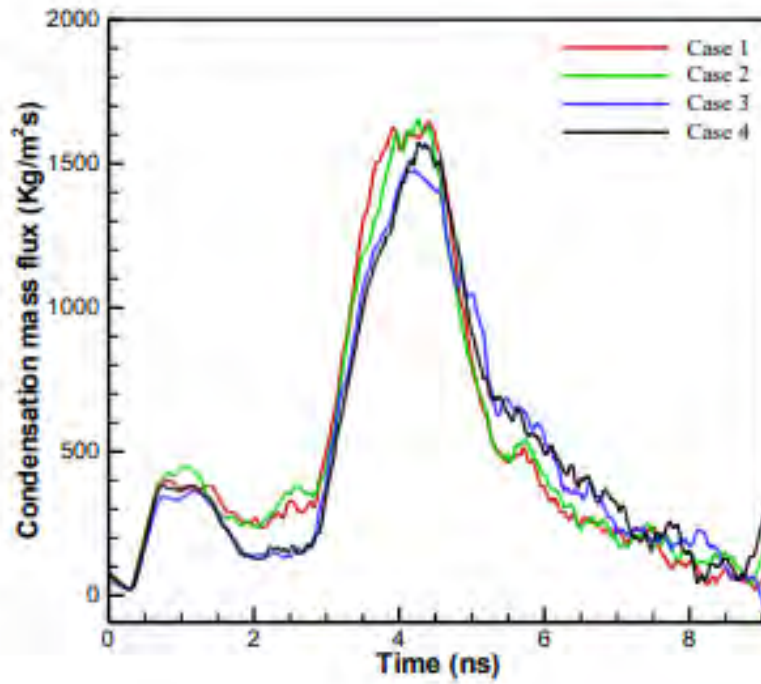


(a)

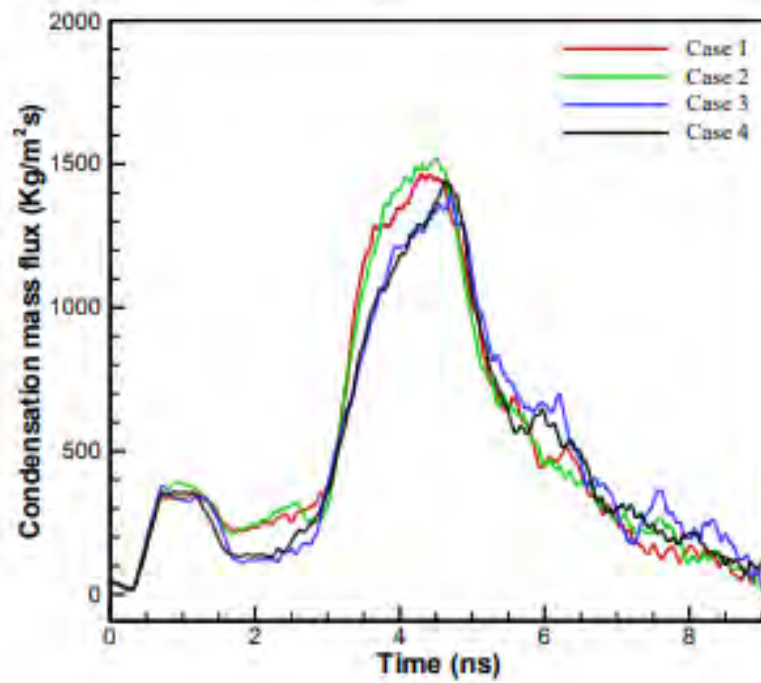


(b)

Figure 5.48: Temporal variation of number of condensed atoms for different cases of (a) surface 2A and (b) surface 2B.

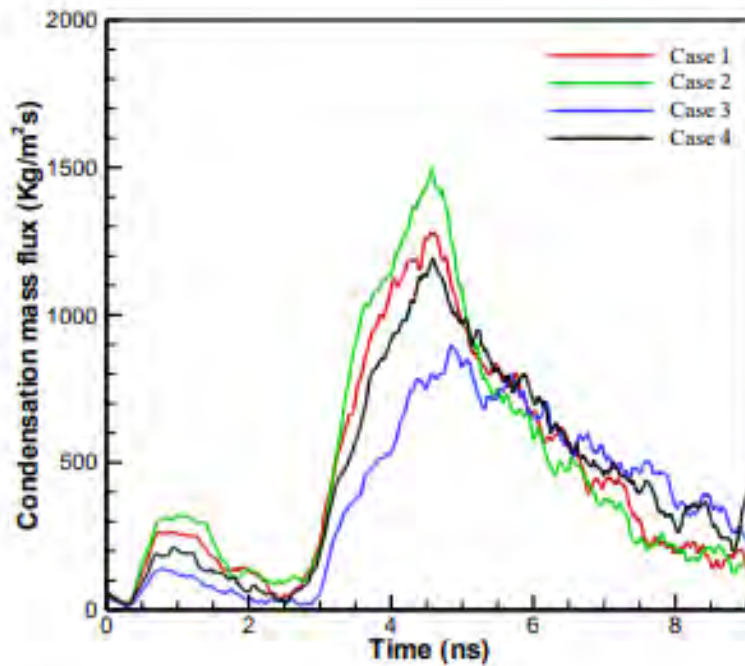


(a)

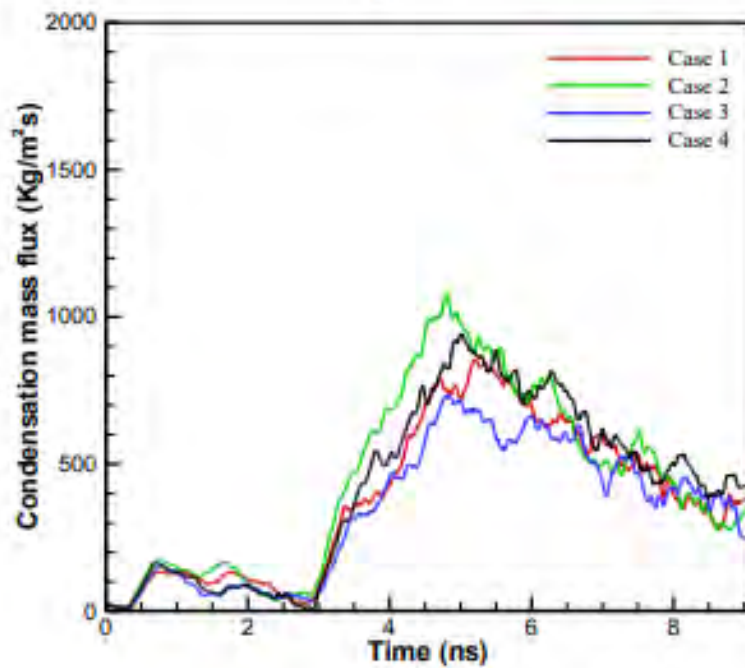


(b)

Figure 5.49: Temporal variation of condensation mass flux, m_c for different cases of (a) surface 1A and (b) surface 1B.



(a)



(b)

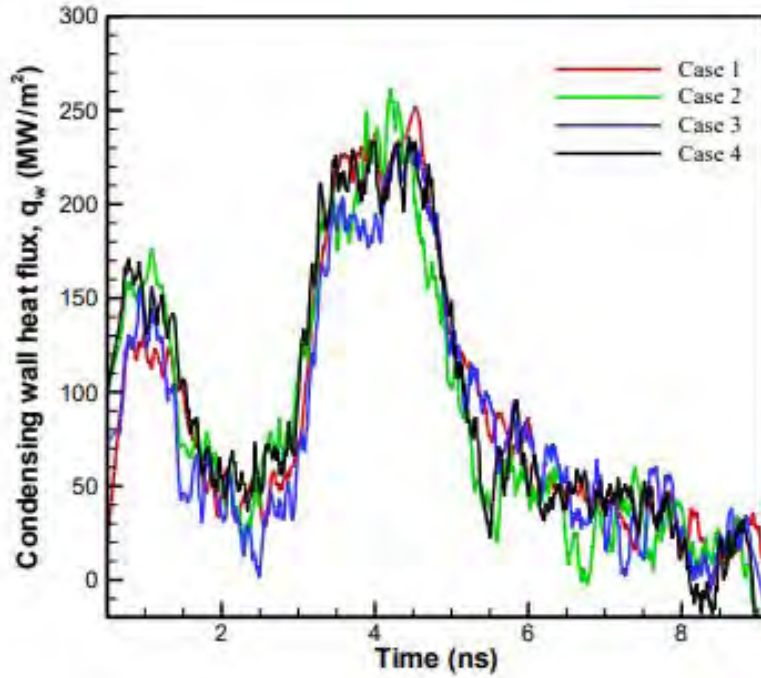
Figure 5.50: Temporal variation of condensation mass flux, m_c for different cases of (a) surface 2A and (b) surface 2B.

played an important role rather than the phobic atoms in surface 2A. For this reason, case 1 has offered a higher number of condensed atoms than case 4 on surface 2A compared to surface 2B.

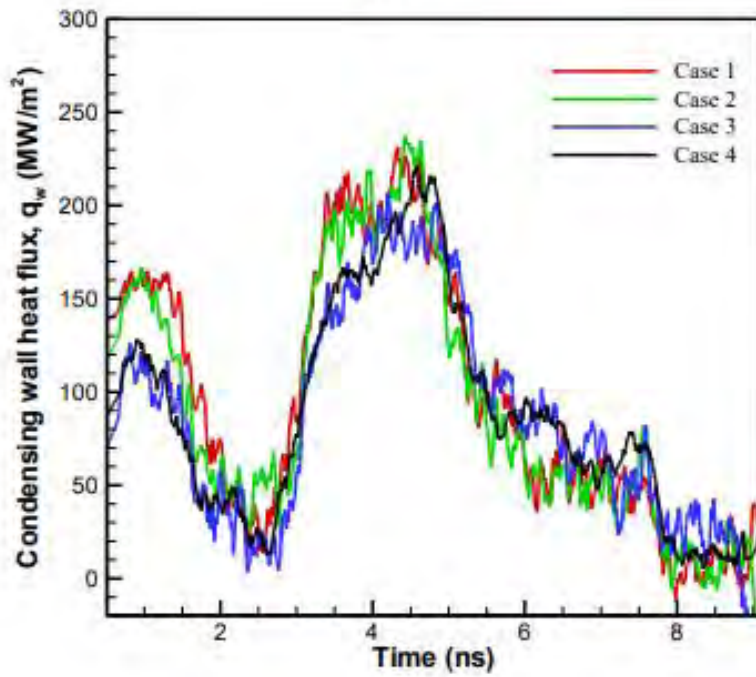
Figure 5.49 and Figure 5.50 illustrate the temporal variation of condensation mass flux, m_c , for different cases. It is observed from figure 5.49 (a) that case 2 has attained the highest magnitude of maximum value of condensation mass flux than the other cases due to its highest value of overall wettability, which results in the lowest solid-liquid interfacial thermal resistance among all the cases. Because of the wide dispersion of philic atoms along the length of surface 1A, the effect of the wettability of phobic atoms has not been significant on surface 1A between cases 1 and 2. As a result, the difference between cases 1 and 2 is not significant in terms of the maximum value of condensation mass flux. Because of the wide dispersion of philic atoms along the length of surface 1A, the effect of the wettability of phobic atoms has not been significant on surface 1A between cases 1 and 2. The maximum value of condensation mass flux is higher in case 4 than in case 3 due to the higher wettability of the condensing surface. Similar characteristics are observed in surface 1B, but the effect of the wettability of phobic atoms is more prominent than in surface 1A. In surface 2 with a $\alpha = 0.2$, the maximum value of condensation mass flux is the highest in case 2 for both FWG and patterned surface wetting configuration. On surface 2B, case 4 attains the highest value after case 2 due to the confined region of hydrophilic atoms in the patterned surface. As a result, on surface 2B, the wettability of phobic atoms has played a more important role than on surface 2A. The behavior of condensation mass flux in various cases is consistent with the earlier sections' analysis.

5.4.5 Heat flux characteristics at the condensing wall

The condensing wall heat flux for different cases at various surface configurations is calculated using the approach described in section 5.2.4. The numerical value of heat flux depicted in figures 5.51 and 5.52 is in the same order of magnitude as Liang et al. [135]. The characteristics of heat flux at the condensing wall follow the order of case 2 > case 1 > case 4 > case 1 in terms of the magnitude of maximum condensing wall heat flux for surfaces 1A, 1B, and 2A, which is in good agreement with the earlier characteristics of condensation mass flux. But, for surface 2B, the phobic atoms are confined to a very limited region compared to other surface configurations, which has helped case 4 attain a value of maximum condensing wall heat flux higher than case 1 due to the influence of wettability in the phobic region.

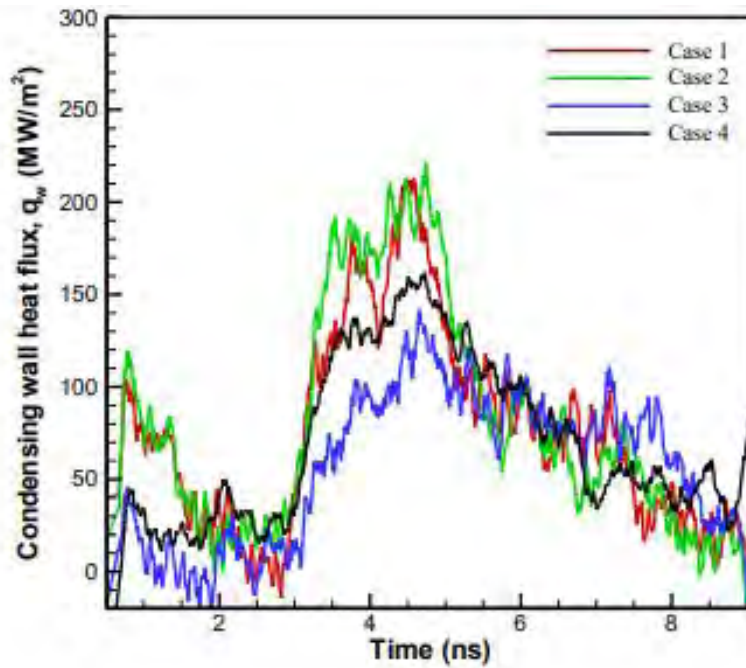


(a)

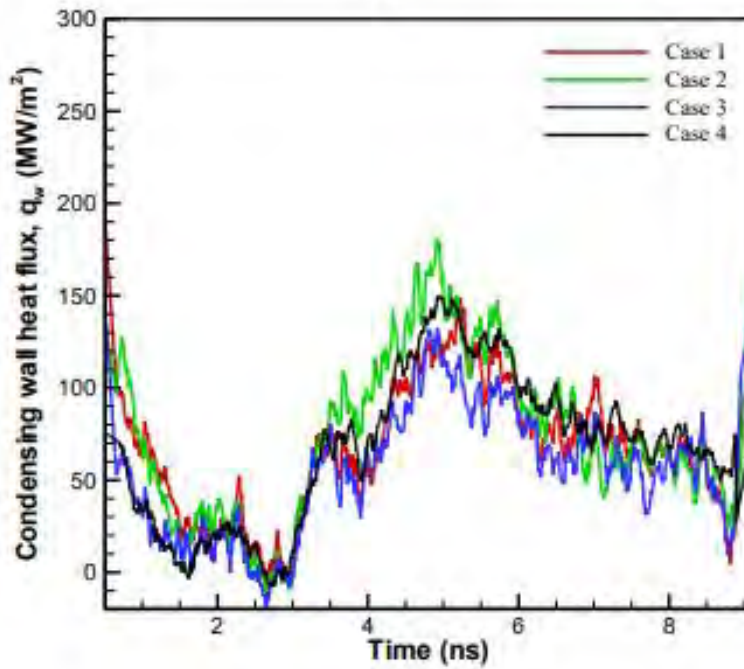


(b)

Figure 5.51: Temporal variation of condensing wall heat flux, q_w for different cases of (a) surface 1A and (b) surface 1B.



(a)



(b)

Figure 5.52: Temporal variation of condensing wall heat flux, q_w for different cases of (a) surface 2A and (b) surface 2B.

5.4.6 Time-averaged condensation characteristics

To estimate the overall performance of the condensation process during the entire period of simulation, the time-averaged value of condensation mass flux and condensing wall heat flux have been calculated, which are depicted in figure 5.53 for different cases at various surfaces. From figure 5.53, it is observed that the average value of condensation mass flux and condensing wall heat flux is the highest in case 2 for all of the surfaces. Among other cases, the average value of condensation mass flux and condensing wall heat flux follows the order case 1 > case 4 > case 3 for surface 1A, surface 1B, and surface 2A in terms of higher magnitude, and for surface 2B, the order is case 4 > case 1 > case 3. The results plotted in the figure conform qualitatively with the earlier analysis.

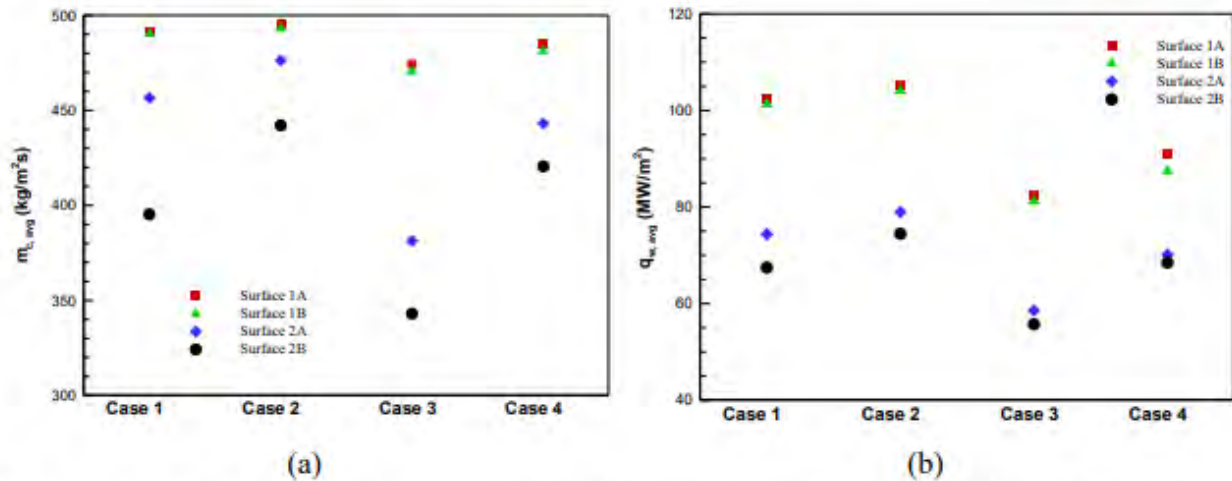


Figure 5.53: Variation of (a) average condensation mass flux, $m_{c,avg}$ and (b) average condensing wall heat flux, $q_{w,avg}$ for different cases of hybrid wetting surface.

In this research, the wetting configuration of the condensing surface has been varied under a uniform evaporating condition ensured by the unchanged hydrophilic wetting condition of the bottom surface. Two different types of wetting profiles are modeled on the upper surface, namely, gradient and patterned wetting profiles. Between them, functional wettability gradient (FWG) surfaces have been modeled by utilizing the power-law function from the notion of functionally graded material (FGM), whereas patterned wetting surfaces are modeled by juxtaposing the regions of different wettability. The performance of gradient and patterned wetting surfaces has been compared under an identical hydrophilic-hydrophobic fraction. The effect of hydrophilic proportion and hydrophilic-hydrophobic patterning on nanoscale condensation process has been assessed. Four different cases of wettability contrast surfaces i.e., superhydrophilic-superhydrophobic, superhydrophilic-hydrophobic, hydrophilic-superhydrophobic and hydrophilic-hydrophobic combinations have been modelled for determining the performance of hybrid wetting surface at different wettability contrast. The condensation characteristics of different surfaces have been reported with important parameters such as nucleation, coalescence and growth of the condensate, solid-liquid interfacial thermal resistance, number of condensed atoms, condensation mass flux, condensing wall heat flux, and surface tension profile. The key outcomes of the current study are as follows:

- i) Condensation process at nanoscale has been enhanced with the increment of hydrophilic fraction of hybrid wetting surface in both FWG and patterned hybrid wetting surface when the fraction of hydrophilic atoms has increased from 0.2 to 0.8. The rate of increment has been more significant in patterned surface than the FWG surface.
- ii) The gradient wetting surfaces are found to be superior in case of enhancement of condensation heat transfer over hybrid wetting surface than the patterned ones for an identical fraction of hydrophilic-hydrophobic combination. The disparity of condensation performance between these two different types of wetting profile has been widened when the fraction of hydrophobic atoms is higher.

- iii) In the cases of patterned surface, it has been detected that smaller strip size of hydrophilic-hydrophobic patterning works in favor of enhancement of condensation heat transfer.
- iv) The nucleation, coalescence and growth of condensate layer over different types of homogeneous and hybrid wetting surfaces has been in excellent agreement with the classical nucleation theory and classical theory of growth mode.
- v) In case of hydrophobic surface, the growth mode has followed the classical VW growth mode. But with the increment of hydrophilic fraction, it has started to shift towards the classical FM growth mode. FM, SK and VW growth mode has been noticed in patterned surfaces with fraction of hydrophilic atoms equal to 0.8, 0.6 and 0.4, 0.2, respectively. Also, for the smaller strip size, it has followed the FM growth mode, and SK growth mode is observed for larger strip size.
- vi) The effect of wettability contrast is more prominent in case of hybrid wetting surfaces with larger fraction of hydrophobic atoms. It is reported that for FWG surfaces at larger proportion of hydrophobic atoms the wetting characteristics of the hydrophilic region has played the important role on condensation heat transfer enhancement due to wide dispersion of hydrophilic atoms. But, for patterned surfaces with higher fraction of hydrophobic atoms, the effect of wettability of phobic atoms has played the dominant role on condensation heat transfer.
- vii) FM growth mode is observed in all of the wettability contrast cases of FWG surfaces with total fraction of hydrophilic atoms equal to 0.8. But for patterned surfaces FM growth mode is observed when the phobic atom has a value of $\epsilon_r = 0.5$. At surfaces with fraction of hydrophilic atoms equal to 0.2, the growth mode of the condensate has followed VW growth mode for all cases with phobic atoms having a value of $\epsilon_r = 0.25$. Among all of the other cases, FM and SK growth mode is noticed in FWG and patterned surfaces respectively. No condensate film has observed to be developed on hydrophobic region with low solid-liquid energy parameter ratio, i.e., $\epsilon_r = 0.25$.

REFERENCES

- [1] J.C. Love, L.A. Estroff, J.K. Kriebel, R.G. Nuzzo, G.M. Whitesides, Self-assembled monolayers of thiolates on metals as a form of nanotechnology, *Chem. Rev.* 105 (2005) 1103–1170.
- [2] H.G. Andrews, E.A. Eccles, W.C.E. Schofield, J.P.S. Badyal, Three-dimensional hierarchical structures for fog harvesting, *Langmuir*. 27 (2011) 3798–3802.
- [3] Y. Ghalavand, M.S. Hatamipour, A. Rahimi, A review on energy consumption of desalination processes, *Desalin. Water Treat.* 54 (2015) 1526–1541.
- [4] N. Ghaffour, T.M. Missimer, G.L. Amy, Technical review and evaluation of the economics of water desalination: current and future challenges for better water supply sustainability, *Desalination*. 309 (2013) 197–207.
- [5] J.W. Rose, Personal reflections on fifty years of condensation heat transfer research, *J. Enhanc. Heat Transf.* 22 (2015).
- [6] A.B. LITTLE, S. GARIMELLA, A review of ejector technology for refrigeration applications, *Int. J. Air-Conditioning Refrig.* 19 (2011) 1–15.
- [7] A.B. Little, S. Garimella, J.P. DiPrete, Combined effects of fluid selection and flow condensation on ejector operation in an ejector-based chiller, *Int. J. Refrig.* 69 (2016) 1–16.
- [8] Q. Zhao, D. Zhang, X. Zhu, D. Xu, Z. Lin, J. Lin, Industrial application of dropwise condensation, in: *Int. Heat Transf. Conf. Digit. Libr.*, Begel House Inc., 1990.
- [9] P. Zhang, F.Y. Lv, A review of the recent advances in superhydrophobic surfaces and the emerging energy-related applications, *Energy*. 82 (2015) 1068–1087.
- [10] L. Pérez-Lombard, J. Ortiz, C. Pout, A review on buildings energy consumption information, *Energy Build.* 40 (2008) 394–398.
- [11] I. Mudawar, Assessment of high-heat-flux thermal management schemes, *IEEE Trans. Components Packag. Technol.* 24 (2001) 122–141.
- [12] V.P. Carey, *Liquid Vapor Phase Change Phenomena: An Introduction to the Thermophysics of Vaporization and Condensation Processes in Heat Transfer Equipment*, Second Edition, Taylor & Francis, 2007.
- [13] D. Goldhaber-Gordon, M.S. Montemerlo, J.C. Love, G.J. Opiteck, J.C. Ellenbogen, Overview of nanoelectronic devices, *Proc. IEEE*. 85 (1997) 521–540.
- [14] A. Bar-Cohen, M. Arik, M. Ohadi, Direct liquid cooling of high flux micro and nano electronic components, *Proc. IEEE*. 94 (2006) 1549–1570.
- [15] J.-W. Song, L.-W. Fan, Temperature dependence of the contact angle of water: A review of research progress, theoretical understanding, and implications for boiling heat transfer, *Adv. Colloid Interface Sci.* 288 (2021) 102339.

- [16] J.M. Ludwicki, F.L. Robinson, P.H. Steen, Switchable wettability for condensation heat transfer, *ACS Appl. Mater. Interfaces*. 12 (2020) 22115–22119.
- [17] H. Zhao, D. Beysens, From droplet growth to film growth on a heterogeneous surface: condensation associated with a wettability gradient, *Langmuir*. 11 (1995) 627–634.
- [18] M. Nenad, X. Rong, D.J. Preston, R. Enright, I. McKay, E.N. Wang, Condensation on hydrophilic, hydrophobic, nanostructured superhydrophobic and oil-infused surfaces, (2013).
- [19] Y. Yao, J. Aizenberg, K.-C. Park, Dropwise condensation on hydrophobic bumps and dimples, *Appl. Phys. Lett.* 112 (2018) 151605.
- [20] Y.A. Cengel, A.J. Ghajar, *Heat and mass transfer, A Pract. Approach*. (2007).
- [21] E. Schmidt, W. Schurig, W. Sellschopp, Versuche über die Kondensation von Wasserdampf in Film-und Tropfenform, *Tech. Mech. Und Thermodyn.* 1 (1930) 53–63.
- [22] A. Cavallini, G. Censi, D. Del Col, L. Doretti, G.A. Longo, L. Rossetto, C. Zilio, Condensation inside and outside smooth and enhanced tubes—a review of recent research, *Int. J. Refrig.* 26 (2003) 373–392.
- [23] A.S. Dalkilic, S. Wongwises, Intensive literature review of condensation inside smooth and enhanced tubes, *Int. J. Heat Mass Transf.* 52 (2009) 3409–3426.
- [24] W.-T. Ji, G.-H. Chong, C.-Y. Zhao, H. Zhang, W.-Q. Tao, Condensation heat transfer of R134a, R1234ze (E) and R290 on horizontal plain and enhanced titanium tubes, *Int. J. Refrig.* 93 (2018) 259–268.
- [25] Y. Li, L. Li, J. Sun, Bioinspired Self-Healing Superhydrophobic Coatings, *Angew. Chemie Int. Ed.* 49 (2010) 6129–6133.
- [26] S. Lee, K. Cheng, V. Palmre, M.D.M.H. Bhuiya, K.J. Kim, B.J. Zhang, H. Yoon, Heat transfer measurement during dropwise condensation using micro/nano-scale porous surface, *Int. J. Heat Mass Transf.* 65 (2013) 619–626.
- [27] A. Ulman, Formation and structure of self-assembled monolayers, *Chem. Rev.* 96 (1996) 1533–1554.
- [28] A. Lafuma, D. Quéré, Slippery pre-suffused surfaces, *EPL (Europhysics Lett.)* 96 (2011) 56001.
- [29] T.-S. Wong, S.H. Kang, S.K.Y. Tang, E.J. Smythe, B.D. Hatton, A. Grinthal, J. Aizenberg, Bioinspired self-repairing slippery surfaces with pressure-stable omniphobicity, *Nature*. 477 (2011) 443–447.
- [30] J.D. Smith, R. Dhiman, S. Anand, E. Reza-Garduno, R.E. Cohen, G.H. McKinley, K.K. Varanasi, Droplet mobility on lubricant-impregnated surfaces, *Soft Matter*. 9 (2013) 1772–1780.
- [31] K.J. Renken, C.D. Mueller, Measurements of enhanced film condensation utilizing a porous

- metallic coating, *J. Thermophys. Heat Transf.* 7 (1993) 148–152.
- [32] D.J. Preston, K.L. Wilke, Z. Lu, S.S. Cruz, Y. Zhao, L.L. Becerra, E.N. Wang, Gravitationally driven wicking for enhanced condensation heat transfer, *Langmuir*. 34 (2018) 4658–4664.
- [33] R. Wang, D.S. Antao, Capillary-enhanced filmwise condensation in porous media, *Langmuir*. 34 (2018) 13855–13863.
- [34] D. Niu, G.H. Tang, The effect of surface wettability on water vapor condensation in nanoscale, *Sci. Rep.* 6 (2016) 1–6. <https://doi.org/10.1038/srep19192>.
- [35] S. Yang, Y. Zhang, L. Chen, Molecular dynamics study on the effect of surface wettability on the performance of water vapor condensation, *AIP Adv.* 9 (2019).
- [36] B. El Fil, G. Kini, S. Garimella, A review of dropwise condensation: Theory, modeling, experiments, and applications, *Int. J. Heat Mass Transf.* 160 (2020) 120172.
- [37] J.L. McCormick, J.W. Westwater, Nucleation sites for dropwise condensation, *Chem. Eng. Sci.* 20 (1965) 1021–1036. [https://doi.org/10.1016/0009-2509\(65\)80104-X](https://doi.org/10.1016/0009-2509(65)80104-X).
- [38] S. Khandekar, K. Muralidhar, Dropwise condensation on inclined textured surfaces, 2014.
- [39] J.W. Rose, Dropwise condensation theory, *Int. J. Heat Mass Transf.* 24 (1981) 191–194.
- [40] İ.O. UÇAR, H.Y. ERBİL, Droplet condensation on polymer surfaces: A review, *Turkish J. Chem.* 37 (2013) 643–674.
- [41] X. Ma, J. Chen, D. Xu, J. Lin, C. Ren, Z. Long, Influence of processing conditions of polymer film on dropwise condensation heat transfer, *Int. J. Heat Mass Transf.* 45 (2002) 3405–3411.
- [42] D.W. Tanner, C.J. Potter, D. Pope, D. West, Heat transfer in dropwise condensation—Part I The effects of heat flux, steam velocity and non-condensable gas concentration, *Int. J. Heat Mass Transf.* 8 (1965) 419–426.
- [43] Z. Qi, Z. Dongchang, L. Jifang, Surface materials with dropwise condensation made by ion implantation technology, *Int. J. Heat Mass Transf.* 34 (1991) 2833–2835.
- [44] X. Chen, J. Wu, R. Ma, M. Hua, N. Koratkar, S. Yao, Z. Wang, Nanograsped micropylamidal architectures for continuous dropwise condensation, *Adv. Funct. Mater.* 21 (2011) 4617–4623.
- [45] C. Lo, C. Wang, M. Lu, Spatial control of heterogeneous nucleation on the superhydrophobic nanowire array, *Adv. Funct. Mater.* 24 (2014) 1211–1217.
- [46] R. Enright, N. Miljkovic, J.L. Alvarado, K. Kim, J.W. Rose, Dropwise condensation on micro-and nanostructured surfaces, *Nanoscale Microscale Thermophys. Eng.* 18 (2014) 223–250.
- [47] N.A. Patankar, Supernucleating surfaces for nucleate boiling and dropwise condensation

- heat transfer, *Soft Matter*. 6 (2010) 1613–1620.
- [48] S. Daniel, M.K. Chaudhury, J.C. Chen, Fast drop movements resulting from the phase change on a gradient surface, *Science* (80-.). 291 (2001) 633–636.
- [49] Y.-T. Cheng, D.E. Rodak, A. Angelopoulos, T. Gacek, Microscopic observations of condensation of water on lotus leaves, *Appl. Phys. Lett.* 87 (2005) 194112.
- [50] C. Dorrer, J. R uhe, Some thoughts on superhydrophobic wetting, *Soft Matter*. 5 (2009) 51–61.
- [51] A. Ghosh, S. Beaini, B.J. Zhang, R. Ganguly, C.M. Megaridis, Enhancing dropwise condensation through bioinspired wettability patterning, *Langmuir*. 30 (2014) 13103–13115.
- [52] P.S. Mahapatra, A. Ghosh, R. Ganguly, C.M. Megaridis, Key design and operating parameters for enhancing dropwise condensation through wettability patterning, *Int. J. Heat Mass Transf.* 92 (2016) 877–883.
- [53] M. Alwazzan, K. Egab, B. Peng, J. Khan, C. Li, Condensation on hybrid-patterned copper tubes (I): Characterization of condensation heat transfer, *Int. J. Heat Mass Transf.* 112 (2017) 991–1004.
- [54] M.M. Derby, A. Chatterjee, Y. Peles, M.K. Jensen, Flow condensation heat transfer enhancement in a mini-channel with hydrophobic and hydrophilic patterns, *Int. J. Heat Mass Transf.* 68 (2014) 151–160.
- [55] K.K. Varanasi, M. Hsu, N. Bhate, W. Yang, T. Deng, Spatial control in the heterogeneous nucleation of water, *Appl. Phys. Lett.* 95 (2009) 94101.
- [56] Y. Hou, M. Yu, X. Chen, Z. Wang, S. Yao, Recurrent filmwise and dropwise condensation on a beetle mimetic surface, *ACS Nano*. 9 (2015) 71–81. <https://doi.org/10.1021/nn505716b>.
- [57] A. Tokunaga, T. Tsuruta, Enhancement of condensation heat transfer on a microstructured surface with wettability gradient, *Int. J. Heat Mass Transf.* 156 (2020) 119839.
- [58] P. Shanmugavel, G.B. Bhaskar, M. Chandrasekaran, P.S. Mani, S.P. Srinivasan, An overview of fracture analysis in functionally graded materials, *Eur. J. Sci. Res.* 68 (2012) 412–439.
- [59] S.S. Wang, Fracture mechanics for delamination problems in composite materials, *J. Compos. Mater.* 17 (1983) 210–223.
- [60] E. M uller,  . Drařar, J. Schilz, W.A. Kaysser, Functionally graded materials for sensor and energy applications, *Mater. Sci. Eng. A*. 362 (2003) 17–39.
- [61] M. Niino, K. Kisara, M. Mori, Feasibility study of FGM technology in space solar power systems (SSPS), in: *Mater. Sci. Forum*, Trans Tech Publ, 2005: pp. 163–170.
- [62] W. Pompe, H. Worch, M. Epple, W. Friess, M. Gelinsky, P. Greil, U. Hempel, D.

- Scharnweber, K. Schulte, Functionally graded materials for biomedical applications, *Mater. Sci. Eng. A.* 362 (2003) 40–60.
- [63] Z. Liu, M.A. Meyers, Z. Zhang, R.O. Ritchie, Functional gradients and heterogeneities in biological materials: Design principles, functions, and bioinspired applications, *Prog. Mater. Sci.* 88 (2017) 467–498.
- [64] B. Saleh, J. Jiang, R. Fathi, T. Al-hababi, Q. Xu, L. Wang, D. Song, A. Ma, 30 Years of functionally graded materials: An overview of manufacturing methods, Applications and Future Challenges, *Compos. Part B Eng.* 201 (2020) 108376.
- [65] C. Gerk, M. Willert-Porada, Development of graded composite electrodes for the SOFC, in: *Mater. Sci. Forum, Trans Tech Publ*, 1999: pp. 806–813.
- [66] R. Jedamzik, A. Neubrand, J. Rödel, Characterisation of electrochemically processed graded tungsten/copper composites, in: *Mater. Sci. Forum, Trans Tech Publ*, 1999: pp. 782–787.
- [67] W.G. Hoover, C.G. Hoover, Nonequilibrium molecular dynamics, *Condens. Matter Phys.* (2005).
- [68] Q. Sheng, J. Sun, Q. Wang, W. Wang, H.S. Wang, On the onset of surface condensation: Formation and transition mechanisms of condensation mode, *Sci. Rep.* 6 (2016) 1–9.
- [69] K. Yasuoka, M. Matsumoto, Molecular dynamics of homogeneous nucleation in the vapor phase. I. Lennard-Jones fluid, *J. Chem. Phys.* 109 (1998) 8451–8462.
- [70] K.K. Tanaka, A. Kawano, H. Tanaka, Molecular dynamics simulations of the nucleation of water: Determining the sticking probability and formation energy of a cluster, *J. Chem. Phys.* 140 (2014).
- [71] W. Xu, Z. Lan, B.L. Peng, R.F. Wen, X.H. Ma, Effect of surface free energies on the heterogeneous nucleation of water droplet: A molecular dynamics simulation approach, *J. Chem. Phys.* 142 (2015).
- [72] X. Ou, X. Wang, Z. Lin, J. Li, Heterogeneous Condensation of Water on the Mica (001) Surface: A Molecular Dynamics Simulation Work, *J. Phys. Chem. C.* 121 (2017) 6813–6819..
- [73] J.H. Pu, J. Sun, Q. Sheng, W. Wang, H.S. Wang, Dependences of Formation and Transition of the Surface Condensation Mode on Wettability and Temperature Difference, *Langmuir.* 36 (2020) 456–464.
- [74] Q. Sheng, J. Sun, W. Wang, H.S. Wang, C.G. Bailey, How solid surface free energy determines coalescence-induced nanodroplet jumping: A molecular dynamics investigation, *J. Appl. Phys.* 122 (2017).
- [75] B. Xu, Z. Chen, Molecular dynamics study of water vapor condensation on a composite wedge-shaped surface with multi wettability gradients, *Int. Commun. Heat Mass Transf.* 105 (2019) 65–72.

- [76] A. Giacomello, S. Meloni, M. Chinappi, C.M. Casciola, Cassie-baxter and wenzel states on a nanostructured surface: Phase diagram, metastabilities, and transition mechanism by atomistic free energy calculations, *Langmuir*. 28 (2012) 10764–10772.
- [77] S. Gao, Q. Liao, W. Liu, Z. Liu, Effects of Solid Fraction on Droplet Wetting and Vapor Condensation: A Molecular Dynamic Simulation Study, *Langmuir*. 33 (2017) 12379–12388.
- [78] S. Gao, W. Liu, Z. Liu, Tuning nanostructured surfaces with hybrid wettability areas to enhance condensation, *Nanoscale*. 11 (2019) 459–466.
- [79] Q. Wang, H. Xie, J. Liu, C. Liu, Heterogeneous nucleation of argon vapor on the nanostructure surface with molecular dynamics simulation, *J. Mol. Graph. Model*. 100 (2020) 107674.
- [80] M.M. Rashidi, S. Ghahremanian, D. Toghraie, P. Roy, Effect of solid surface structure on the condensation flow of Argon in rough nanochannels with different roughness geometries using molecular dynamics simulation, *Int. Commun. Heat Mass Transf.* 117 (2020) 104741.
- [81] L. Li, P. Ji, Y. Zhang, Molecular dynamics simulation of condensation on nanostructured surface in a confined space, *Appl. Phys. A Mater. Sci. Process*. 122 (2016).
- [82] Y. Wang, P. Keblinski, Role of wetting and nanoscale roughness on thermal conductance at liquid-solid interface, *Appl. Phys. Lett.* 99 (2011) 73112.
- [83] R.J. Stoner, H.J. Maris, Kapitza conductance and heat flow between solids at temperatures from 50 to 300 K, *Phys. Rev. B*. 48 (1993) 16373.
- [84] Z. Deng, C. Zhang, C. Shen, J. Cao, Y. Chen, Self-propelled dropwise condensation on a gradient surface, *Int. J. Heat Mass Transf.* 114 (2017) 419–429.
- [85] T. Wang, W. Li, L. Liu, H. Chen, Y. Wang, J. Zhang, Y. Yan, The mechanism for the motion of nanoscale water droplet induced by wetting gradient: A molecular dynamic study, *Comput. Mater. Sci.* 105 (2015) 39–46.
- [86] B. Peng, X. Ma, Z. Lan, W. Xu, R. Wen, Experimental investigation on steam condensation heat transfer enhancement with vertically patterned hydrophobic–hydrophilic hybrid surfaces, *Int. J. Heat Mass Transf.* 83 (2015) 27–38.
- [87] A. Chatterjee, M.M. Derby, Y. Peles, M.K. Jensen, Enhancement of condensation heat transfer with patterned surfaces, *Int. J. Heat Mass Transf.* 71 (2014) 675–681.
- [88] K. Egab, M. Alwazzan, B. Peng, S.K. Oudah, Z. Guo, X. Dai, J. Khan, C. Li, Enhancing filmwise and dropwise condensation using a hybrid wettability contrast mechanism: Circular patterns, *Int. J. Heat Mass Transf.* 154 (2020) 119640.
- [89] K.K. Varanasi, M. Hsu, N. Bhate, W. Yang, T. Deng, Spatial control in the heterogeneous nucleation of water, *Appl. Phys. Lett.* 95 (2009) 1–4.
- [90] Y. Shang, Y. Hou, M. Yu, S. Yao, Modeling and optimization of condensation heat transfer

- at biphilic interface, *Int. J. Heat Mass Transf.* 122 (2018) 117–127.
- [91] Z. Liang, A. Chandra, E. Bird, P. Keblinski, A molecular dynamics study of transient evaporation and condensation, *Int. J. Heat Mass Transf.* 149 (2020) 119152.
- [92] J. Sun, H.S. Wang, On the early and developed stages of surface condensation: Competition mechanism between interfacial and condensate bulk thermal resistances, *Sci. Rep.* 6 (2016) 1–12.
- [93] G. Nagayama, M. Takematsu, H. Mizuguchi, T. Tsuruta, Molecular dynamics study on condensation/evaporation coefficients of chain molecules at liquid-vapor interface, *J. Chem. Phys.* 143 (2015).
- [94] D. Huang, X. Quan, P. Cheng, An investigation on vapor condensation on nanopillar array surfaces by molecular dynamics simulation, *Int. Commun. Heat Mass Transf.* 98 (2018) 232–238.
- [95] S. Ghahremanian, A. Abbassi, Z. Mansoori, D. Toghraei, Molecular dynamics simulation of annular condensation of vapor argon through a nanochannel for different saturation conditions with focusing on the flow and heat transfer, *Int. Commun. Heat Mass Transf.* 116 (2020) 104704.
- [96] B.J. Alder, T.E. Wainwright, Phase transition for a hard sphere system, *J. Chem. Phys.* 27 (1957) 1208–1209.
- [97] B.J. Alder, T.E. Wainwright, Studies in molecular dynamics. I. General method, *J. Chem. Phys.* 31 (1959) 459–466.
- [98] M.P. Allen, M.R. Wilson, Computer simulation of liquid crystals, *J. Comput. Aided. Mol. Des.* 3 (1989) 335–353.
- [99] A. Hospital, J.R. Goñi, M. Orozco, J.L. Gelpí, Molecular dynamics simulations: advances and applications, *Adv. Appl. Bioinforma. Chem. AABC.* 8 (2015) 37.
- [100] J.M. Haile, I. Johnston, A.J. Mallinckrodt, S. McKay, Molecular dynamics simulation: elementary methods, *Comput. Phys.* 7 (1993) 625.
- [101] S. Goel, M. Knaggs, G. Goel, X.W. Zhou, H.M. Upadhyaya, V.K. Thakur, V. Kumar, G. Bizarri, A. Tiwari, A. Murphy, Horizons of modern molecular dynamics simulation in digitalized solid freeform fabrication with advanced materials, *Mater. Today Chem.* 18 (2020) 100356.
- [102] D. Frenkel, B. Smit, M.A. Ratner, *Understanding molecular simulation: from algorithms to applications*, Academic press San Diego, 1996.
- [103] J.E. Lennard-Jones, A.F. Devonshire, Critical phenomena in gases-I, *Proc. R. Soc. London. Ser. A-Mathematical Phys. Sci.* 163 (1937) 53–70.
- [104] P.M. Morse, Diatomic molecules according to the wave mechanics. II. Vibrational levels, *Phys. Rev.* 34 (1929) 57.

- [105] M.S. Daw, S.M. Foiles, M.I. Baskes, The embedded-atom method: a review of theory and applications, *Mater. Sci. Reports.* 9 (1993) 251–310.
- [106] J. Tersoff, Modeling solid-state chemistry: Interatomic potentials for multicomponent systems, *Phys. Rev. B.* 39 (1989) 5566.
- [107] D.W. Brenner, Empirical potential for hydrocarbons for use in simulating the chemical vapor deposition of diamond films, *Phys. Rev. B.* 42 (1990) 9458.
- [108] R. Car, M. Parrinello, Unified approach for molecular dynamics and density-functional theory, *Phys. Rev. Lett.* 55 (1985) 2471.
- [109] J.-M. Combes, P. Duclos, R. Seiler, The born-oppenheimer approximation, in: *Rigorous At. Mol. Phys.*, Springer, 1981: pp. 185–213.
- [110] J. Fu, Overview of Nanostructure Modeling and Atomistic Simulation Methods, *At. Simul. Anisotropic Cryst. Struct. Nanoscale.* (2019) 1.
- [111] G. Ziegenhain, A. Hartmaier, H.M. Urbassek, Pair vs many-body potentials: Influence on elastic and plastic behavior in nanoindentation of fcc metals, *J. Mech. Phys. Solids.* 57 (2009) 1514–1526.
- [112] M.J. Buehler, *Atomistic modeling of materials failure*, Springer, 2008.
- [113] M.S. Daw, M.I. Baskes, Embedded-atom method: Derivation and application to impurities, surfaces, and other defects in metals, *Phys. Rev. B.* 29 (1984) 6443.
- [114] A.C.T. Van Duin, S. Dasgupta, F. Lorant, W.A. Goddard, ReaxFF: a reactive force field for hydrocarbons, *J. Phys. Chem. A.* 105 (2001) 9396–9409.
- [115] L. Verlet, Computer" experiments" on classical fluids. I. Thermodynamical properties of Lennard-Jones molecules, *Phys. Rev.* 159 (1967) 98.
- [116] W.C. Swope, H.C. Andersen, P.H. Berens, K.R. Wilson, A computer simulation method for the calculation of equilibrium constants for the formation of physical clusters of molecules: Application to small water clusters, *J. Chem. Phys.* 76 (1982) 637–649.
- [117] O.N. De Souza, R.L. Ornstein, Effect of periodic box size on aqueous molecular dynamics simulation of a DNA dodecamer with particle-mesh Ewald method, *Biophys. J.* 72 (1997) 2395–2397.
- [118] J.W. Gibbs, *Elementary principles in statistical mechanics: developed with especial reference to the rational foundations of thermodynamics*, C. Scribner's sons, 1902.
- [119] S. Plimpton, Fast parallel algorithms for short-range molecular dynamics, *J. Comput. Phys.* 117 (1995) 1–19.
- [120] A. Stukowski, Visualization and analysis of atomistic simulation data with OVITO—the Open Visualization Tool, *Model. Simul. Mater. Sci. Eng.* 18 (2009) 15012.
- [121] A. Hens, R. Agarwal, G. Biswas, Nanoscale study of boiling and evaporation in a liquid Ar

- film on a Pt heater using molecular dynamics simulation, *Int. J. Heat Mass Transf.* 71 (2014) 303–312.
- [122] H.A. Lorentz, Ueber die Anwendung des Satzes vom Virial in der kinetischen Theorie der Gase, *Ann. Phys.* 248 (1881) 127–136.
- [123] J.G. Kirkwood, F.P. Buff, The statistical mechanical theory of surface tension, *J. Chem. Phys.* 17 (1949) 338–343.
- [124] A.K.M.M. Morshed, T.C. Paul, J.A. Khan, Effect of nanostructures on evaporation and explosive boiling of thin liquid films: A molecular dynamics study, *Appl. Phys. A Mater. Sci. Process.* 105 (2011) 445–451.
- [125] S.C. Maroo, J.N. Chung, Molecular dynamic simulation of platinum heater and associated nano-scale liquid argon film evaporation and colloidal adsorption characteristics, *J. Colloid Interface Sci.* 328 (2008) 134–146.
- [126] Q. Cao, W. Shao, X. Ren, X. Ma, K. Shao, Z. Cui, Y. Liu, Molecular dynamics simulations of the liquid film evaporation heat transfer on different wettability hybrid surfaces at the nanoscale, *J. Mol. Liq.* 314 (2020) 113610.
- [127] Q. Cao, Z. Cui, Molecular dynamics simulations of the effect of surface wettability on nanoscale liquid film phase-change, *Numer. Heat Transf. Part A Appl.* 75 (2019) 533–547.
- [128] Y. Ueki, Y. Miyazaki, M. Shibahara, T. Ohara, Molecular dynamics study of thermal resistance of solid-liquid interface in contact with single layer of nanoparticles, *Int. J. Heat Mass Transf.* 120 (2018) 608–623.
- [129] H. Han, C. Schlawitschek, N. Katyal, P. Stephan, T. Gambaryan-Roisman, F. Leroy, F. Müller-Plathe, Solid–liquid interface thermal resistance affects the evaporation rate of droplets from a surface: A study of perfluorohexane on chromium using molecular dynamics and continuum theory, *Langmuir.* 33 (2017) 5336–5343.
- [130] K. Oura, M. Katayama, A. V Zotov, V.G. Lifshits, A.A. Saranin, Growth of thin films, in: *Surf. Sci.*, Springer, 2003: pp. 357–387.
- [131] H. Takagishi, T. Masuda, T. Shimoda, R. Maezono, K. Hongo, Method for the Calculation of the Hamaker Constants of Organic Materials by the Lifshitz Macroscopic Approach with Density Functional Theory, *J. Phys. Chem. A.* 123 (2019) 8726–8733.
- [132] H.C. Hamaker, The London-van der Waals attraction between spherical particles, *Physica.* 4 (1937) 1058–1072.
- [133] D. Ivanova-Stancheva, Influence of the hamaker constant on the value of the critical thickness of foam films, *Coatings.* 9 (2019) 576.
- [134] M. Rauscher, S. Dietrich, Nano-droplets on structured substrates, *Soft Matter.* 5 (2009) 2997–3001.
- [135] Z. Liang, T. Biben, P. Keblinski, Molecular simulation of steady-state evaporation and

- condensation: Validity of the Schrage relationships, *Int. J. Heat Mass Transf.* 114 (2017) 105–114.
- [136] R.W. Schrage, *A theoretical study of interphase mass transfer*, Columbia University Press, 1953.
- [137] J. Straub, The role of surface tension for two-phase heat and mass transfer in the absence of gravity, *Exp. Therm. Fluid Sci.* 9 (1994) 253–273.
- [138] Y.W. Wu, C. Pan, Molecular dynamics simulation of thin film evaporation of Lennard-Jones liquid, *Nanoscale Microscale Thermophys. Eng.* 10 (2006) 157–170.
- [139] T. Ishiyama, T. Yano, S. Fujikawa, Molecular dynamics study of kinetic boundary condition at an interface between argon vapor and its condensed phase, *Phys. Fluids.* 16 (2004) 2899–2906.
- [140] T. Tsuruta, G. Nagayama, Molecular dynamics studies on the condensation coefficient of water, *J. Phys. Chem. B.* 108 (2004) 1736–1743.
- [141] Q. Cao, Z. Cui, W. Shao, Optimization method for grooved surface structures regarding the evaporation heat transfer of ultrathin liquid films at the nanoscale, *Langmuir.* 36 (2020) 2802–2815.
- [142] Q. Cao, W. Shao, Z. Cui, Molecular dynamics simulations and mathematical optimization method for surface structures regarding evaporation heat transfer enhancement at the nanoscale, *Int. J. Heat Mass Transf.* 153 (2020) 119616.
- [143] P.R. ten Wolde, D. Frenkel, Computer simulation study of gas–liquid nucleation in a Lennard-Jones system, *J. Chem. Phys.* 109 (1998) 9901–9918.
- [144] J. Wedekind, D. Reguera, What is the best definition of a liquid cluster at the molecular scale?, *J. Chem. Phys.* 127 (2007) 154516.